Metal Ion Implanted Electrodes for Dielectric Elastomer Actuators

PAR

Samuel ROSSET

EPFL

ÉCOLE POLYTECHNIQUE
FÉDÉRALE DE LAUSANNE

Suisse
2008

Space, [the guide] says, is big. Really big. You just won't believe how vastly, hugely, mindbogglingly big it is. I mean, you may think it's a long way down the road to the chemist's, but that's just peanuts to space.

Douglas Adams, The Hitchhiker's Guide to the Galaxy
English humorist & science fiction novelist (1952 - 2001)

Abstract

This thesis reports on the successful use of low-energy metal ion implantation to fabricate compliant electrodes for miniaturized dielectric elastomer actuators (DEAs, also known as artificial muscles). DEAs are elastomeric actuators capable of large deformations (above 100% depending on conditions) and which require deformable electrodes. On most of the macroscale DEAs, they are made of carbon powder or grease, which can be easily applied on large uniform surfaces (cm^2 to m^2). This technology is not applicable to small-size DEAs which require reliable electrodes that can be patterned on a mm-to-μm scale. On the other hand, metallic thin-film deposition can be used to make patterned electrodes, but their maximum strain is limited to that of metals, i.e. $2 - 3\%$.

The Microsystems for Space Technologies Laboratory (LMTS) has introduced implantation of metallic elements into soft polydimethylsiloxane (PDMS) layers by filtered cathodic vacuum arc, as a means of creating compliant electrodes on elastomers. The incoming metallic particles have an energy between $0.05 - 5$ keV, which leads to a spatial distribution of the implanted elements between the surface of the elastomer, and a depth of $50 - 60$ nm. The implanted atoms form nanometer-size clusters which are in contact but can slide relative to each other, hence keeping a conduction path at large strain. Titanium, palladium and gold implantations were conducted in an experimental implanter. Au-implanted electrodes exhibited the best overall performance, combining low sheet resistance ($100 - 200$ Ω/square), high maximum strain before loss of conductivity (175%), and a small impact on the Young's modulus of the PDMS on which they are created ($50 - 100\%$ relative increase).

Small-size circular diaphragm dielectric elastomer actuators ($\varnothing 1.5 - 3$ mm) with Au-implanted electrodes were fabricated and characterized. Out of plane displacements up to 25% of the membrane's diameter were observed. This is a factor 4 increase compared to similar devices using patterned Au thin-film as electrode material, thus demonstrating the outstanding properties of metal-ion implanted layers as compliant electrodes for DEAs.

Keywords: Dielectric elastomer actuators, Electroactive polymers, Artificial muscles, Metal ion implantation, Deformable electrodes, Smart materials.

Résumé

Cette thèse présente l'utilisation de l'implantation d'ions métalliques à basse énergie afin de fabriquer des électrodes déformables pour des actionneurs en polymères électroactifs (DEAs, ou muscles artificiels) miniaturisés. Les DEAs sont une classe d'actionneurs en élastomère, capables de très grandes déformations (plus de 100% selon les conditions), et qui nécessitent des électrodes qui peuvent subir ces déformations tout en restant conductrices. La plupart des DEAs de grande taille ont des électrodes faites à base de poudre ou graisse de carbone, qui peuvent facilement être appliquées sur de grandes surfaces uniformes (cm^2 à m^2). Cette technologie n'est pas applicable aux DEAs de petite taille, lesquels nécessitent des électrodes fiables qui peuvent être structurées à petite échelle (mm à μm). Si le dépôt de couches minces métalliques permet quant à lui de fabriquer des électrodes structurées, la déformation maximale de ses dernières est limitée à celle du métal qui les compose (typiquement 2%-3%) et n'est donc pas adapté à cette application.

Le Laboratoire des Microsystèmes pour les Technologies Spatiales (LMTS) a introduit l'implantation de métaux dans des couches de polydiméthylsiloxane (PDMS) par arc cathodique filtré (FCVA) afin de fabriquer des électrodes déformables sur des élastomères. Les particules métalliques ont une énergie distribuée entre $0.4 - 5$ keV, ce qui conduit à une distribution des particules implantées entre la surface du PDMS et $50 - 60$ nm. Les atomes implantés se regroupent et forment des nanoparticules qui se touchent tout en pouvant bouger les uns par rapport aux autres, ce qui permet de garder une bonne conductivité électrique pour des déformations importantes de l'électrode. Un implanteur FCVA a été construit et des implantations de titane, palladium et or ont été réalisées. Parmi ces 3 métaux, ce sont les électrodes implantées avec de l'or qui présentent les meilleures caractéristiques, en combinant une faible résistance de surface ($100 - 200$ Ω/carré), un allongement élevé avant la perte des propriétés de conduction électrique (175%), et un faible impact sur le module de Young du PDMS sur lequel elles sont réalisées ($50 - 100\%$ d'augmentation relative).

Des actionneurs miniaturisés constitués par des membranes circulaires ($\varnothing 1.5 - 3$ mm) avec des électrodes d'or implanté ont été fabriqués et caractérisés. Des déplacements hors du plan de 25% par rapport au diamètre de l'actionneur ont été obtenus. Ceci représente une augmentation d'un facteur 4 comparé à des actionneurs de taille similaire dont les électrodes étaient réalisées par du métal en couche mince structuré en anneaux concentriques, démontrant donc les propriétés exceptionnelles de l'implantation de ions métalliques appliquée à la fabrication d'électrodes pour des DEAs.

Mots clés: Actionneurs en polymères électroactifs, Muscles artificiels, Implantation d'ions métalliques, Electrodes déformables.

Contents

Chapter 1

Introduction

This thesis reports on the miniaturization of dielectric elastomer actuators and the fabrication of compliant electrodes for these devices by implantation of metal ions into soft elastomers.

Smart materials (i.e. materials that have one property that can be significantly changed by external stimuli, such as electric or magnetic fields, mechanical stress, temperature, moisture or pH) have gained wide interest in the last decades. Besides the well-known examples such as piezoelectric materials or shape memory alloys, smart polymers are gaining importance. Polymers have been used for a long time as a structural material in all kind of consumer products, but they have also started to be used as functional materials: photoresist for microfabrication processes, organic light emitting diodes (OLED) [1], and more recently, dielectric electroactive polymers (EAP) [2, 3]. Mainly initiated by Ron Pelrine and Roy Kornbluh from SRI international, research on dielectric EAP has quickly gathered a wide interest and has had (together with research on ionic EAP) its own annual conference (electroactive polymer actuators and devices) since 1998. Research groups from all over the world have started projects on this kind of actuation principle, and several companies have been founded to bring EAP-based products to the market.

EAPs form a large group of polymer-based actuators that respond to electric stimuli by a change of shape. These actuators are generally classified in two categories depending on their activation mechanism: electronic and ionic (Table 1.1) [4]. Electronic EAP are driven by Coulomb forces (electrostrictive, electrostatic, piezoelectric and ferroelectric). Ionic EAPs are driven by electrochemistry, i.e. ion mobility or diffusion; they require low actuation voltages, but need power to hold a static position. Ion transport is assured by an electrolyte and operation in air is problematic due to the possible drying of the electrolyte. On the other hand, electronic EAPs require higher voltage level to work, but do not need power to hold a static position. Operation in air is not problematic for those devices. Consequently we have decided to concentrate our efforts for the miniaturization of EAPs on the electronic branch exclusively, and more precisely on dielectric EAPs.

Dielectric EAPs can produce very large surface strains (cf. chap. 2) and require electrodes that can sustain the same amount of strain without damages. This is more challenging as it may sound, as conductive materials are generally not compliant, and compliant materials not conductive. As R. Pelrine et al.

Table 1.1: *Classification of EAPs (from [4]). The main representant of each category is indicated in italics.*

Electronic EAP	Ionic EAP
Dielectric EAP	Carbon Nanotubes (CNT)
Electrostrictive Graft Elastomers	Conductive Polymers
Electrostrictive Paper	ElectroRheological Fluids (ERF)
Electro-Viscoelastic Elastomers	Ionic Polymer Gels (IPG)
Ferroelectric Polymers	*Ionic Polymer-*
Liquid Crystal Elastomers (LCE)	*Metallic Composite (IPMC)*

stated in the first major publication on dielectric EAPs: *The ideal electrode would be highly conductive, perfectly compliant and patternable, and could be made thin relative to the polymer thickness* [5]. The general compromise is to use electrodes based on carbon powders (cf. section 2.1), which – except for the compliance – are far from the *perfect electrodes* described by Pelrine. Furthermore, carbon-based electrodes are hardly applicable to small-size devices, for which the patterning of the electrodes on a small scale (mm to μm) is necessary, without mentioning the impossibility to work with carbon powders in a clean room.

Consequently, we present metal ion implantation as a way to make compliant electrodes that have a high conductivity (< 1 kΩ/square), a small thickness (~ 50 nm), and that can be easily patterned by photolithography or with a steel shadow mask. Ion implanted electrodes are therefore much closer to the *perfect electrode* described by Pelrine than the widely used carbon-based electrodes.

This document presents the mechanical and electrical characteristics of electrodes made by ion implantation, as well as application of this technology to the fabrication and characterization of diaphragm dielectric EAPs.

Chapter 2

Dielectric Elastomer Actuators

Dielectric electroactive polymers actuators, also known as dielectric elastomer actuators (DEAs), are electrostatic devices formed by a layer of soft elastomer (mainly silicone- or acrylic-based polymers [6], with a Young's modulus of $0.05 - 5$ MPa) sandwiched between two compliant electrodes: they are basically rubbery capacitors. When a voltage is applied between the electrodes, the electric field generates an electrostatic attractive force between the electrodes (also known as *Maxwell stress*). This force squeezes the elastomer, and its thickness decreases. As elastomers are generally considered to be incompressible (Poisson coefficient of 0.5, or very high bulk modulus) [7], this thickness decrease leads to an area expansion of the same magnitude (Fig. 2.1). Consequently, this method of actuation requires compliant electrodes and would not work with rigid electrodes. Depending on the conditions and the type of elastomer, area strains exceeding 200% can be obtained [2].

In terms of strain capabilities and energy density, the characteristics of DEAs are similar to those of natural muscles, and they both respond to electrical stimulus by a change in shape. Consequently, DEAs are sometimes nicknamed *artificial muscles* [3]. Their large strains and force capabilities, coupled to their intrinsic linear motion and low weight, make DEAs very interesting candidates to a broad range of applications. The field of humanlike robotics would for example greatly beneficiate from the replacement of electrical motors
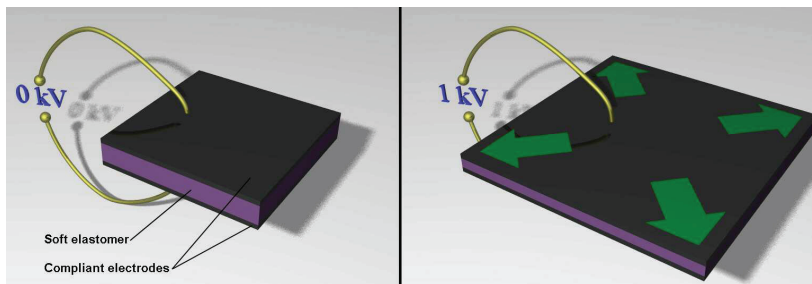

Figure 2.1: *Dielectric EAP (DEAP) principle. When a voltage is applied to the electrodes (typically up to 1 kV), the electrostatic pressure squeezes the elastomer dielectric (right side). The volume of the dielectric being quasi constant, the whole structure stretches (in the case of free boundary conditions).*

and gears by artificial muscles, and effort is currently being made to develop artificial muscles that can compete with a human in an arm wrestling competition [8, 9]. More generally, DEAs are possible substitutes to electromagnetic motors in applications which require linear motion, such as robot manipulators [10, 11], or in harsh environments, such as samples manipulators for magnetic resonance imaging (MRI) [12], whose strong electromagnetic fields makes the use of conventional motors impossible.

2.1   Electrodes for dielectric elastomer actuators

The major requirement that an electrode for DEA must meet is *compliance*: the ability of stretching without breaking, and while remaining conductive. As exposed above, application of a voltage between the electrodes of a DEA can lead to large area expansion of the device. Its electrodes must be able to sustain the same strain without damage. Metallic layers, which are often used to make electrodes because of their excellent electrical conductivity, are unsuitable for this application, as they are too stiff with their Young's modulus 5–6 orders of magnitude higher than that of the elastomers used for DEAs. Additionally, they can only sustain a few percents (2%-3%) of elastic strain before plastic deformation takes place.

Most of the macroscale DEAs have electrodes made of conductive carbon particles (carbon black), either directly applied on the PDMS, or – for better adhesion – suspended in grease or in a soft polymer matrix [3]. Depending on the composition of the material in which the carbon black is suspended, and the method of application of the mixture on the PDMS, carbon-based electrodes can exhibit different properties [13]. O'Brien et al. tested three different methods to make carbon-based electrodes for self-sensing applications [14]. They measured the resistance-strain behavior of loose carbon powder, silicone-bound carbon powder and carbon grease. Loose powder was found to be the best solution in term of electric properties, with low noise and absence of hysteresis. However, it suffers from very poor adhesion of the powder on the elastomer. Additionally, Pelrine et al. noted that loose carbon powders are problematic at very large strains, because full coverage of the surface cannot be assured [15]. Consequently, suspension of powders in grease or silicone are generally preferred, as it remains conductive at large strains and offers better adhesion to the elastomer.

2.2   Miniaturization of dielectric elastomer actuators

Bringing the DEA technology to the world of micro-electro-mechanical systems (MEMS) is a promising opportunity, for it enables to obtain characteristics (force, displacement, response speed) unmatched by any other mainstream MEMS actuator types, such as air-gap electrostatic, thermal, magnetic or piezoelectric actuators (Fig 2.2).

Several small-size devices based on dielectric elastomer actuators have already been investigated. M. Aschwanden has fabricated highly tunable diffraction gratings achieving a period change of 19.2%, which is an improvement of a factor 90 compared to analog tunable gratings based on hard materials [16]. J. Loverich et. al. introduced a new class of all-polymer micropumps, which
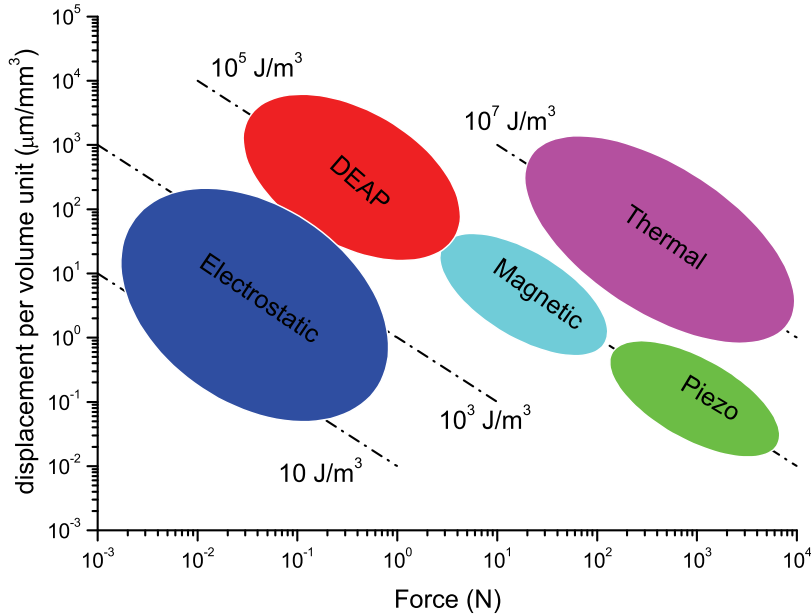
Figure 2.2: *Comparison between different actuation principles compatible with microsystems. The displacement per volume unit vs. output force is plotted. Dielectric EAPs (DEAPs) present an exceptional combination of force and displacement capability that no other principle of actuation has.*

are low cost, insensitive to gas bubbles, and which occupy less than 10 mm^2 of chip space while producing flow rates up to 77 μl/min [17]. Pimpin et. al. developped micro syntethic jet actuators based on DEAs that are capable to produce a jet flow up to 1.3 kHz with a maximum velocity of 0.4 m/s [18,19].

In spite of being succesful applications in the field of micro-DEAs, the examples exposed above suffer from one common problem: compliant electrodes. The electrodes of Loverich's pump are made with carbon grease and suffer from migration of the conductive material, which results in the loss of electrical connection with the power supply after about 10 hours of operation. The loose powder electrodes of Aschwanden's device are patterned using a carbon black coated polydimethylsiloxane (PDMS) stamp. He has obtained a good resolution, with patterened lines of 100 μm. However, working with carbon powder results in quite a messy process, which is a problem that generally concerns carbon-based electrodes, but which is rarely admitted in literature.

Pimpin's synthetic jet actuator is really interesting, because the author is the first to propose an alternate way to make compliant electrodes, that are applicable to small-size devices by being patternable, clean and robust. It consists in using a $170-200$ nm e-beam evaporated gold metallic layer that is patterned in linked concentric circles in order to increase the achievable strain and to reduce the stiffening impact on the elastomer. Beside sharing the same objective of finding a way to make patternable and reliable compliant electrodes, our actuators are very similar to Pimpin's in term of size, geometry and operation principle (cf. chapter 6), thus forming a good comparison point.
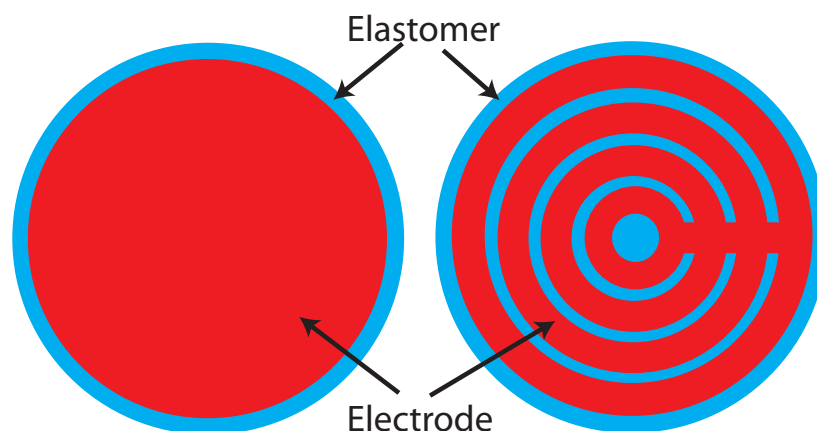
Figure 2.3: *Schematic representation of a plain electrode (left) and a patterned electrode (right). The patterned electrodes allows to use non-compliant material such as evaporated metals as electrodes, but require a patterning resolution much higher than the actuator's size.*

Pimpin's circular actuators are able to produce vertical displacement up to 5.6% of their diameter, which is 13.6 times the displacement obtained with plain electrodes (0.5%) of the same thickness [19]. Our proof of concept ion-implanted DEA presented at Transducers 2005 in Seoul exhibited vertical displacements greater than 10% of its diameter [20], and we have obtained vertical displacement up to 25% on optimized actuators (cf. chapter 6), thus demonstrating the impressive performance increase brought by ion implantation. Indeed, this is 4.5 times more than Pimpin's patterned electrodes, and 48 times higher than plain (i.e. unpatterned, covering the whole membrane's surface) evaporated electrodes.

Patterned electrodes suffer from an important drawback compared to plain electrodes: to obtain his 5.6% vertical displacement on a $\varnothing 2$ mm actuator, Pimpin's patterned electrode were 23 μm wide with inter-spacing of 7 μm, which is quite a challenging resolution for phtotolithography on PDMS. Reducing the size of the actuator would therefore be difficult. Plain electrodes do not suffer from this problem, as making a $\varnothing 100$ μm actuator, would require to pattern an electrode of the same dimension, which is not problematic (Fig. 2.3). Actuators with plain electrodes can therefore be miniaturized more easily, without fear of technical limitations.

As ion-implanted electrodes have a low impact on the Young's modulus of the polymer on which they are made, there is no need to finely pattern them: plain electrodes of the same size than the actuator can be used. Other advantages of ion implanted-electrodes, as will be exposed in the following chapters are: negligible thickness ($\sim 20-50$ nm *inside* the elastomer), low mass (~ 4 μg/cm^2), low surface resistivity (< 10 kΩ/square), large strain capabilities ($< 150\%$), moderate impact on Young's modulus ($+50-100\%$), patternability and transparency.

2.3 Governing equations for dielectric elastomer actuators

DEAs are essentially capacitors whose dielectric is an elastomer. The well known equations derived for air-gap capacitors are consequently applicable to this situation with some modifications to take into account the change in area that occurs during deformation and that is not present in conventional air-gap electrostatic devices, used in most MEMS application in which the gap height is voltage-tunable. The most fundamental equation that characterizes DEAs is the electrostatic pressure p that is generated upon application of a voltage between the electrodes, and that is defined as the change in electrostatic energy U per unit area A per unit displacement of the film in the thickness direction z [5]:

$$p = \frac{1}{A}\frac{dU}{dz} \ \ (\text{Pa}). \tag{2.1}$$

The electrostatic energy, as for any capacitor, is given by:

$$U = \frac{1}{2}CV^2 \ \ (\text{J}), \tag{2.2}$$

where V is the applied voltage (V), and C the capacitance (F) of the capacitor formed by the actuator (parallel-plate capacitor of area A and thickness z):

$$C = \frac{\epsilon_0\epsilon_r A}{z}, \tag{2.3}$$

with ϵ_0 the vacuum permittivity and ϵ_r the relative permittivity of the elastomer. The change in electrostatic energy due to a thickness change dz and an area change dA can therefore be calculated:

$$dU = \frac{\partial U}{\partial z}dz + \frac{\partial U}{\partial A}dA. \tag{2.4}$$

The thickness and area changes are linked by the volume incompressibility of elastomers (Poisson coefficient, ν, equal to 0.5), which means that in any deformed state, the elastomer volume is equal to its undeformed volume V_0. Hence:

$$A = \frac{V_0}{z} \Rightarrow dA = -\frac{A}{z}dz. \tag{2.5}$$

Combining together eqs. 2.2 to 2.5 leads to:

$$dU = \frac{\epsilon_0\epsilon_r V^2}{2}\left(-\frac{A}{z^2} - \frac{A}{z^2}\right)dz = -\frac{A\epsilon_0\epsilon_r V^2}{z^2}dz \tag{2.6}$$

Finally, introducing eq. 2.6 into eq. 2.1 allows to find the electrostatic pressure:

$$p = -\frac{\epsilon_0\epsilon_r V^2}{z^2} = -\epsilon_0\epsilon_r E^2, \tag{2.7}$$

where $E = V/z$ is the electrostatic field. The negative sign indicates that the generated stress is compressive.

It should be noted that the electrostatic pressure of a DEA is twice the one of a parallel-plate capacitor, due to the dA contribution to the change
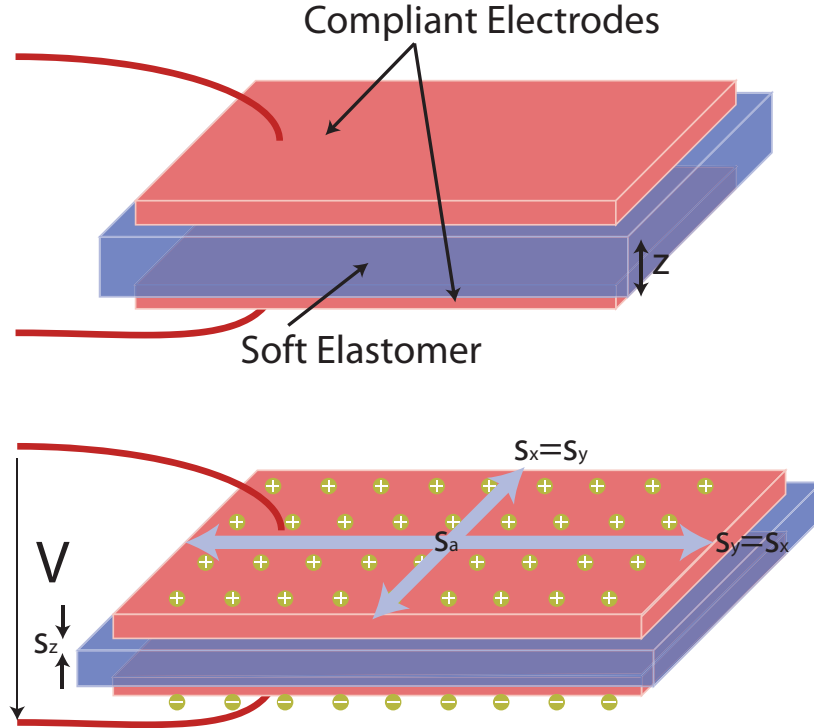
Figure 2.4: *Free boundary conditions case: the negative thickness strain s_z causes a positive area strain s_a which can be decomposed into two equal longitudinal (or in-plane) strain components $s_x = s_y$*

in electrostatic energy dU (eq. 2.4). Physically, this is explained by the fact that on an electrode, the charges repel each other and tend to increase the electrode's area, which contributes to the deformation. Although this lateral force is also present in parallel plate capacitors, it can not contribute to the deformation because of the rigid electrodes. For constant charge operation, spreading the charges of same sign (increasing the area) and bringing opposite charges closer (decreasing the thickness) both contribute to the decrease of electrostatic energy.

In addition to this factor two increase due to the area expansion, the electrostatic pressure of DEAs is further increased compared to air-gap capacitors. The proportionality of the electrostatic pressure (eq. 2.7) to the relative permittivity of the elastomer plays in favor of DEAs, as elastomers commonly used have an ϵ_r of $2 - 5$. It is even possible to chemically modify some silicones (such as PDMS) by adding fillers to further increase their dielectric constant [21]. The electric field that elastomers can sustain is higher than air and varies between $\sim 30 - 250$ V/μm [15]. Consequently, the electrostatic energy density that can be stored in a DEA can be one or two orders of magnitude higher than that of an air-gap capacitor (Fig. 2.2).

A DEA will respond to the electrostatic pressure by changing its shape in order to reach an equilibrium position. The mechanical response strongly depends on the actuator's geometry and boundary conditions. The analytical

modeling of our diaphragm actuators will be exposed in detail later (cf. chapter 6), but general considerations can be made for the case of hypothetical free boundary conditions, in which the application of a voltage difference between the electrodes leads to a thickness decrease and an area expension (Fig. 2.4). As a first approximation, let's assume that the elastomer is characterized by an isotropic Young's modulus Y independant of strain, and a Poisson coefficient $\nu = 0.5$ (incompressibility). We can equalize the electrostatic pressure (eq. 2.7) with the elastic compressive stress from Hooke's law, which links the the vertical stress to the vertical strain s_z[1], which is negative in case of compression:

$$-\epsilon_0 \epsilon_r E^2 = Y s_z \Rightarrow s_z = -\frac{\epsilon_0 \epsilon_r V^2}{Y z^2}. \tag{2.8}$$

The in-plane strains are linked to the vertical strain by the condition of volumic incompressibility:

$$V = V_0 = x_0(1 + s_x)y_0(1 + s_y)z_0(1 + s_z)$$
$$V_0 = V_0(1 + s_x)(1 + s_y)(1 + s_z)$$
$$\Rightarrow (1 + s_x)^2(1 + s_z) = 1, \tag{2.9}$$

taking into account that the in-plane strain s_x is equal to the perpendicular in-plane strain s_y.

For small strains (i.e. low applied voltage), two approximations can be made. First, the electrostatic force increase due to the thickness reduction can be neglected, which means that we don't take into account the E field's dependance on the deformation. Equation 2.8 can be rewritten:

$$s_{z0} = -\frac{\epsilon_0 \epsilon_r V^2}{Y z_0^2}, \tag{2.10}$$

where s_{z0} is the approximated thickness strain, and z_0 the initial thickness of the elastomer, in the absence of an electric field. The second approximation consists in neglecting the second order terms in the incompressibility equation (eq. 2.9), which leads to the following relations describing the in-plane deformation:

$$s_a = -s_z$$
$$s_x = s_y = -\frac{s_z}{2}, \tag{2.11}$$

where s_a is the surface strain.

For larger deformations, the increase of the electrostatic force with the thickness compression cannot be neglected. In that case equation 2.8 must be used and can be transformed as follows:

$$s_z = -\frac{\epsilon_0 \epsilon_r V^2}{Y z_0^2 (1 + s_z)^2} = \frac{s_{z0}}{(1 + s_z)^2} \tag{2.12}$$

This third order equation has three solutions, but one is physically impossible and another describes an equilibrium position which is not mechanically stable.
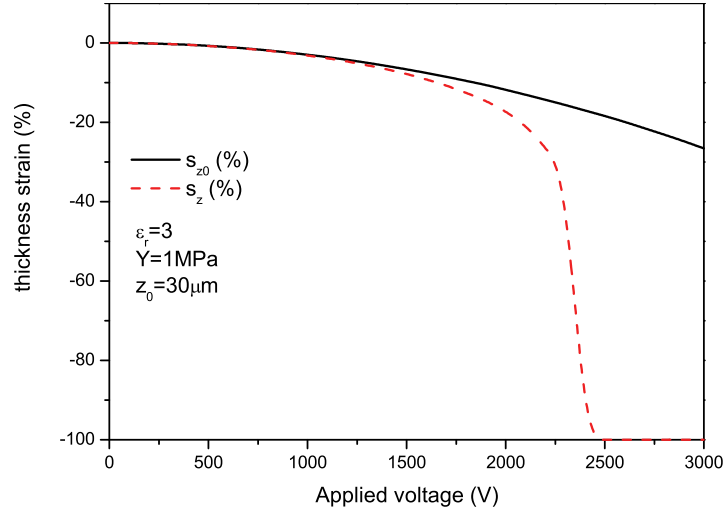
---

[1]$s_z = (z - z_0)/z_0$

Figure 2.5: *Calculated approximated (s_{z0}) and real (s_z) thickness strain for a DEA with $\epsilon_r = 3$, $Y = 1$ MPa and $z_0 = 30$ μm as a function of applied voltage.*

The true value of s_z is:

$$s_z = -\frac{2}{3} + \frac{1}{3}\left(\alpha + \frac{1}{\alpha}\right)$$

$$\alpha = \sqrt[3]{\frac{2}{2 + 27s_{z0} + 3\sqrt{3}\sqrt{4s_{z0} + 27s_{z0}^2}}}. \tag{2.13}$$

It should be noted that α is a complex number, but s_z is purely real. An example of thickness deformation calculated with the two models is shown on figure 2.5. The approximation (eq. 2.10) gives acceptable values for strains up to -6%. For higher strains, the complete expression for s_z (eq. 2.13) must be used. The graphical representation show that the model predicts a pull-in phenomenon for strains higher than 33%, similar to what can be observed for air-gap capacitors [22]. When pull-in occurs in a DEA, it causes a dramatic increase of the electric field which leads to dielectric breakdown and failure of the device.

The above model assumes that the Young modulus does not depend on the deformation. However, elastomers have a stress-strain behavior which is hyperelastic and non linear: their strain-stress behavior derives from a Helmoltz free-energy function which only depends on the strain tensor [23]. Many hyperelastic models have been developped to describe large deformations of elastomers: Neo-hookean, Yeoh, Ogden, Mooney-Rivlin, etc [24]. Some non-linear models also consider the visco-elastic behaviour of some elastomers, which is the time-dependance of the deformation response due to applied stress. Because of the hyperealsticity, the s_z calculated with the Hookean (elastic) model (eq. 2.13) will be overestimated for large strains ($> 20\%$).

2.4 The prestretching of dielectric elastomer actuators

It has been observed that pre-stretching the material before applying actuation (typically 100%-500%) greatly enhances its performances (see e.g. [2,3,16]). The advantage of the prestreching mainly resides in the fact that the functioning point of the actuator is shifted in the hyperelastic zone of the material, which causes an important increase of the Young's modulus with strain. This prevents pull-in to occur and allows to overcome the 33% thickness strain limit leading to area strains above 200% [2]. A further strain increase can be obtained by the pre-stretching's ability to increase the maximal field that can be applied to an elastomer before dielectric breakdown. The reason behind this is not fully understood but is attributed to alignment of polymer chains due to the directional strain [3]. However, at small voltage levels (i.e. small strains), prestretching is not advantageous, as it increases the Young's modulus, hence causing a strain reduction. The important strain increase reported in litterature (see e.g. [2, 16]) is in fact mostly due to the thickness reduction induced by the prestretching: At a given voltage, this increases the electrical field, and therefore, the deformation strain. However, a 100 μm-thick elastomer layer biaxially stretched by 100% in x and y will deform less than a non-prestretched 25 μm-thick layer when submitted to the same moderate voltage. At higher voltages, the non-prestretched actuator will fail due to pull-in, whereas the prestretched one can overcome the 33% strain limit.

Prestretching is mainly necessary for acrylic DEAs, as the material commonly used (VHB adhesive, by 3M) has high initial thickness (50 μm and up). Additionally, acrylic elastomers suffer from viscoelastic behavior, which slows down their response speed [2], and prestretching has been observed to reduce this problem. However, pre-stretching reduces the shelf life of the actuators, as any defect that exists in the dielectric layer will be propagated by the high strain energy stored into the elastomer [25]. A detailed study on prestrain by Choi et. al. has shown that the only true benefit of prestraining DEA films is the increase of the breakdown field [26].

2.5 Polymers for dielectric elastomer actuators

There are two main categories of elastomers which are widely used in DEAs: silicones and acrylics [6]. When SRI started their research on EAP, they tried all kind of rubbery material to see which of them could produce large strain outputs [3]. Acrylic elastomers and silicones were seen to be the best performing. Among the different research groups, there seems to be a preference for acrylic elastomers, mainly 3M VHB 4905 and 4910 (respectively 0.5 mm and 1.0 mm thick) [2, 11, 17, 24, 25, 27], as they are capable of larger strains than silicones and are available in the form of ready-to-use polymerized sheets. However, their important thickness, low breakdown voltage and viscoelastic characteristics render the use of prestreching compulsory.

Silicone-based elastomers, mainly Polydimethylsiloxane (PDMS), are also widely used. Nusil CF19-2184 (Nusil), Sylgard 186 and HS3 (Dow Corning) are three examples of PDMS that have mechanical and electrical properties suitable for DEAs applications [2, 15, 19]. PDMS layers are produced by mixing two different components that cure and form an elastic layer. This allows to

easily produce sheets of different thicknesses without using prestretching. Very thin layers ($2 - 50$ μm) can be obtained by spin coating, similarly to what is done to dispense photosensitive resists for microelectronics or MEMS fabrication processes. This renders the production of thin PDMS layers compatible with microfabrication technologies and equipment. Compared to acrylic elastomers, silicone conserve their elastic propertied on a large range of temperature (-50° C to $+200^o$ C). Consequently PDMS was used throughout this project, which enabled the creation of stable and robust elastomeric films of tunable thickness, without external prestretch. Two different PDMS types were used: *Nusil CF19-2184* from Nusil, and *Sylgard 186* from Dow Corning. A third silicone, *Dragon Skin* from SmoothOn, was used for the first proof-of-concept devices, but was then discarded due to a low breakdown voltage [28] and a low Young's modulus (a DEA made with an elastomer that is very soft will have high strain capabilities, but very low output forces).

Chapter 3

Ion Implantation

Generally speaking, ion implantation is a material engineering process by which ions of a material are *implanted* (i.e. injected) in a target material, thus modifying the physical properties of the target. The main parameters that characterize an implantation are: the incoming ions species, their energy (eV), the composition of the target, the angle of incidence – which will be considered perpendicular to the target surface (0°) for the remaining of this document – of the ions, and the implanted dose ($ions/cm^2$). The first four parameters influence the depth profile of the implanted ions inside the target, and the last parameter defines the volumic density of the implanted species (i.e. the quantity of implanted ions) (Fig. 3.1).

One of the most common applications of ion implantation is the introduction of dopants into a semi-conductor in order to modify its electrical properties. In that case, the implanted ions are typically boron, phosphorus or arsenic, and the target can be silicon (Si) or other semi-conductors such as III-V compounds. Implantation of oxygen ions into silicon is also used in the SIMOX (Separation by Implantation of Oxygen) process to produce silicon on insulator (SOI) wafers [30].

The broad range of energies and ion species involved in ion implantation cannot be met with a single type of implanter. Three main categories can be defined among the ion beam lines implanters: high-current, medium-current and high-energy implanters [31]. High-current implanters can produce ion current up to 25 mA, but at rather low energies (1-200 keV) and are targeted for high-dose application. At the other end, high-energy implanters can produce ions accelerated at several MeV, but with rather low current. Appart from conventional beam-line implanters, there also exists plasma based implanters, such as vaccum arc plasma sources, or plasma immersion ion implantation (PIII) [32], that are, for example, well adapted to the implantation of metal ions with a large flux.

3.1 Ion implantation into polymers

Alteration of polymers' properties (chemical, structural, mechanical, electrical...) by ion implantation is a growing area of research. Most of the literature published in that domain concerns implantation of light elements (N, H, Ar, etc) on relatively hard polymers (PET, PI, ...), and at rather high energies (a
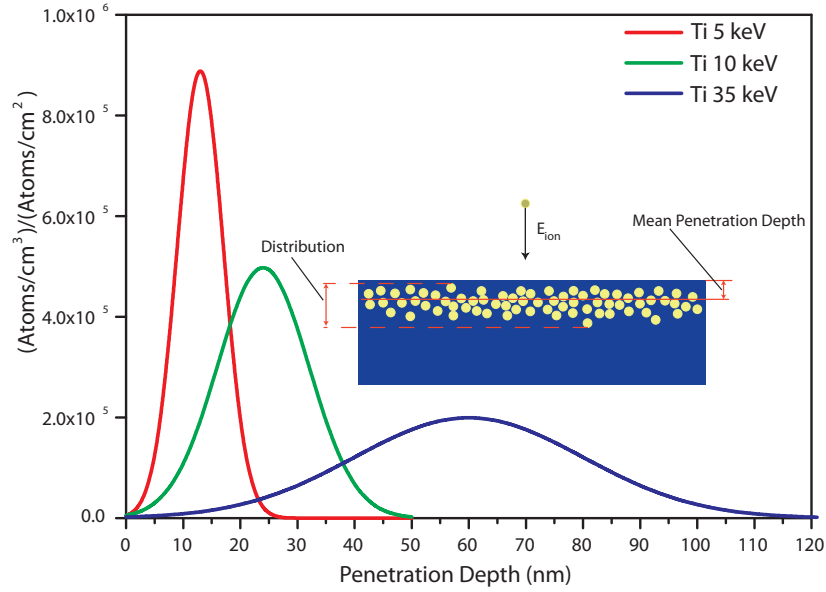
Figure 3.1: *SRIM [29] simulation of titanium ions penetration into PDMS for three different incoming energies (5, 10 and 35 keV). An increase in energy leads to a deeper mean penetration into the PDMS and to a larger dispersion of the ions. The lowest energy allows to obtain a dense layer of ions close to the surface. The vertical axis represents the Ti volumic density obtained per incoming ion dose.*

few hundred keV to several MeV [33–36]. For example, implantation of Ar^+ ions at 600 keV into poly-iso-quinazolindione (PIQ) transformed an insulating 1.3 μm-layer into a semi-conducting compound for doses between $1 \cdot 10^{14}$ and $2 \cdot 10^{15}$ at/cm^2 [34]. The high energy used in this application allowed to obtain a large penetration depth, estimated at 700 nm.

Relatively few publications report on implantation of metallic particles into polymers, and those which do are targeted on hard polymers, such as PET [37, 38]. Physical changes are observed with colors varying from transparent for unimplanted PET to bright metallic depending on dose. A sharp decrease of the resistivity is observed [38], coupled with an increase of Young's modulus, surface hardness and wear resistance [39–41], as well as with a modification of surface roughness [42].

3.2   Ion Implantation for Dielectric elastomer actuators

If the literature on metal implantation into polymer is sparse, publications on metal implantation into elastomer are quasi nonexistent. As elastomers used for DEAs are very soft, heavy metallic ions can easily penetrate into the polymer matrix. Consequently, low ion energies must be used to keep the ions close to the surface, as required to create electrodes for DEAs. Monte Carlo simulations were used to estimate the ion range into PDMS, with a program

named SRIM [29]. The optimal energy was found to be between 2 and 8 keV, for a penetration depth of a few tens of nanometer (Fig. 3.1).

In addition to a low energy, the implantation must be conducted with a high ion flux in order to reach the desired dose $(1 \cdot 10^{16} - 5 \cdot 10^{16} \text{ at/cm}^2)$ in a reasonable amount of time. Unfortunately, typical classical (ion beam) implantation machines have a very low ion flux at low energies and can hardly produce a stable beam below 10 keV. When implanting metal ions into soft elastomers at energies of 10 keV or above, the ions cannot be confined close to the surface, and the implantation time can become very long in order to reach a volumic density of metallic particles high enough to create a conductive layer. This leads to implantations lasting from a couple of hours to several days, which makes these implanters practically and economically unsuitable for our application.

Consequently, a plasma-based technique of implantation based on a pulsed vacuum arc plasma source was selected to make the implantations, and an experimental implanter was built, due the difficulty to find a project partner possessing the needed equipment and willing to allow the use of polymer inside the chamber.

3.3 Filtered Cathodic Vacuum Arc

Vacuum arc plasma implantation is mainly used to apply wear-resistant coatings on cutting tools, but also has many other applications, such as the deposition of multilayer metallic thin-films [43], transparent conducting layers [44], or spectrally selective transparent coatings [45].

In vacuum arc plasma systems, the plasma is generated by a high-current electrical arc between a metal – or any other conducting material – source (cathode) and a counter electrode (anode). The major downside of arc-created plasma is the presence of macroparticles of sizes up to a few micrometers in the plasma [46]. For many applications, it is highly undesirable for those particles to reach the target's surface, as it lowers the quality and density of the implanted/deposited layer. When implanting PDMS for DEA applications, it would contribute to create a metallic layer on the surface, which is precisely what needs to be avoided in order to ensure the compliance of the electrodes. A conventional way to remove these particles is to take advantage of their very low charge over mass ratio and to place a bent magnetic filter on the plasma path [44, 47–50]. This filtered version of vacuum arc plasma was pioneered by Aksenov in the late 70s [51] and developed mainly by Brown et al. at Lawrence Berkeley Laboratory [43, 44, 46–48, 52–55]. It is commonly called *Filtered Cathodic Vacuum Arc* (FCVA).

FCVA is a technology which is well suited for the implantation of PDMS aimed towards the fabrication of DEAs. The dense plasma flux ensures a high ion current, which brings short implantation time. FCVA can be used without any external acceleration potential, in which case the ion energy is only due to the pressure gradient generated by the arc creation inside the vacuum chamber. The ions are accelerated to a speed of $5 \cdot 10^3 - 2 \cdot 10^4$ m/s, nearly independent of the cathode material [43, 56], and represents an energy of 25–200 eV (49 eV for gold [56]). A negative potential can be applied on the substrate holder to further accelerate the ions to greater energy, for example in the 2–8 keV range,
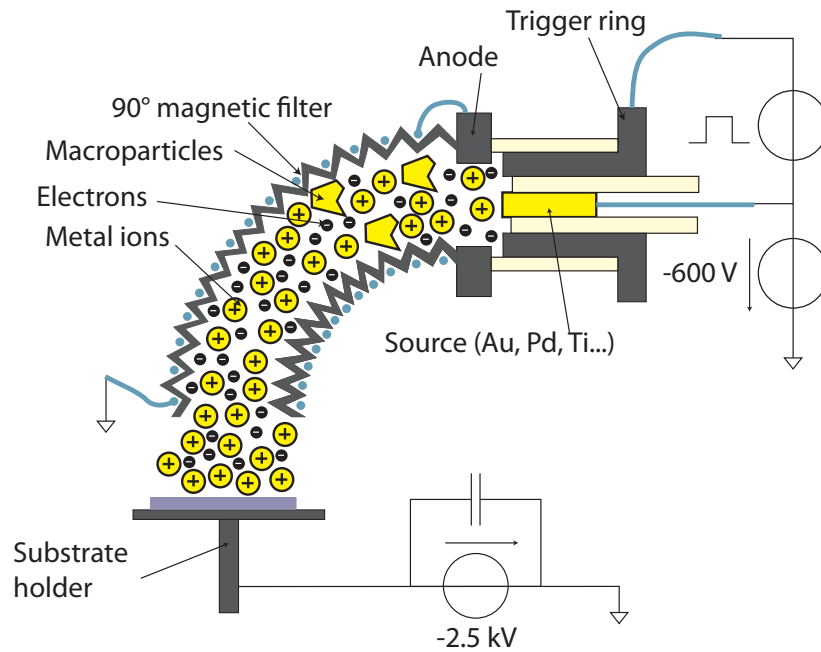
Figure 3.2: *Schematic representation of our FCVA implanter. A high voltage impulsion on the trigger electrode initiates the main arc between the source and the anode. The electrons, ions and macroparticles produced by the arc enter the filter which traps the unwanted macroparticles. The substrate holder is negatively biased to accelerate the positive ions through the plasma sheath.*

which is particularly adapted to our application.

A FCVA system is formed by a plasma gun, a magnetic filter, and electronics to generate the electrical signals. Most FCVA equipments work in pulsed mode, but there also exists continuous-mode apparatus. Operation of the plasma gun takes place in high vacuum ($\sim 10^{-6}$ mbar). In our pulsed system (Fig. 3.2), a charged capacitor tank applies 600 V between the anode and the source (cathode). The generated electrical field between the two electrodes is smaller than the breakdown field in vacuum. Hence, no current is flowing between the two electrodes. The arc is initiated by a high voltage pulse ($10 - 18$ kV) on the trigger electrode, which is situated in close proximity of the cathode. This small plasma initiates the main arc between the cathode and the anode, which discharges the tank capacitor in 600 μs with a current of 50–100 A, leading to the production of a dense plasma of the cathode material.

The electro-magnetic filter consists of a 90° bent flexible vacuum bellow, around which a 15-turns coil is wound. The coil is serially connected with the anode terminal, thus automatically producing the steering magnetic field during the arc duration. The downside of this configuration is the impossibility to finely control the arc current (i.e. the guiding field), which depends on the arc voltage, as well as cathode material and erosion. On the other hand, as plasma triggering may be difficult in presence of strong magnetic fields, this serial configuration facilitates the creation of the plasma: the trigger behavior
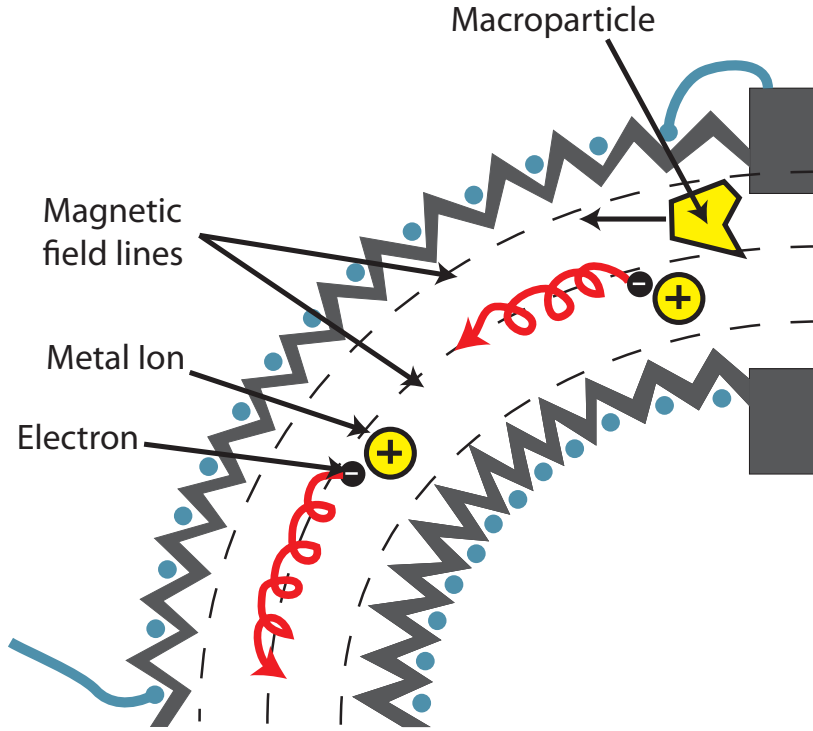
Figure 3.3: *Filtration principle. The magnetic field strength (typ. 20 −
100 mT) is such that the diameter of the filter duct is much smaller than
the metallic ions' Larmor radius, and much larger than the electron's gyration
radius. The magnetized electrons guide the ions through attractive Coulomb
forces, and the macroparticles remain unaffected due to their heavy mass and
small charge.*

is the same as with a vacuum arc without magnetic field [46].

The filter's principle is based on the magnetic confinement of the electrons
in the filter, and the guiding of the positive ions by the electrons through the
attractive Coulomb electrostatic forces (Fig. 3.3). When the plasma, moving
at $1 - 2 \cdot 10^4$ m/s, enters the filter, the magnetic field in the duct will affect
the electrons much more than the ions. Indeed, as the magnetic field in the
filter is typically between $20 - 100$ mT, the diameter of the filter duct (2 cm)
is much smaller than the metal ions' Larmor radius, and much larger than the
electron's gyration radius. The electron's Larmor radius (r) is given by [44]:

$$r = \frac{\sqrt{m_e k T_e}}{eB},\tag{3.1}$$

where m_e is the mass of the electron, k the Boltzmann constant, T_e the electron
temperature, e the elementary charge, and B the magnetic field. Assuming a
typical electron temperature of 3 eV [44], this leads to gyration radius around
100 μm. The gyration radius of the positive ions is several order of magnitude
larger due much higher masses and lower temperatures. Consequently, elec-
trons are magnetised, but ions are not. During the arc, a cloud formed from

electrons, ions, and macroparticles is ejected from a cathode spot and expands due to the pressure gradient, while moving towards the filter. The particles' speed vector has therefore a non-null component perpendicular to the guiding magnetic field, which induces the gyration of the electrons while they move towards the exit of the filter. The electrons are confined at the center of the filter duct, and so are the positive ions, because of Coulomb interactions in the plasma. The macroparticles are unaffected by the magnetic field and the electrostatic forces, and they follow their straight trajectory until they hit the duct's wall.

It is not crucial to precisely control the guiding field's amplitude, as long as it is high enough to confine the electrons in the filter. Anders et. al. demonstrated that the filter's efficiency increases with increasing guiding field [43], which we can only indirectly control by changing the arc voltage. A fully decoupled system, with the arc pulse completely separated from the generation of the guiding field would enhance our ability to improve the filter's efficiency, which is estimated at a few percent only. Anders et. al. have also studied the strong influence of the duct's bias on the filter's efficiency, as well as the addition of a focusing field at the filter's entrance [43, 44, 47], which are two features not present on our system. They have also noted that the filter's efficiency was dependant on the cathod material; we have also observed this phenomenon, with a much lower efficiency for gold than for palladium or titanium. Variation of the ion flux at the duct's output with the element type is principally attributed to the ratio of ions over macroparticles, which increases with increasing fusion temperature [52].

3.3.1   From plasma generation to implantation

Because of its complex behavior, extracting and accelerating ions from a neutral plasma is not straightforward. Two different methods dominates: extractor grids and plasma immersion implantation. Extractor grids are used to produce a pure ion beam out of a plasma, for example in metal vapour vacuum arc systems. The plasma is created at a high potential and confined in a chamber by a set of three extractor grids differently biased whose purpose consist in confining the plasma, suppressing the electrons, and accelerating the positive ions [57]. Such ions sources were developed to inject heavy ions into particle accelerators [58], and can be applied to FCVA sources [52]. Although this method ensures that a pure beam of ion reaches the surface of the sample, it requires precise adjustments of the extractor grids (plasma potential, grid spacing, and mesh size) in order to obtain a good extraction efficiency [59].

The second dominant method is plasma immersion ion implantation (PIII) [60]: the substrate to be coated is immersed into a stationary plasma whose potential is close to ground. A square pulsed negative potential is applied to the substrate to accelerate the ions. During the active part of the pulse, a plasma sheath is created around the substrate. The high potential difference between the plasma and the substrate creates a strong electric field in the sheath, which accelerates the positive ions towards the target: implantation takes place (Fig. 3.4). The sheath width expends with time, due to charge depletion caused by the E field, eventually leading to full depletion and breakdown between the HV electrode and grounded parts of the vacuum chamber [55]. Consequently, PIII is used with a pulsed negative potential on the substrate. During the
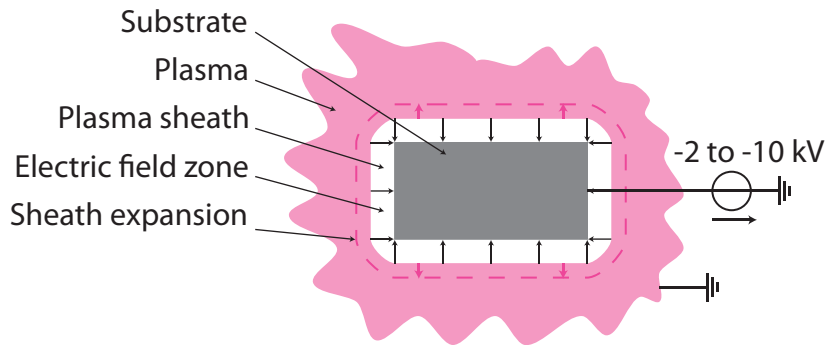
Figure 3.4: *Schematic representation of PIII implantation. During the HV pulse, a plasma sheath is created around the substrate. The electric field in this sheath accelerates the plasma's positive ions towards the substrate. At the same time the sheath expands due to charge depletion. The high voltage is pulsed to allow for plasma recovery.*

non-active part of the cycle, the plasma can recover for the next polarized phase. As a matter of fact, PIII is a two phases process, with implantation taking place during the polarized part of the cycle, and deposition taking place during plasma recovering. The ratio of implantation over deposition depends on the duty cycle of the high voltage pulse, which typically varies between $10 - 50\%$. The pulse parameters must also be chosen to avoid plasma depletion and electric breakdown. Pulsed HV biasing is easily applicable to metal vapor plasma created with FCVA sources [53, 61].

However, there is an important difference between FCVA and standard PIII: In PIII, the plasma has usually a negligible or very small drift velocity, whereas in the case of cathodic arc, the plasma plumes away at a speed of $1 - 3$ cm/μs. In this situation the plasma sheath expansion away from the substrate is compensated by plasma motion towards it. Consequently a high negative potential can be held during an extended period of time, thus leading to pure implantation, similar to what could be obtained with a MEVVA source with extractor grids. Brown and coworkers were able to hold voltages up to -10 kV during implantation pulses of 10 ms, but extreme care had to be taken on the substrate's shape, which had well rounded corner to prevent breakdown [53, 55]. It is therefore possible to achieve pure implantation of metallic ions with an FCVA setup such as the one represented on figure 3.2.

3.3.2 Our filtered cathodic vacuum arc system

Our experimental FCVA system (Fig. 3.5) is based on RHK Technology[1] *ARC 20* pulsed arc source. It can be fitted by any conducting source material in the form of ⌀3 mm by 15 mm cylinders. This small source size is well suited for research purposes, as expensive metals and alloys can be tested for a relatively low cost. Titanium, gold, and palladium implantations were used for the present work. The arc duration is ~ 600 μs and the pulse rate can be set
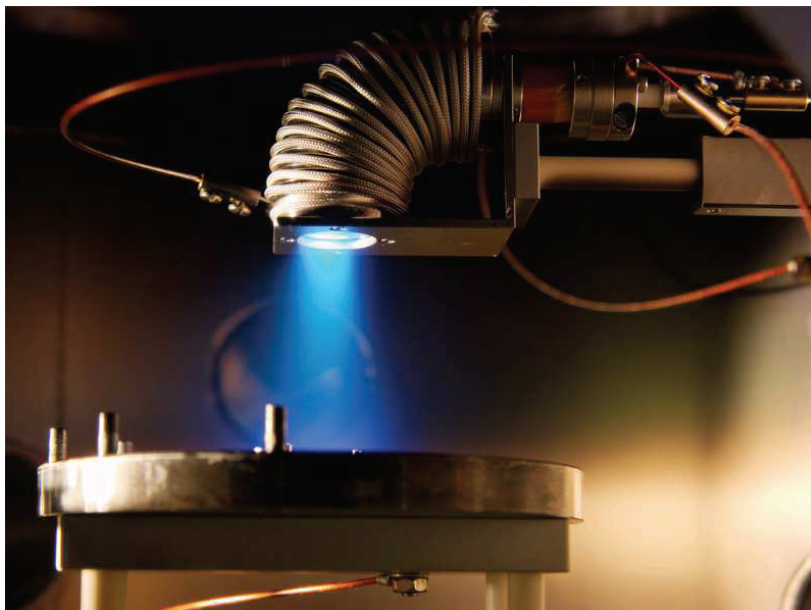
---

[1] www.rhk-tech.com

**Figure 3.5:** *Picture of our FCVA implanter during a pulse*

between $0.01 - 50$ Hz. Practically, pulse rates between $0.5 - 2$ Hz are typically used.

The implantation spot has an estimated surface of 1 cm^2 with a Gaussian concentration profile. To compensate for the small implantation area and its inhomogeneity, a motorized x, y scanning stage was added to our implanter, which allows homogeneous implantation on substrates up to $\varnothing 10$ cm. This 2D scanning is achieved by having the substrate holder moving on an axis (x), and the plasma gun moving on a perpendicular axis (y).

The energy is controlled by a high voltage source which can apply a potential between 0 and -5 kV on the substrate holder. Our aim is to achieve pure ion implantation by holding the negative potential during the whole pulse length (cf. subsection 3.3.1). Plasma generation by the arc leads to the creation of ions with different charge states (Tab. 3.1). Hence there is an energy distribution among the ions reaching the substrate (Fig. 3.6), but for the three tested elements (Au, Pd, Ti), the mean charge is $Q_{avg} \approx 2.0$ e, leading to an average ion energy twice the absolute value of the acceleration potential, if the voltage on the substrate does not fluctuate. However, we fail to hold the negative potential during every pulses. As Brown et. al. noted [53, 55], two modes are observed during the implantation pulses: some pulses behave as expected, with the current drawn from the HV capacitor corresponding to that of the ion current. The second mode which is observed is a breakdown, with the capacitor being completely discharged in a few microseconds. This is due to breakdown through the plasma sheath: electrons are pulled out of the substrate's surface and injected into the plasma. This behavior must be avoided when implanting thin PDMS membranes, as the resulting high current can damage the membranes. We have consequently added a resistor to limit the current drawn in case of breakdown, at the cost of a larger voltage fluctu-

Table 3.1: *Charge state fractions of Au, Pd, and Ti ions generated by vacuum arc, as well as mean ion charge (Q_{avg}) (from [54]).*

Element	Q=1+ (%)	2+ (%)	3+ (%)	4+ (%)	Q_{avg}
Gold	14	75	11		2.0
Palladium	23	67	9	1	1.9
Titanium	11	75	14		2.1
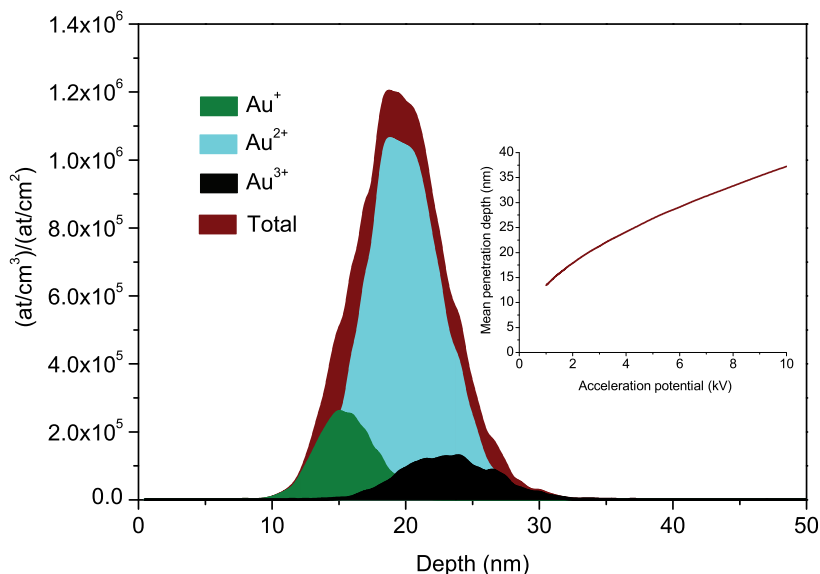
Figure 3.6: *SRIM [29] simulation of the volumic density versus penetration depth of Au ions with the charge repartition given in table 3.1. The mean penetration depth is dominated by the doubly charged ions.*

ation of the substrate's holder potential, which leads to a broad ions' energy distribution during a pulse.

We are currently in the process of solving this issue, but it is not clear at this time if limiting the energy spread will be beneficial for our application. All the encouraging results presented in this document were obtained with a fluctuating potential, and it is possible that the resulting broader ion distribution which extends up to the elastomer's surface takes an active part to the observed mechanical and electrical behavior. Having the ions extending up to the PDMS' surface eases the electrical contact of the electrode, which would be more difficult with a completely buried layer.

The implanted dose (i.e. quantity of implanted atoms per surface ares) is the second important parameter to control in order to finely tune the mechanical and electrical properties of the implanted layer. However our implanter only offers an indirect way to control the dose through the selection of the number of pulses (i.e. arcs). The link between the number of pulses and the dose was established by conducting RBS analyses on samples implanted with a different number of pulses (Fig. 3.7). This calibration allows to determine the number of pulses required to reach a desired dose for each of the three tested metals. The
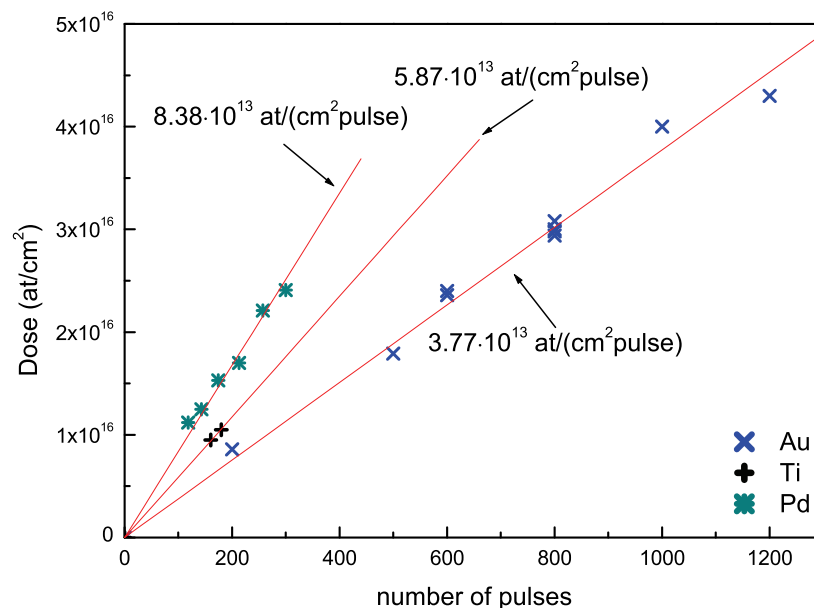
Figure 3.7: *The correlation between the number of pulses and the implanted dose was established with RBS analyses. The slope of the linear regression gives the implanted dose per pulse for the three tested metals.*

Au datapoints are particularly interesting, as they come from three independent sets of implantation. Between each set, the source was either changed or was at a different wear level. Nevertheless all the points align along the same line, meaning that the output flux of the plasma gun is not sensitive to precise positioning or source erosion.

The ion-beam has a gaussian shape and the quantity of implanted ion on a small surface area depends on the surface element's distance from the beam's center. Because the RBS analyses on our implanted layers had to be conducted with a broad unfocused beam to avoid damaging the polymer, the obtained value is an averaged dose for the analysed surface. However, bulge test measurements (cf. subsection 5.3.4) sometimes show different Young's modulus values for membranes situated on the same chip, if it was not properly centered relative to the ion beam. The motorized xy stage, which was primarily installed to implant surfaces larger than the beam's size, can also advantageously be used when implanting surfaces smaller than the ion beam, in order to obtain a better dose homogeneneity on the treated surface.

For a scanned implantation, the user defines the area to implant, and the pulse density (i.e. the number of arc pulses per surface unit, Fig. 3.8). The total number of pulses is therefore defined by the pulse density multiplied by the scanned surface. The homogeneity of the implantation depends on the spacing between pulses relative to the beam diameter, which depends on the desired dose (i.e. pulse density): the higher the pulse density, the smaller the spacing between pulses, therefore leading to a better homogeneity.

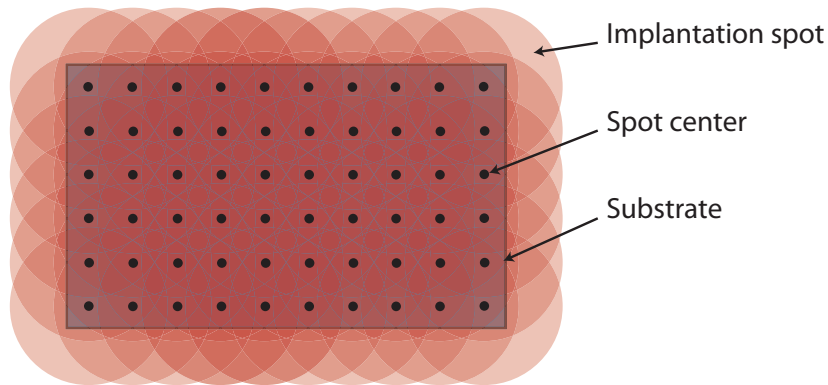The RBS calibration made on samples implanted with the scanning system

Figure 3.8: *Illustration of the scanned implantation. The plasma gun is moved at a constant speed over the substrate of area A. Implantation is pulsed at a constant rate, thus creating an homogeneous implantation on the substrate. To ensure homogenetiy on the whole substrate, the implanted zone should be chosen slightly larger than the substrate. The implantation is characterized by the number of pulses divided by the area A. The pulse density depends on the scanning speed and the pulse rate.*
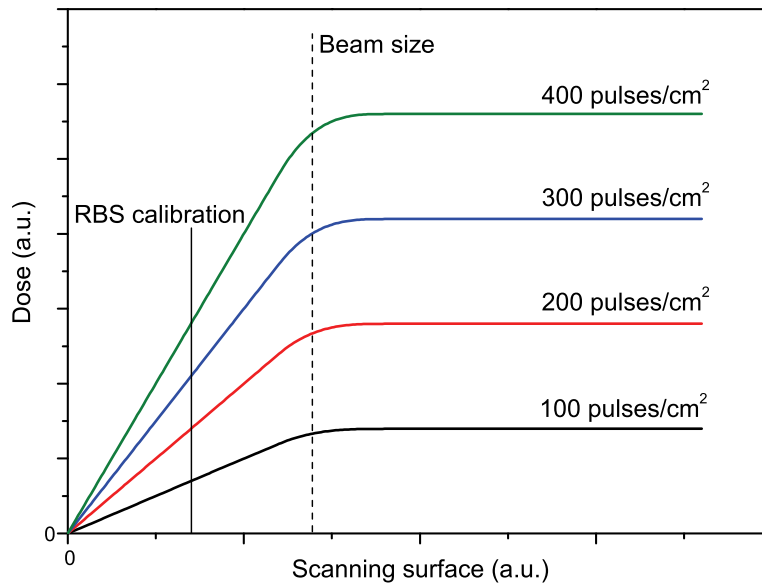

Figure 3.9: *Dose as a function of scanned surface for different values of pulse density. For large scanned surfaces, the dose is independant of the scanned surface, which is not true for surfaces smaller than the beam size. RBS calibrations made for a scanned surface smaller than the beam size are only valid when scanning the same surface area. RBS calibration made for scanned surfaces larger than the beam size remain valid if a different area (but larger than the beam's area) is scanned.*

gives the number of atoms per surface area (the dose) for a given pulse density
that was used to implant the sample. In other words, for a given metal, the RBS
calibration gives the number of implanted metal atom per pulse. By selecting
a pulse density, one should obtain the same dose for any given surface area.
However, this reasoning is correct only for scanned areas much larger than
the beam surface. In the case of implanted surface smaller than the beam's
size, a different RBS calibration should be made for several different surface
sizes in order to be able to correctly estimate the dose for any implantationed
surface (Fig. 3.9). The beam's size being different for each metal, and hard to
determine due to the lack of a clear border, this calibration should be made for
each metal. Due to the number of involved RBS analyses and the impossibility
to carry out these measurements ourselves, this general calibration has not been
made. Consequently, the dose will be given in at/cm^2 only if the implantation
was made in the same condition than the corresponding RBS calibration. In
the other cases (e.g. the strip's for the strain measurement, subsection 5.2.3),
the dose is given in pulses/cm^2.

Pulse-to-dose correlation for static implantations has also been conducted
inside the implanter with a Faraday cup (Fig. 3.10): The plasma gun is moved
above a Faraday cup with an opening of 1 cm^2, and a single plasma pulse
is triggered. The resulting ions are captured by the Faraday cup, while the
electrons are prevented from entering by a negatively biased grid at the cup's
entrance. The electrical current produced by the Faraday cup is converted to a
voltage with a 47 Ω resistor and monitored by an oscilloscope. By integrating
the current over the pulse's duration, it is possible to calculate the amount of
charges in a pulse, and to convert this number to a number of particles by using
the average charge of each ion, according to table 3.1. Due to some variation of
the quantity of ejected particles during a pulse, the measurement is conducted
on a certain amount of pulses, and averaged. Measurements with the Au source
have led to a dose per pulse value of $3.53 \cdot 10^{13}$ at/(cm$^2 \cdot$ pulse), which is in
good agreement with the $3.77 \cdot 10^{13}$ at/(cm$^2 \cdot$ pulse) obtained by RBS analyses
(6.3 % relative error). However, precise results are hard to obtain due to the
difficult alignment of the plasma beam with the Faraday cup. Additionally,
calibrating a scanned implantation is not possible with this method.

3.4 Metal ion implantation as a means to create compliant electrodes

Why does metal ion implantation on PDMS create a compliant electrode that
can be stretched without damage while remaining conductive, when cathodic
sputtering or e-beam evaporation lead to non-compliant layers? Why does de-
positing a metal layer on the surface of an elastomer lead to completely differ-
ent mechanical properties than implanting particles of metal a few nanometer
under its surface? The key point of ion implanted electrodes resides in the
fact that implantation will not form a continuous polycrystalline film in which
strong lattice forces bind the metallic atoms together within a grain, and grains
are attached to each other at the grain boundaries, thus forming a rigid film
capable of only a few percent strain before breaking. Ion implantation will
lead to the formation of small size (2 − 20 nm) clusters in the polymer matrix.
These clusters can touch each other (thus providing a conducting path) with-
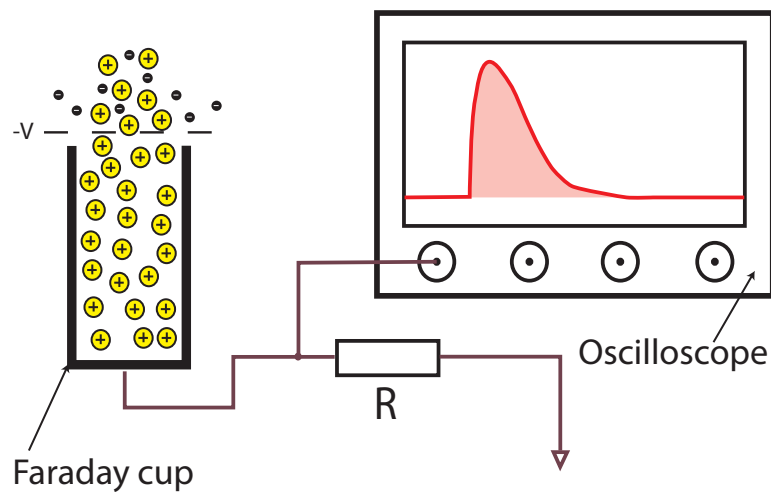
Figure 3.10: *In-chamber pulse-to-dose calibration with a Faraday cup. The ions are collected in a Faraday cup. The resulting current is converted to a voltage by a resistor, which is in turn recorded by an oscilloscope. Integration of the peak allows to extract the number of ions collected by the cup for one pulse.*
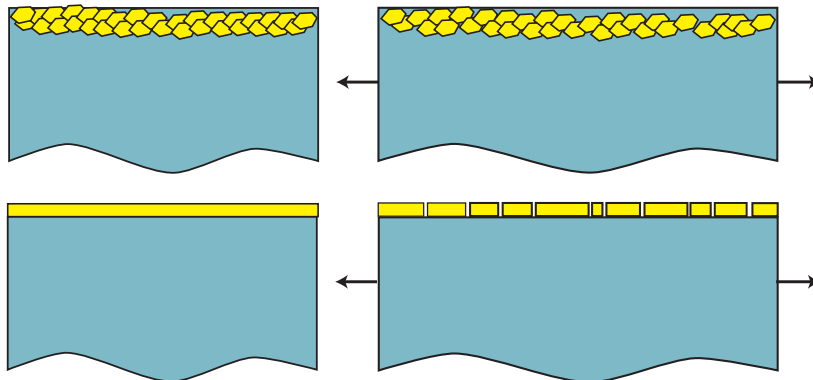

Figure 3.11: *Top: Schematic cross-section illustrating a compliant electrode obtained by ion implantation. The clusters are touching each other but can slide relative to one another. They can sustain large strain while remaining conductive. Bottom: non-compliant electrode obtained by thin film deposition. The strong binding forces which link the metallic atoms together drastically limit the achievable strain before damage to the electrode.*

out forming a strong mechanical bond. The absence of a strong bond between clusters allows them to slide relative to each other (Fig. 3.11). This leads to a reduced impact on the stiffening (increase of Young's modulus) of the PDMS due to the inclusion of the metallic particles, and to important strains before loosing conduction, as well as low degradation when cyclically stretched (cf chapter 5).
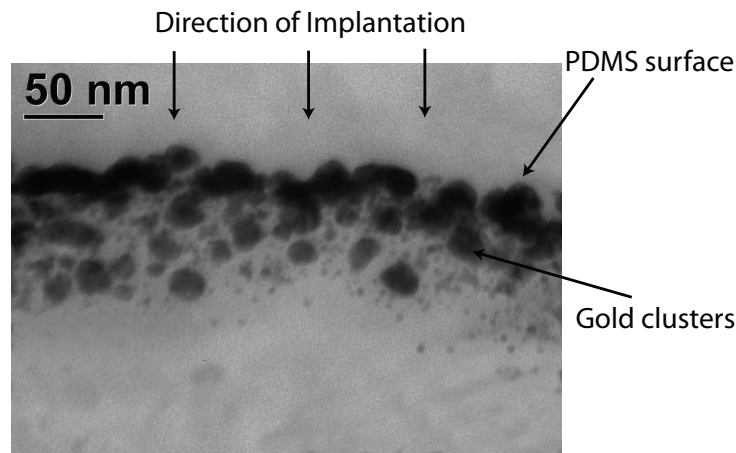
Figure 3.12: *TEM cross-section of Au-implanted PDMS (dose of* $1.5 \cdot 10^{16}$ *at/cm^2 at 5 keV), which shows Au atoms forming nm-size clusters when implanted into PDMS. The atoms extend from the surface up to a depth of about 60 nm below the surface [62].*

The existence of the nanometer-scale clusters that explain the compliance obtained by ion implantation has been verified by TEM cross-sections [62] (Fig. 3.12). Yuguang et. al. performed TEM cross-section observations on PET implanted at 79 keV with Ag ions [40]. They observed three different layers: a first layer without precipitates, a second layer densely packed with clusters, and a third layer with a decreasing concentration of Ag nanoparticles, which is in good accordance with the distribution expected from the simulations (see e.g. Fig. 3.1). The first layer is not present on our implantations, which present a non-null concentration at the surface of the PDMS. This can be explained by a lower implantation energy, and an energy decrease during the pulse (cf. subsection 3.3.2).

Implantation-induced damages in the PDMS causes degradation of the polymer matrix, mainly through chain scission and carbonization. Part of the electrical conduction in the implanted layer can be due to these damages, which would allow for current to flow between two non-touching clusters through carbon-enriched destructured polymer. Indeed implanting inert gas ions (e.g. Ar^+) into polymer can turn an insulating polymer into a conducting compound, through formation of a dense carbon network created by ion-induced damages to the polymer [34]. This phenomenon further increases the strain that can be applied to a metal-implanted layer before loosing conductivity.

An important part of the LMTS' project on ion-implanted DEAs is devoted to the study of the impact of the metal ion implantation on the structure of the PDMS and how this structure modification caused by implantation relates to the mechanical and electrical properties. Although cross-sections of implanted PDMS for TEM observation are extremely difficult to prepare, they are the key for a better comprehension of the measurements and observations presented in this report (cf. chapters 5 and 6). This part of the project is conducted by Muhamed Niklaus [62,63], and only briefly mentioned in this document.

3.4.1   Alternate ways to make compliant electrodes

In addition to the mainstream carbon-based electrodes traditionally used for DEAs (cf. section 2.1), and to low-energy ion implantation presented in this chapter, there are other alternate ways to make compliant electrodes on polymers; for DEA or other applications. Indeed the interest for stretchable or bendable electrodes is not limited to the field of DEAs, but covers a much larger area, including for example flexible and expendible displays [64], implantable sensors [65], or sensitive skins [66]. Depending on the application, the desired properties can vary widely, for example in terms of strain (from a few percents in case of slight bending, up to hundreds of percents for DEAs), or in term of number of sustainable cycles (from a single deformation during installation for an implantable sensor, to several hundred thousands of cycles for DEAs).

Gold thin-films, although not intrinsically compliant, can be used to make stretchable electrodes by exploiting compressive stress due to thermal coefficient missmatch between the metal and the polymer [67, 68]. The principle consists in depositing the thin-metallic film on a heated piece of polymer. When cooled to room temperature, the compressive stress generated at the interface will create periodic wrinkles of the metallic film. When submitted to strain, the wrinkles will first start to flatten. During this phase, there is almost no change in the resistance of the metallic track, as the total length remains the same. When the wrinkles have completely flatten, the metal layer is submitted to tension and the resistivity increases quickly up to the breaking of the metallic track. Lacour et al. report achievable strains of 23% with this method. This value was increased to 28% by depositing the gold on a pre-stretched elastomeric layer, in order to increase the wrinkles' amplitude [69]. The major downside of this technique is that it works best with narrow strips submitted to unidirectional strain parallel to the strip. Another approach with gold as a compliant electrode with good adhesion properties involves the use of a nanoporous Au layer [70]. However this method does not allow for easy patterning of the electrode.

Urdaneta et. al. have developed a chemical scheme to create stretchable electrodes by chemical reduction and diffusion of a Pt salt [71]. Advantages of this method include its intrinsic patternability by photolithography, very low initial (undeformed) surface resistance (2 Ω/square), as well as high strain capabilities (up to 70-150%). Unfortunately, important degradation of the electrode's resistance when cyclically stretched makes this method difficulty applicable to DEAs. Furthermore, the effect of the Pt salt in the polymer may have an important negative impact on the Young's modulus and the dielectric breakdown field of the elastomer.

As a final example, let us mention carbon nanotubes, that have been used to make electrodes for DEAs. Under certain conditions, these electrodes exhibit self-clearing (i.e. self-healing by vaporization of the electrode material) behavior in case of a dielectric breakdown through the PDMS, which prevents the destruction of the device [72]. This is a very interesting property for the reliability and lifetime of DEAs, but impact of the nanotubes on the mechanical properties of the elastomer must also be quantified to further assess the applicability of this method for artificial muscles.

Chapter 4

Fabrication processes

4.1 Polydimethylsiloxane preparation

Two PDMS with similar properties were used throughout this project: Dow Corning *Sylgard 186* and *Nusil CF19-2186*. Their preparation for spin-coating was done as follows:

4.1.1 Dow Corning Sylgard 186

Dow Corning Sylgard 186 is prepared according to the manufacturer recommendations, by mixing 10 parts of PDMS with one part of polymerizing agent. To lower the very high viscosity of the mixture (120 Pa·s), 0.9 part (47.4% wt.) of isooctane (2,2,4-trimethylpentane) is added to the PDMS and fully mixed, before being placed in a vacuum desiccator to remove the air trapped during the mixing process. The pot life is approximately 2 hours, therefore time is not an issue (spin coating is made in a clean room environment, whereas preparation of the mixture is conducted outside. Some time is therefore needed between the preparation and the coating). Depending on the application the mixture is spin-coated on silicon wafers, photoresist-coated silicon wafers, or flexible polyvinylidene chloride (PVDC) sheets. The thicknesses obtained on photoresist-covered Si for different spinning speeds are reported on figure 4.1. The curing time of Sylgard 186 depends on the temperature, ranging from one day at room temperature to 15 minutes at 150° C, and is slightly increased by the addition of solvent. The mechanical properties of the layer is dependant on the curing temperature (cf. subsection 5.3.3), and has been varied depending on the application and the desired final properties. Consequently curing conditions will be specified in the relevant chapters and sections.

4.1.2 NuSil Technology Nusil CF19-2184

Nusil CF19-2184 is a two-components (part A and B) PDMS with a 1:1 mixing ratio. It has a very short pot life (15 min), which complicates its usage, as the application must be executed directly after the mixing. Due to high viscosity of component A and B (respectively 90 Pa·s and 60 Pa·s), 37% wt. of isooctane is added to each of the two parts, which are separately prepared, degassed, and finally poured into the two tubes of a dispenser gun with a static mixer. The two parts are therefore stored separately, and mixed only
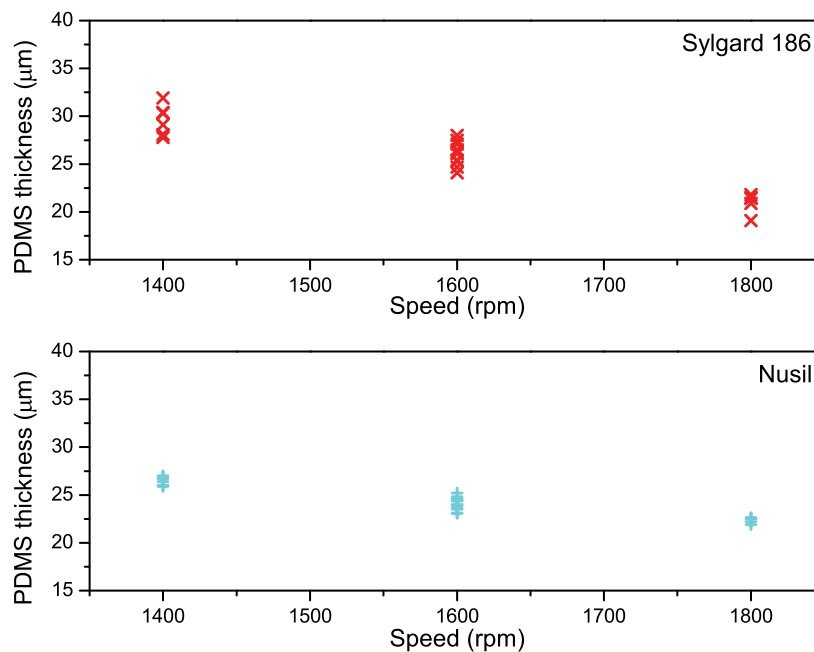
Figure 4.1: *PDMS thickness obtained by spin-coating Sylgard 186 (top) and Nusil (bottom) on photoresist-covered Si wafers. Both PDMS were diluted in isooctane as explained in subsections 4.1.1 and 4.1.2. The different datapoints for a given speed represent the thickness inhomogeneity over the wafer's surface.*

while dispensing the PDMS on the substrate, which allows to store the preparation for a few days before using it. Thicknesses obtained by spin-coating Nusil on photoresist-covered Si wafers at different speeds are reported on figure 4.1. Similarly to Sylgard 186, the layer's mechanical properties depend on the curing temperature, which will be specified in the relevant parts of this manuscript.

4.2   A few considerations on patterning

Most of the following sections of this chapter, describing the process flows concerning the different chips used throughout this study, mention the creation of *patterned* electrodes (either by sputtering or implantation). As a matter of fact, the possibility to pattern metal implanted electrodes is one of the many advantages of this technique compared to other methods to make electrodes for DEAs, and it opens the way to the miniaturization of artificial muscles, in order to make MEMS-DEAs. However, ion implantation is not intrinsically patternable, as the output beam of our implanter (~ 1 cm^2) is much too large to use it to define shapes. We must therefore use the standard patterning techniques of microfabrication in order to define the zones that are going to be implanted from the ones that will remain free of ions: photolithography and shadow masking.

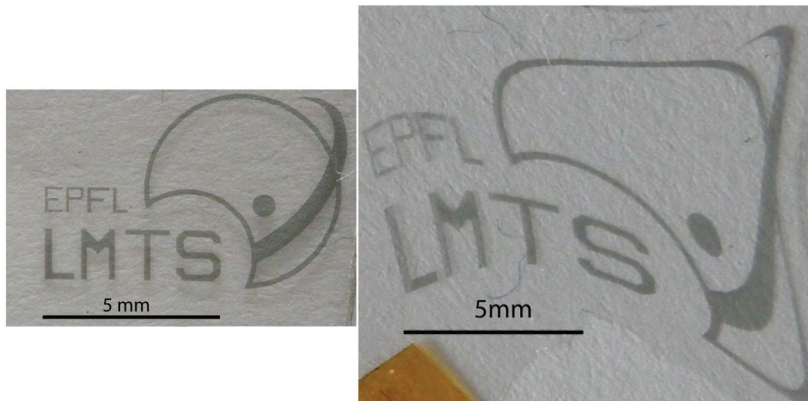Photolithography is the most versatile technique, allowing to define complex

Figure 4.2: *Left: undeformed Au implantation of the lab's logo, patterned by photolithography. The smallest dimension (43 μm for the EPFL letters' lines) and the annular shapes make it impossible to obtain this layout with steel shadow mask. Right: same as top, but stretched after implantation*

shapes with good resolution. A positive photoresist (PR) layer is spin-coated on the PDMS and selectively exposed to UV light through a mask. After being dipped into a devlelopment bath, the exposed parts of the PR are dissolved, thus reproducing the mask pattern on the substrate, with zones still covered by PR, and zones where the PDMS is exposed. Implantation is then conducted on the whole wafer's surface, but as the ion's penetration ($\sim$ 50 nm) is much smaller than the PR's thickness (> 1 μm), the PDMS zones that are covered with PR will remain free of ions. Removing the PR layer in an acetone bath leaves a PDMS layer which is selectively implanted.

Due to PDMS' high coefficient of thermal dilatation, the obtained resolution is lower than when patterning photoresist on silicon, but Pimpin and coworkers were for example able to pattern 45 μm wide tracks with interspacing of 10 μm on PDMS [19]. We have conducted some tests of patterning implantation on PDMS with photolithography and a PR mask. Our lab logo, which has lines as small as 43 μm, as well as annular shapes is a good example of a pattern which cannot be implanted with a steel shadow mask. The use of photolithography to create a PR mask on PDMS, followed by implantation and removal of the mask in acetone was successfully demonstrated with this test pattern (Fig. 4.2).

Unavoidable for high resolution patterns, photolithography is an overkill for our designs, which never necessitate resolution above 200 μm. It is also not easily applicable to chip-level fabrication, and the fact that most of our processes involve sacrificial layers that are soluble in acetone makes the use of a PR mask difficult.

We have consequently used steel shadow masks for all of our patternings. This technique has many advantages, such as re-usable masks, process rapidity, and the possibility to work on a single chip, rather than on the whole wafer. The main disadvantage of steel shadow masks is the shape limitation: If it is easy to make polygons, it is impossible to create annular shapes such as rings, or any shape involving islands. The steel masks were patterned by laser and consist of three layers: a plain bottom plate, a frame whose opening's size
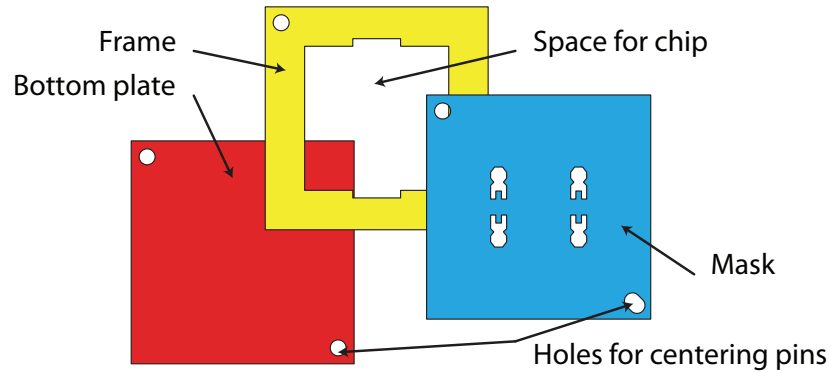
Figure 4.3: *Steel masks for our patterned implantations and sputterings consist of three parts: a bottom plate, a frame, which positions the chip on which the patterned electrodes are made, and the mask itself, which defines the pattern's shape.*

matches the chip to be patterned, and whose height is also equal to that of the chip, and finally the top layer in which the pattern is defined (Fig. 4.3). The three layers are held in place by pins on two diagonal corners, hence assuring positioning and alignment in the case where two or more masks need to be used for a process.

4.3   Chips for electrical resistance measurements

This section describes the fabrication process for the chips devoted to electrical resistance measurements, in order to characterize the electrical conductivity obtained for different implantation parameters (doses and metals).

They consist of a thin PDMS layer on a silicon chip and are fabricated as follows (Fig. 4.4): A $20 - 30$ μm-thick layer of PDMS is spin-coated on a 4" silicon wafer. As the PDMS' type, thickness and mechanical properties are not critical for this application, several variations of these parameters were used, without differentiation in the measurements. The coated wafer is then diced into 10×10 mm^2 chips, and gold electrodes are sputtered on the PDMS in a Balzers SCD-030 bench top sputtering system for 90" at 60 mA, leading to a thickness of ~ 15 nm. The spacing between the two electrodes is 0.5 mm wide on a length of 5 mm, thus defining a zone of 1/10 square. Implantation is then conducted through a steel shadow mask that defines an opening covering part of the two electrodes, as well as the space between them. The implanted layer's resistance was measured with a multimeter between the two gold pads. All implantations were conducted with an accelerating potential of -2.5 kV, leading to an implantation energy of distributed between 50 eV and 5 keV (cf. 3.3.2).

4.4   Samples for strain tests

The samples for strain tests (measurement of resistance vs. strain, degradation of the resistance with the number of strain cycles, etc.) consisted in ~ 200 μm-
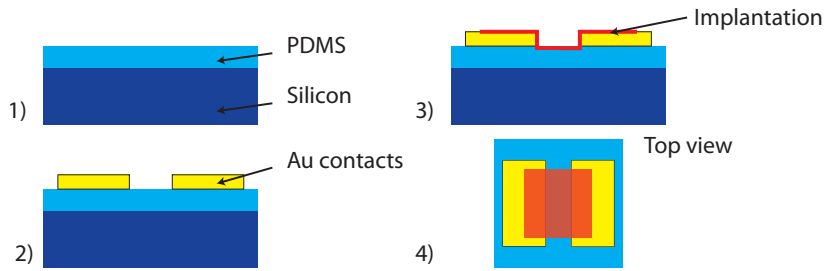
Figure 4.4: *Chips for resistance measurements. 1) A 20−30 μm-thick layer of PDMS is spin-coated on a 4" silicon wafer, which is then diced into 10×10 mm² chips. 2) Gold electrodes (∼ 25 nm) are sputtered on the PDMS through a steel shadow mask. 3–4) Implantation is finally conducted through a steel shadow mask.*
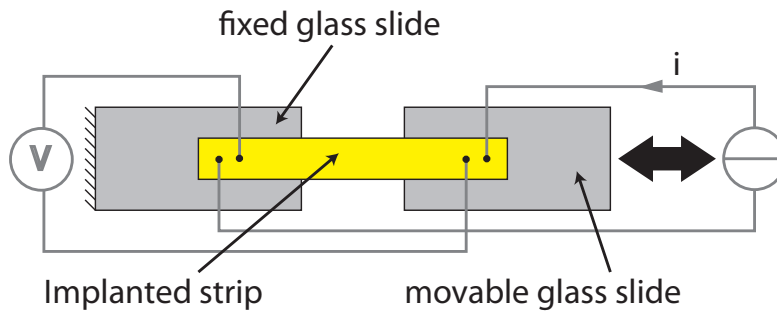

Figure 4.5: *Samples for strain tests: an implanted PDMS strip's extremities are glued to a microscope glass slide. Wires are then connected to the stripe for a four points resistance measurement.*

thick PDMS strips of a length of $6 − 20$ mm and a width of $3 − 5$ mm. The thickness was chosen so as to be able to easily manipulate the samples. To obtain this important thickness, the PDMS-isooctane mix was not spin-coated, but casted in a Petri dish and cured at room temperature. The strips were then cut in the Petri dish with a razor blade, laid on a glass microscope slide for mechanical support, and implanted over the whole area on one side. Each extremity of the strip was then glued to a glass slide and electrical connections were added (Fig. 4.5). This configuration ensured the electrical contacts remain free of mechanical stress and strain: any change in resistance while stretching the sample was therefore attributed to the implanted layer. Two wires were connected on each side of the strip, and 4-wires resistance measurements were performed in order to supress the influence of the contacts.

4.5 Chips for the measurement of dielectric breakdown

We have conducted extensive dielectric breakdown field measurements on implanted PDMS of varying thicknesses ($19 − 35$ μm). Samples were prepared in such a way that the capacitor zone in which dielectric breakdown occurs was free from mechanical deformation due to the application of the electrical
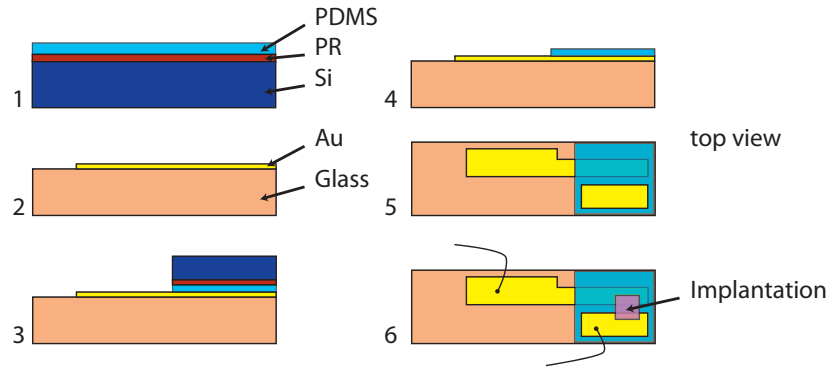
Figure 4.6: *Process flow for the fabrication of the dielectric breakdown test chips. 1) A PDMS layer is spin-coated on a PR-covered Si wafer. The wafer is then diced into 25×25 mm^2 chips. 2) A gold electrode is sputtered through a shadow mask on a microscope glass slide. 3) A Si-PR-PDMS chip is bonded on the glass slide after an oxygen plasma treatment. 4) The assembly is dipped into acetone to dissolve the PR layer and remove the Si transfer chip. 5) A top gold electrode is sputtered on the PDMS through a shadow mask. 6) Implantation is conducted through a shadow mask. Electrical contacts are made to the sputtered electrodes*

contacts, that can have an influence on the measurement (Fig. 4.6): A PDMS layer is spin-coated on a PR-coated Si wafer and diced into 25×25 mm^2 chips. On a microscope glass slide, a patterned gold electrode is deposited by cathodic sputtering. The PDMS chip is bonded on the microscope slide by treatment of the two surfaces in a low-energy oxygen plasma. The assembly is then dipped into acetone to remove the Si transfer chip. A second patterned electrode is sputtered on the PDMS layer and a 5×5 mm^2 patterned implantated zone is defined to cover both electrodes. The implanted zone has one side on the top Au electrode, and the other side covering the bottom electrode, separated by the PDMS layer. This active zone is far from the electrical connections, where mechanical stress which deform the PDMS is applied. Consequently, deformation due to electrical contacts will have no impact on the maximal voltage that can be applied to the structure. Implantations were conducted at 5 keV for both Au and Pd samples. For Au, the implanted dose was $3.8 \cdot 10^{16}$ at/cm^2, and for Pd $4.2 \cdot 10^{16}$ at/cm^2. High doses were chosen on purpose to accentuate the implantation-induced degradation, if any.

4.6   Suspended membranes

Thin $(20 - 30 \ \mu$m) suspended PDMS membranes are a key geometry for many measurements, from mechanical characterization (Young's modulus and stress, cf. subsections 5.3.2–5.3.4), to diaphragm actuators (cf. chapter 6). Most of the standard MEMS fabrication processes for the fabrication of thin-film suspended membranes are based on deposition of the membrane material on a substrate, with a subsequent patterned backside etching of the substrate to define the openings and free the membranes. Although this kind of approach
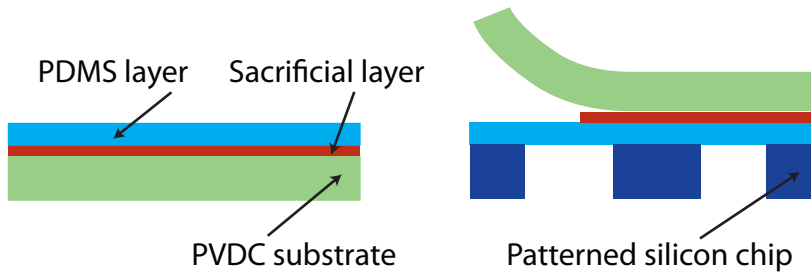
Figure 4.7: *Fabrication of suspended PDMS membranes. Spin-coating of a PR sacrificial layer on a flexible PVDC sheet stretched on a rigid frame, followed by the spin-coating and curing of the PDMS layer (left). Oxygen plasma bonding of the PDMS layer on a patterned Si wafer with through holes, and removal of the PVDC transfer substrate by dissolution of the PR layer.*

was successfully applied to PDMS membranes by other groups [19,73], we have selected a different process, mainly motivated by the clean room staff's desire to keep PDMS out of dry etching equipment.

Consequently, we have opted for a bonding-based process: The PDMS is spun on a transfer substrate preliminarily coated with a $2-3$ μm-thick photoresist (PR) layer which serves as a sacrificial layer. In parallel, through-holes ($\varnothing 1-3$ mm) are patterned in a Si wafer, either by deep reactive ion etching (DRIE), or by UV-laser drilling. The patterned wafer and the PDMS layer are irreversibly bonded together at room temperature after an oxygen plasma treatment. The surface activations for most of the chips used during this study were made in an old lunatic plasma asher whose operational parameters were not easily controlled, except for the generator's frequency: 13.56 MHz. The latter chips were bonded in a new microwave plasma reactor ($f = 2.45$ GHz) for 15 s at 400 W, and with an O_2 flow of 400 sccm at a pressure of ~ 500 mTorr, for very reliable and reproducible results.

Finally, the transfer wafer is removed by dissolution of the sacrificial layer (Fig. 4.7). The bonding and release processes were tested on the wafer- and chip-level. For the latter solution, the patterned Si wafer is diced into separate chips, which are then separately bonded on the PDMS layer. The chief advantage of the chip-level process resides in the possibility to bond the patterned Si chips to different PDMS layers (for example of different thicknesses), thus quickly obtaining suspended membranes with different properties.

The transfer substrate on which the PDMS is spin-coated is a stretched polyvinylidene chloride (PVDC) foil. It was necessary to use a flexible transfer support in order to ensure perfect bonding on the patterned Si wafer. Indeed, as the PDMS film is not homogeneous on the whole wafer's surface (with mainly a bump at the center, and at the substrate's periphery), a rigid transfer wafer leads to incomplete bonding, with most of the PDMS not even touching the target wafer (Fig 4.8). Exerting important mechanical pressure during the bonding is a possible solution, but the more elegant technique using a flexible transfer substrate was used. A gentle push with the finger is sufficient to ensure perfect bonding on the whole surface.

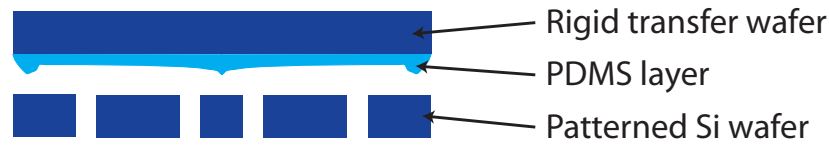For a chip-level process, the thickness homogeneity issue is reduced, and

Rigid transfer wafer
PDMS layer
Patterned Si wafer

Figure 4.8: *The (grossly exaggerated) PDMS thickness inhomogeneities prevent a good quality bonding over the whole surface if the transfer substrate is rigid.*

it is possible to successfully bond a PDMS layer that was prepared on a rigid substrate (such as a Si wafer diced into separate chips). However, the use of a flexible transfer substrate is still preferred, as it greatly facilitates the release process. Indeed, the PVDC substrate can be simply peeled off in an acetone bath which dissolves the sacrificial PR layer. With a rigid transfer substrate, the release process takes much more time, as acetone must diffuse from the border to the center to fully dissolve the PR layer before the two pieces can be separated. This issue was in fact encountered during the fabrication of the chips for dielectric strength measurement (cf. section 4.5). Using a flexible transfer substrate leads to better bonding quality and yield.

Compared to a standard thin-film membrane fabrication process, our bonding scheme gives us access to the backside of the PDMS membrane, which – before the bonding step takes place – is the exposed PDMS surface on the transfer wafer. This opportunity can be used, for example, to make the backside implantation before bonding the PDMS layer on the patterned chip or wafer (cf. subsection 4.7.3, in which this opportunity is used).

4.7 Diaphragm actuators

4.7.1 Silicon frame

Diaphragm actuators are fabricated as follows (Fig. 4.9): starting with a suspended membrane (cf. section 4.6), gold contacts are sputtered on the top side of the PDMS to serve as contact pads (cf. section 4.3). Then, topside implantation is conducted through a steel shadow mask whose openings include the suspended membranes and the gold pads. The backside of the membrane is implanted without any mask, and through the Si chip's holes. The Si chip serves as a ground plane, and electrical connections are added to it and to the gold pads that contact the top implantation. Wire bonding can unfortunately not be used to connect the Au pad to an external power supply. The PDMS below the gold pad absorbs the vibration energy, and the bonding wires cannot be attached to the pad. Two different techniques were used to attach a copper wire to the contact pad: with conductive double sided adhesive tape used in SEM or with a conducting elastomeric paste.

It should be noted that executing the patterned (top) implantation on released membranes only works in the case where a steel shadow mask is used, and would not be possible if the patterning was done with a photolithograpy step. Indeed, it is not possible to spin PR on released PDMS membranes: they would deform and cause an accumulation of PR. Consequently, if the implan-
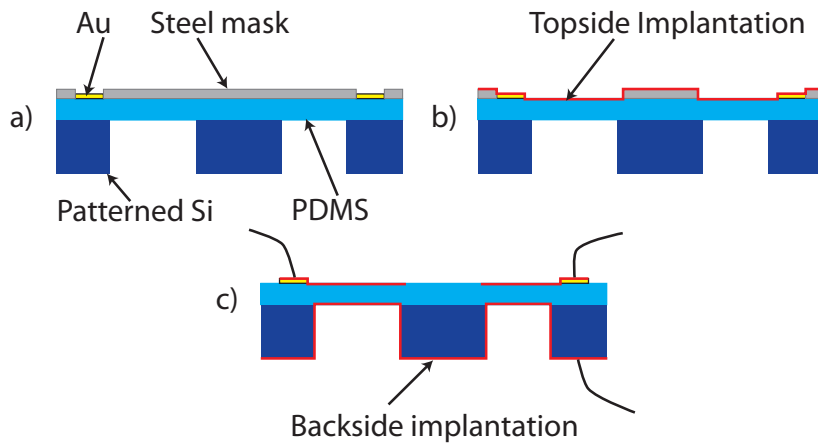
Figure 4.9: *Fabrication process of diaphragm actuators on a Si frame. a) Sputtering of Au contact pads through a steel shadow mask. b) Topside implantation through a steel shadow mask. c) Backside implantation through the holes and electrical connections.*
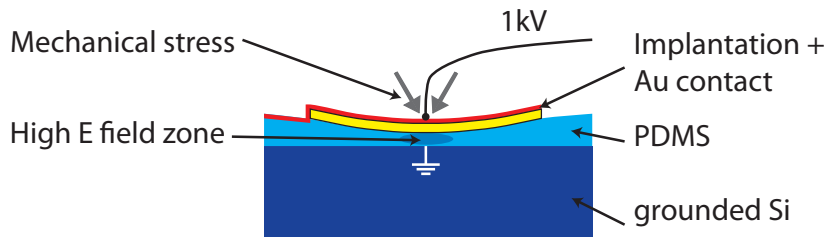

Figure 4.10: *Actuator on silicon: due to local deformation induced by mechanical stress, a high electric field zone is created at the electrical connection's anchor points, leading to lower possible voltages before dielectric breakdown of the PDMS.*

tation pattern requires a higher resolution than what can be achieved with a steel shadow mask and photolithography must be used, a modified process should be considered, in which the release of the membranes represents the last step, similar to a standard suspended membrane fabrication process (cf. section 4.6).

4.7.2 Pyrex frame

The main flaw of the diaphragm actuator on silicon is the fact that the frame itself is conducting and serves as the ground plane. When the electrical wires are added to the top contacts on the PDMS, mechanical force is applied, which leads to the deformation of the PDMS layer, and the creation of a high electric field zone upon high voltage application (Fig. 4.10). This high E field zone limits the voltage that can be applied to the PDMS membrane before dielectric breakdown of the material, thus affecting the displacement properties (cf. subsection 6.2.3) and the reliability of the actuator.
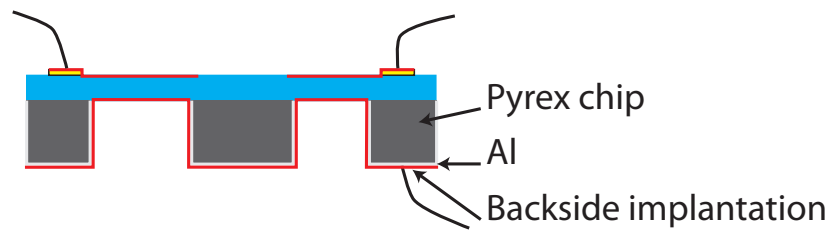
Figure 4.11: *Actuator on Pyrex: Al metallization on the backside and on the holes' walls serves as the ground plane. Topside electrical connection wires are not applied to a high electric field zone; only the active area of the PDMS is submitted to high electric field.*
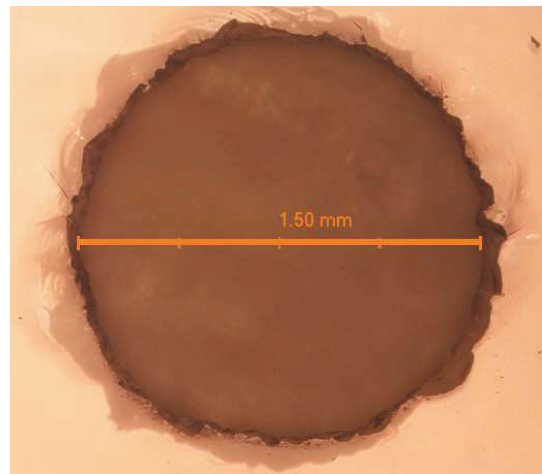

Figure 4.12: *Picture of a ∅1.5 mm hole drilled by laser into a 500 μm-thick Pyrex wafer. Laser-induced damages produce a hole that is not perfectly circular, which influences the deformed membrane's shape.*

Consequently an improved version of the actuators was fabricated, by replacing silicon by Pyrex: holes were drilled by an UV laser through a $500-\mu$m-thick Pyrex wafer. One face of the patterned wafer, as well as the holes' walls, was metalized by 300 nm of Al in an e-beam evaporator. A planetary substrate holder was used to ensure step coverage. The PDMS was bonded on the non-metalized side of the Pyrex, and implantation was conducted similarly to what was done for Si chips (Fig. 4.11). But in this configuration, the electrical wires are not applied in a zone of high electric field. Consequently, even if thinning of the PDMS layer – caused by mechanical force applied to attach the wires – occurs at this location, this will not lower the maximal voltage which can be applied to the device.

Drilling through-holes by laser into Pyrex is a very fast prototyping method, as it requires no mask and photolithography step, but the resulting holes' shape is far from being perfectly circular due to shattered borders (Figure 4.12). This has an influence on the deformed membranes' shape (for example when inflated with air, or activated by application of a voltage), and these Pyrex chips were

not used for bulge test measurements, whose accuracy depends on the shape the membrane takes while defroming. Future devices might need a sharper definition of the holes' borders, with a drilling by sandbalsting [74], or by wet BHF etching which requires a few additional fabrication steps.

This configuration on Pyrex allowed to geatly increase the maximal electric field that could be applied to the PDMS membrane, from < 60 V/μm for actuators on Si chips, to > 100 V/μm on Pyrex, which corresponds to the breakdown field we measured on our thin PDMS membranes (cf. section 5.4). Although actuators on Pyrex were capable of very large displacements due to this increase in the range of applicable voltage (cf. chapter 6), they moved very slowly, with raise and fall times in the order of seconds. This was attributed to a very poor electrical contact between the backside implantation, and the metallization of the holes' sidewalls. Actuators made on silicon chips also exhibited high time constants with a large distribution between $50 - 500$ ms, also attributed to an inconsistant electrical contact between the back of the implanted membrane and the Si chip. The next section describes the final design which combines the advantage of the Pyrex chip – to apply large voltages – with a good backside electrical contact for high motion speeds.

4.7.3 Final design

Reliable and good-quality electrical contact to the backside implantation can only be achieved if the backside implantation is executed before bonding the PDMS to the substrate, and connected to the border of the chip by a metal electrode. Hence, a new process flow was developped, that takes advantage of the exposed PDMS backside before the bonding step (cf. section 4.6) in order to implant the back electrode before bonding (Fig. 4.13).

First, a PDMS layer is spun on a PR-coated silicon wafer and cured at room temperature. The wafer is then diced into 18×18 mm^2 chips. A patterned gold electrode which extends up to the chip's border is sputtered on the silicon chip, followed by the backside implantation. In parallel, through holes ($\varnothing 1.5$, 2, and 3 mm) are drilled with an UV laser into a pyrex wafer, which is then diced into 20×20 mm^2 chips. A gold electrode, identical to the one made on the PDMS and which extends to the chip's border is sputtered on the Pyrex chip. Oxygen plasma treatment is used to bond the two chips together. The two gold electrodes on the PDMS and Pyrex are aligned and put into contact during the bonding. The alignment is assured by a a x, y, z, θ stage, which is used to position the two chips relative to each other. The operation is followed by the removal of the silicon chip by dissolution of the PR layer in acetone, which leaves the PDMS membrane bonded on the Pyrex chip. Because the Pyrex chip is 2 mm larger than the PDMS membrane, the gold electrode provides an electrical contact to the bottom implantation. Topside gold contacts and implantations are finally carried out similarly to what was done for the actuators on silicon.

A variant of this process flow consists in using PDMS on a flexible PVDC substrate rather than on silicon, in order to ease the bonding and release procedures (cf. section 4.6). In that case, a piece of PDMS on PVDC is fixed to the frame part of the steel masks (cf. Fig. 4.3) and replaces the PDMS-coated Si chip. Two small holes are punched at the border of the suspended PVDC/PDMS sandwich to allow access to the patterned gold electrode on the Pyrex after the bonding, because when using PDMS on a flexible substrate,
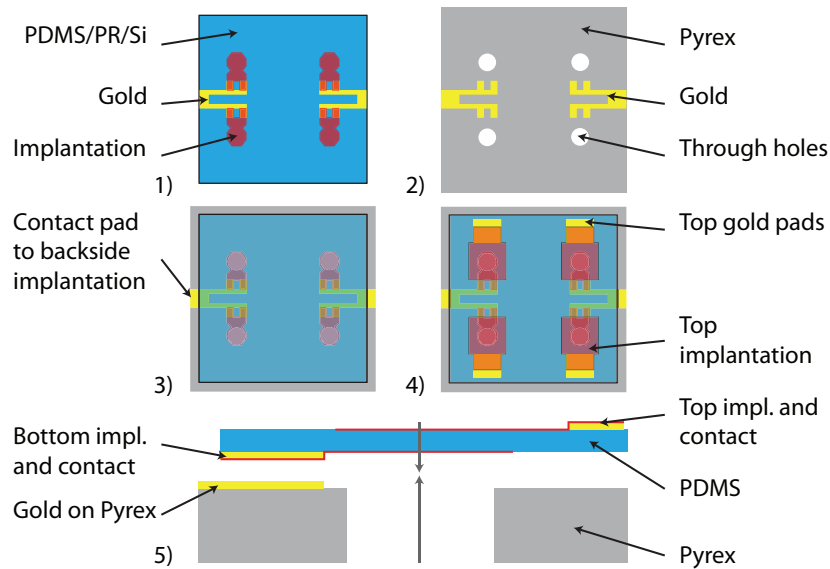
Figure 4.13: *Final design with good quality backside electrical contacts. 1) PDMS is spun on Si wafer covered with PR, which is then diced into 18×18 mm^2 chips. Gold contacts are sputtered on the PDMS, followed by the backside patterned implantation. 2) Holes are patterned with an UV laser through a Pyrex wafer, which is then diced into 20×20 mm^2. Gold contacts are sputtered on the Pyrex chip. The gold contacts on the PDMS and on the Pyrex chip have the same shape. 3) The Si/PR/PDMS sandwich is bonded on the pyrex chip. The two gold electrodes are aligned and put in contact during the bonding. The Si chip is removed by dissolution of the PR layer in acetone. 4) Topside gold contacts and implantation are added. 5) Exploded vue of an actuator's crossection.*

one looses the advantage of having a PDMS layer slightly smaller than the Pyrex chip, providing direct access to the gold contacts on Pyrex.

This process flow allowed the fabriation of actuators that combined high actuation voltages with good electrical contact to the backside implantation, leading to high response speeds. However, it introduced new issues that have yet to be solved. Because the backside implantation is made before bonding the PDMS layer on the Pyrex chip, the implanted zone which links the suspended membrane with the gold sputtered electrode is in contact with the Pyrex chip. Because the penetration depth of the metallic particles extends up to the surface of the PDMS (cf. section 3.4), the interface in this region is Pyrex/gold and not Pyrex/PDMS. During the bonding step, O–H groups are formed on the surface of Pyrex and PDMS, which lead to a chemical bonding of the two surfaces when they are put in contact by the formation of O–H–O bridges at the interface. This process doesn't work with an Au interface, and the implanted zone (as well as the gold sputtered electrodes) remains not bonded. This forms a small non-bonded channel between the membrane and the chip's borders. If this has no consequences for unloaded tests, during which the vertical displacement is observed versus applied voltage, these chips can not be used

for characterization of the displacement under a distributed force (cf. section 6.4) or for bulge test measurements (cf. subsection 5.3.2). Indeed, both of the measurements require the application of a pressure on the backside of the membrane, and because of the existence of the non-bonded channel, the air can escape and a constant pressure cannot be maintained. A possible solution that will be tested is selective inkjet printing of PDMS on the backside implanted zones which are in contact with the Pyrex, in order to cover the gold by a very thin PDMS layer. Additionally, the laser drilling of the holes in the Pyrex chip probably creates microcracks in the chip, where stress concentrates, as the chips break very easily when fixed on the air-tight socket used for bulge test measurements.

Chapter 5

Electrical and mechanical properties of ion-implanted electrodes

This chapter reports on the basic properties of electrodes fabricated by metal ion implantation (cf. chapter 3) and their ability to be used as electrodes for dielectric elastomer actuators. The two main criteria that they must fulfill are time-stable electrical resistance and compliance. The latter requirement can be divided in two aspects: 1) low impact on the mechanical stiffness of the material on which the electrodes are created and 2) large deformation capabilities before loosing electrical conduction. In addition to these basic parameters, this chapter will present other aspects of implanted electrodes characterization, such as the impact of ion implantation on the dielectric breakdown field of the polymer, and transmission properties of implanted PDMS membranes.

5.1 Resistance and time stability

The first step to test the applicability of FCVA ion implantation to create compliant electrodes for DEAs (cf. section 3.4) consists in measuring the surface resistance[1] of implanted PDMS, as well as its stability in time, in order to show this technique's ability to create stable conductive layers.

Chips for resistance measurements were prepared and implanted with different metals and at different doses, starting at $9 \cdot 10^{15}$ at/cm^2 (cf. section 4.3). The surface resistance of each sample was measured with a multimeter immediately after the implantation. Additionally, the resistance was regularly monitored to record the time evolution of the implanted layers' electrical properties.

Transmission electron microscopy images of implanted PDMS show that when the metallic ions penetrate the polymer's surface, they tend to form clusters whose size depends on the dose [62]. At low doses ($< 10^{16}$ at/cm^2 for Au) the implanted particles' density is low and they are too far apart from each other to create a conductive path. Consequently, resistance remains very high (above measurable range). For higher doses, a sharp decrease in resistivity is observed, which also coincides with a rapid increase of the stiffness of the

---

[1]if not specified otherwise, *resistance* refers to *electrical resistance* in this document
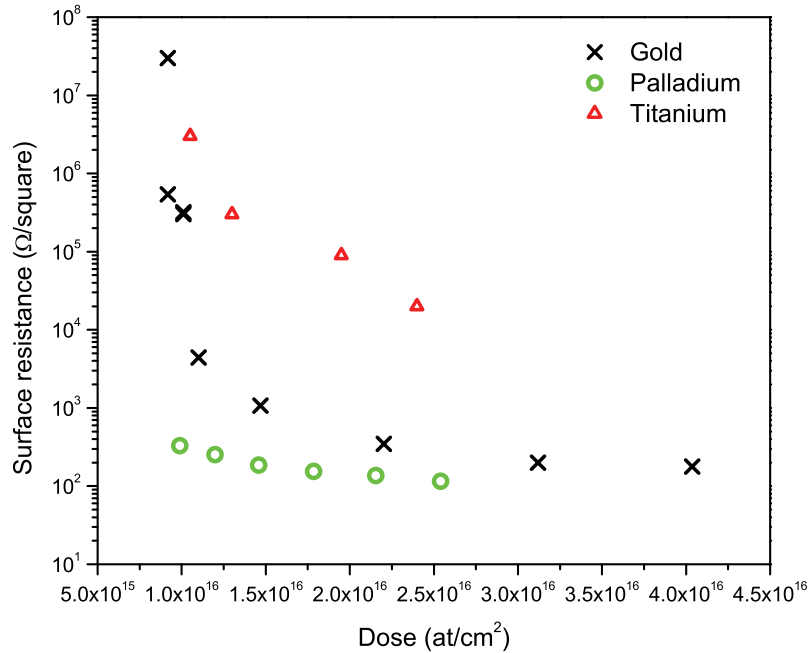
Figure 5.1: *Surface resistance versus dose obtained for Au, Pd, and Ti implantations at 5 keV. The percolation limit is clearly visible for gold.*

membrane (cf. subsection 5.3.4). This is the percolation threshold: the density of metallic particles becomes high enough that conduction paths appear in the implanted layer. For Au, the percolation region is particularly narrow: the surface resistivity drops from $> 10^9$ Ω/square to 1 kΩ/square for doses between 10^{16} at/cm^2 and $1.5 \cdot 10^{16}$ at/cm^2 (Fig 5.1). For titanium, the percolation begins for the same dose, but is much less sharp, and the surface resistance at higher doses is larger than for gold. Palladium has a percolation threshold below $1 \cdot 10^{16}$ at/cm^2, which is therefore not visible on this set of samples. The percolation region of Pd-implanted layers occurring at low doses, combined with the high ion flux obtained with Pd on our FCVA system (Fig. 3.7) makes it difficult to obtain layers in the percolation zone. Pd-implanted layers already have an interesting surface resistance for doses around $1 \cdot 10^{16}$ at/cm^2, and obtaining a low surface resistance with less metallic particles has a very positive influence on the conduction/stiffening tradeoff that will be described in details later (cf. subsection 5.3.4).

The saturation of the surface resistance observed at high doses (clearly visible for gold) can be explained by two different factors. Sputtering of the implanted material has been observed by Niklaus for standard beamline Au ion implantation for doses higher than $2.5 \cdot 10^{16}$ at/cm^2, leading to an implanted dose smaller than expected[2]. It is possible that the same phenomenon occurs with FCVA implantation, although this has not yet been investigated. Additionally, the chips used for resistance measurements will only give accurate
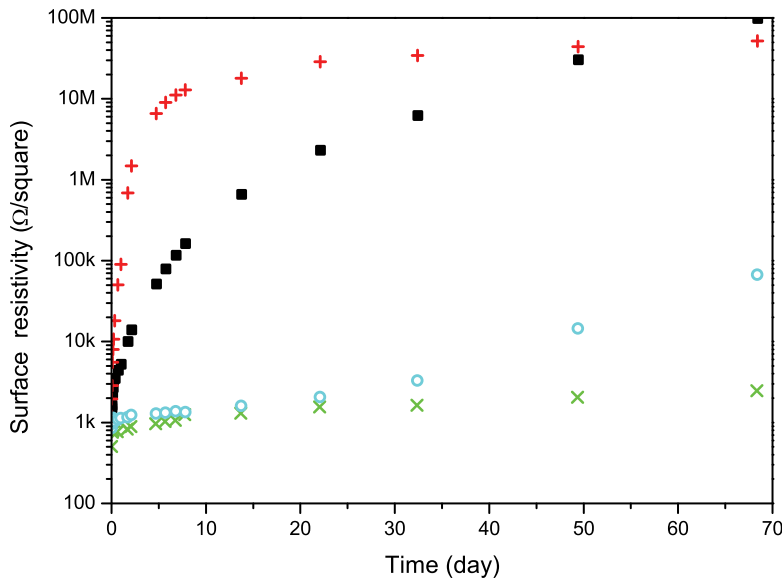
---

[2]Not yet published

Figure 5.2: *Time stability of the surface resistivity of Ti-implanted PDMS at different high dose values (> 3 · 10^{16} at/cm^2). Even layers with an initial surface resistivity < 2 kΩ/square show an important drift with time.*

results when the resistance of the implanted zone is much higher than that of the gold contact pads. When the implanted layer becomes well conductive, the contacts' resistance will have a non-negligible influence on the measured resistance. A new set of masks is currently being made with a larger spacing between the two Au contacts, in order to decrease the influence of the well-conductive sputtered zone in the final results.

Time stability of the resistivity is a concern for titanium layers, which suffer from oxidation: their resistivity quickly increases if left in ambient air, unless they are heavily implanted. But even for doses above $3 \cdot 10^{16}$ at/cm^2 (the precise dose is not given due the probable invalidity of our RBS calibration for high doses), which produces layers with a surface resistance of ~ 2 kΩ/square, the resistance increases with time (Figure 5.2). For the highest tested dose on the figure, one obtains an initial surface resistance around 500 Ω/square that stabilizes around 2 kΩ/square after 50 days. If the layers are kept under vacuum, the conductivity's degradation can be stopped. On the other hand, gold-implanted layers exhibit very stable resistivities vs. time for doses higher than $1.2 \cdot 10^{16}$ at/cm^2. Below this limit, the resistivity increases with time, probably due to diffusion (Fig. 5.3). The same behavior is observed for Pd implantations (Fig. 5.4); for both metals, implanted layers with an initial resistivity below 10 kΩ/square exhibit an excellent time stability over more than eight months. As Ti layers have higher resistances compared to the two noble metals, coupled with oxidation and degradation problems, titanium implantations were abandoned. Preliminary tests and implantations were made with this metal for availability reasons, but due to stability issues, we then
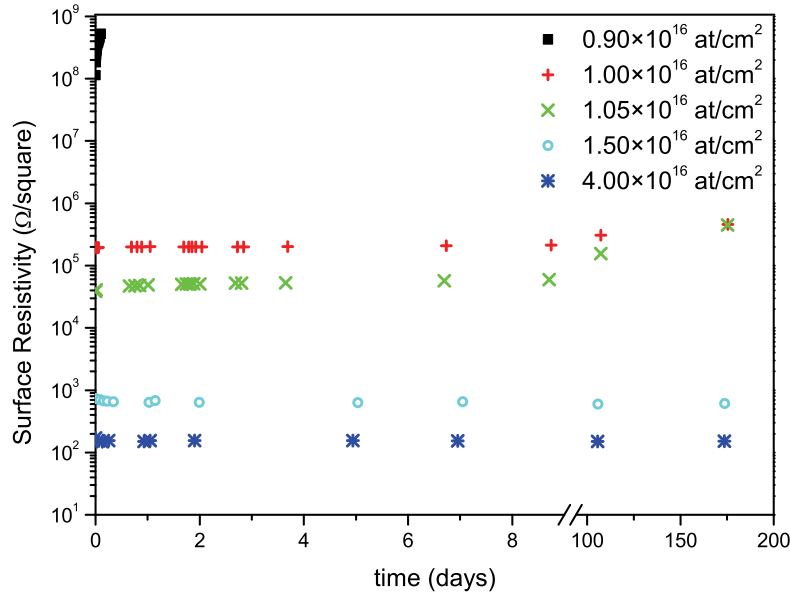
Figure 5.3: *Time stability of the surface resistivity of Au-implanted PDMS for different metal doses over a time period of 180 days. Above a critical ion dose, the surface resistance is highly stable and has not been observed to evolve on a period of 180 days.*

concentrated on gold and palladium implantations.

5.2   Maximum strain capabilities

Having shown in the previous section that ion implantation allows to create conductive layers that are stable in time, the strain capabilities of these electrodes were then investigated. 1) How does the resistance change when the implanted layer is deformed, 2) what is the maximal achievable strain at which the layer ceases to be conductive, and 3) is there a degradation of the resistance for cyclic deformation, are three questions addressed in this section. To conduct the tests presented in this chapter, uniaxial tensile strain was applied on implanted PDMS strips (see section 4.4 for the geometry and fabrication of the strips) using a linear stage connected to a stepper motor.

5.2.1   Overview of the influence of gold dose

The influence of dose was studied by implanting PDMS strips with different doses of gold ions at 5 keV, and stretching them while recording their resistance. Sputtered samples were also fabricated to compare metal ion implantation's elongation capabilities with those of conventional metallic electrodes. Sputtering was conducted in a Balzers SCD-030 bench top sputtering system for 3' at 60 mA, for a thickness of about 25 nm). The maximal strain before loss of conductivity (s_{max}) was seen to be very dependent on the dose and deposition method (Figure 5.5). R_0 is the resistance of the undeformed strip,
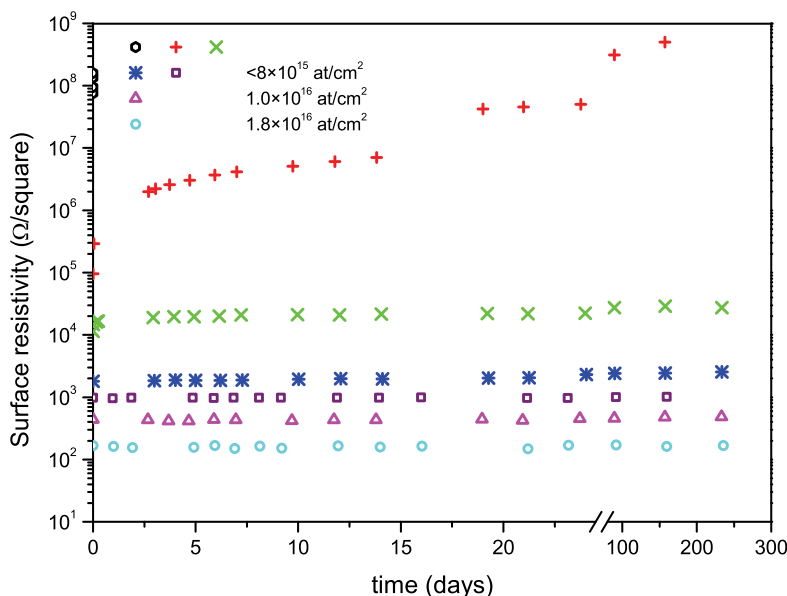
Figure 5.4: *Time stability of the surface resistivity of Pd-implanted PDMS for different metal doses over a time period of 280 days. If the initial sheet resistance is below 10^4 Ω/square, it exhibits an excellent time stability.*

which varies from 17 Ω for the sputtered sample to 398 Ω for the lowest-dose sample.

Unsurprisingly, the sputtered sample exhibited the smallest strain range before loss of conductivity, which was limited to 3%. At 1% strain, cracks start to appear perpendicularly to the direction of traction, and at 3% strain, the cracks become wide enough to completely interrupt the conducting path. In the case of implantation, one may think that the higher the implanted dose, the higher the number of clusters, and consequently the higher the maximum extension before observing a loss of conductivity. However, the opposite trend is observed: The highly implanted samples can be stretched much less than the lightly implanted ones. The maximal strain s_{max} is increased from 30% for an implantation dose of 800 pulses/cm^2 to 175% for a dose which is two times lower.

TEM images of membranes' crossections implanted at 5 keV show that the clusters' size increases with the dose [62], suggesting that a highly implanted gold layer exhibits characteristics that will tend toward those of a continuous metallic film. The dose must be controlled to obtain simultaneously very high maximum strain ($> 50\%$), and a time stable conductivity. The dose must be high enough to obtain a stable layer, and it must remain low enough to enable large strain capabilities. The strip implanted with 400 pulses/cm^2 combines a low initial resistance of 398 Ω, (199 Ω/square) while exhibiting an outstanding maximal strain before loss of conductivity of 175%, at which point the strip's resistance is 1.1 MΩ.

As seen in figure 5.5, the higher the implanted dose, the higher the resistance increase rate versus strain. However, this is not the only factor that reduces
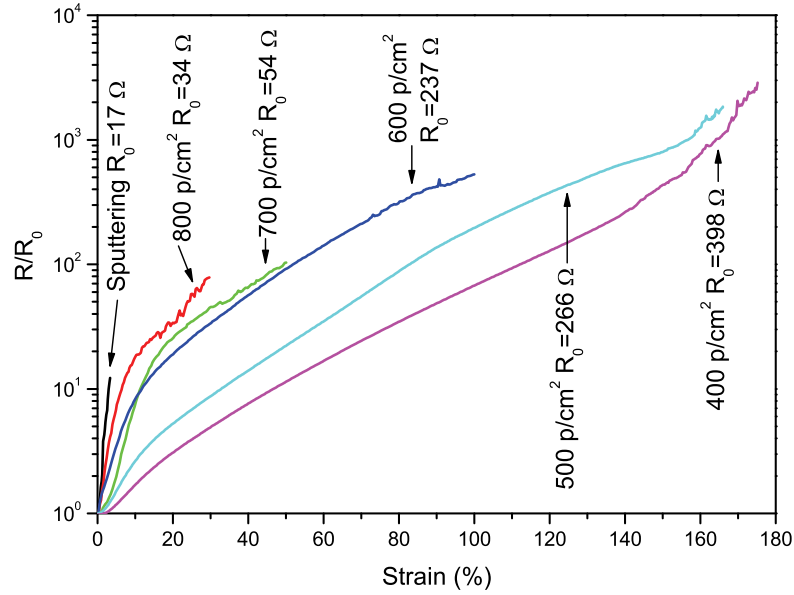
Figure 5.5: *Change in resistance (R/R_0, where R_0 is the undeformed resistance) of gold-sputtered and gold-implanted PDMS strips under uniaxial stress up to loss of conductivity. The implanted dose are given in pulses per square centimeter, due to the difficulty of giving a reliable dose value when motorized scanning is used for the implantation. The maximum strain is 3% for sputtered films and 175% for implanted films.*

the maximal strain of the higher implanted samples. The maximal resistance of the strip, reached just before the layer becomes non-conductive, is much lower on the high-dose samples. From 210 Ω for the continuous sputtered film, it increases to 2.6 kΩ for the implantion at 800 pulses/cm^2, and up to 1.1 MΩ for the lowest tested dose. In the case of the sputtered layer, the limited increase in resistance before a brutal loss of conductivity is explained by the cracks in the electrode: the film suddenly becomes non-conductive when the cracks grow large enough to break the conduction path. The situation is quite similar for the implanted samples: the high-dose electrodes have large clusters and a good conductivity, but when the clusters are separated and cease to touch each other, the conducting path is broken, even though the conductivity just before the path's interruption was still high. For the lower-dose samples that have many small clusters, the strain can be increased much more before all the conductive paths are broken, but as more and more paths break, the resistance increases to much higher values.

5.2.2   Overview of the influence of palladium dose

Similar tests were conducted with Pd-implantations, with which stable low-resistance layers were also produced. A relation between dose and maximal strain was observed, similar to gold implantations, however the maximal achiev-
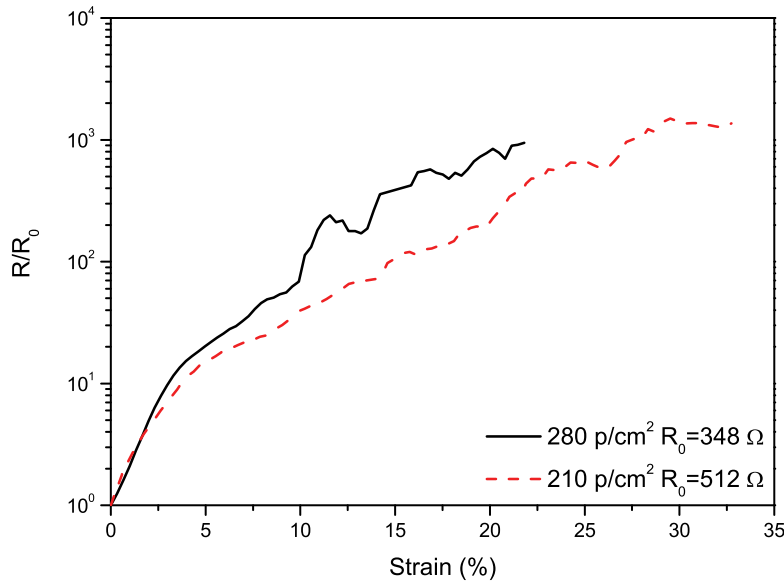
Figure 5.6: *Change in resistance (R/R_0) of Pd-implanted PDMS strips submitted to uniaxial stress up to loss of conductivity. Even for the low doses used (280 and 210 pulses/cm^2, $R_0 = 348$ Ω and $R_0 = 511$ Ω) the maximal strain is low.*

able strain is considerably reduced compared to Au. Even for low doses, the maximal achievable strain was 33% (Figure 5.6). Additionally, the resistance value is noisy for strains above 10%. TEM micrographs of Pd-implanted PDMS crossections have shown a microstructure whose clusters are much bigger than in the case of gold implantation[3]. Because the microstructure of the implanted layer depends on the implanted element, the mechanical and electrical properties of the imlplanted electrodes depend on the metal used. With its larger clusters, palladium-implanted electrodes exhibit smaller strain capabilities than gold-implanted electrodes.

5.2.3 Influence of the number of cycles and strain on the resistance

For the remaining of this section, the resistance versus strain study was conducted on Au-implanted strips with a dose of 500 pulses/cm^2, which combine a low resistance with large strain capabilities. Stepped strain tests were performed on a strip to observe the stability of the resistance when the sample is kept at constant strain for a few minutes. The strain was increased from 0 to 150% by steps of 10% and held for 10 minutes at each strain level (Figure 5.7). The resistance remains very stable with time, even at large strain levels, which is an important difference compared to what O'Brien observed on carbon-coated strips whose resistance exhibited noise as well as bumps [14].

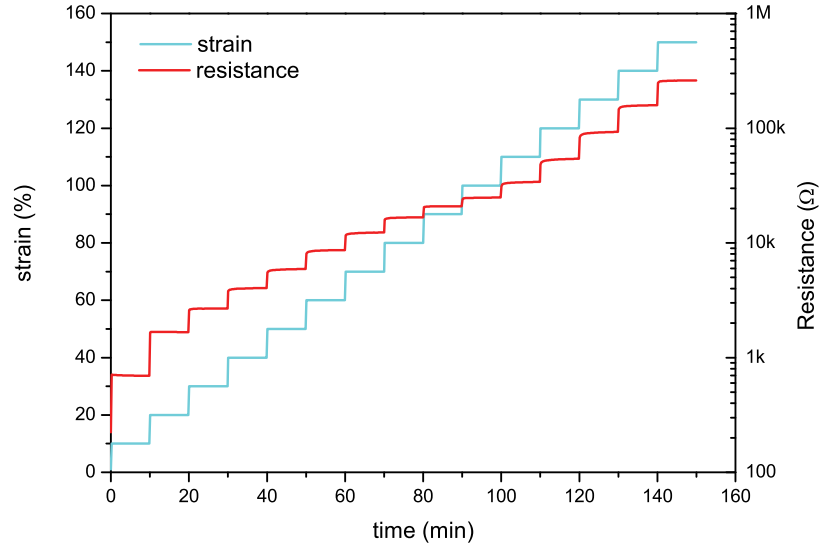[3]Work of M. Niklaus, not yet published.

Figure 5.7: *Resistance of an Au-implanted strip with* 500 *pulses/cm^2 for different strains increased by 10% steps every 10 minutes, up to 150% strain. Resistance does not drift during the hold time.*
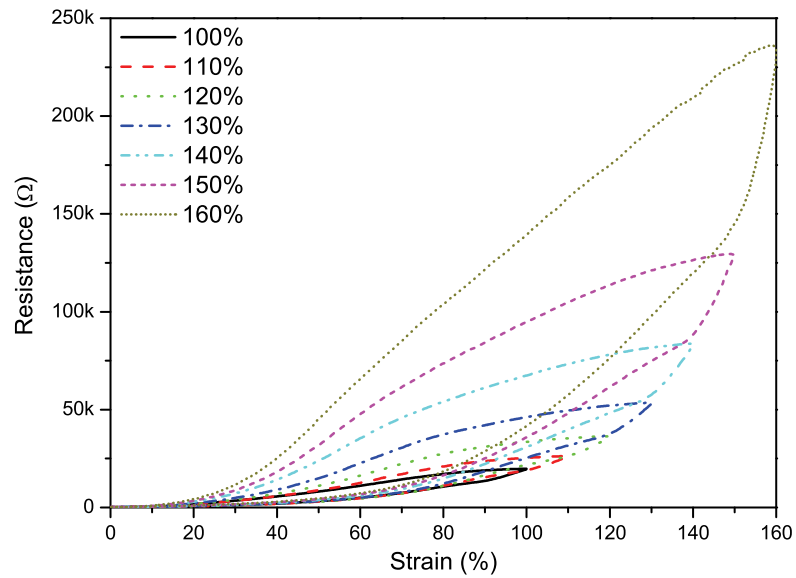

Figure 5.8: *Resistance versus strain for cycles up to different maximal strains on a low-dose,* 500 *pulses/cm^2 Au-implanted strip. As can be seen, an important hysteresis is observed for strain cycles on low-dose samples.*
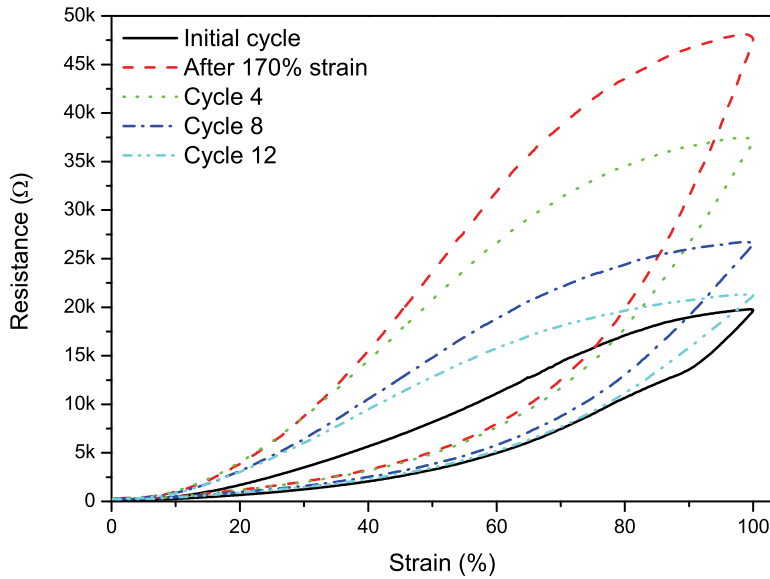
Figure 5.9: *Resistance versus strain for different cycles from 0 to 100% and back to 0. The black curve represents the first cycle. Then the strip was stretched up to 170% strain (not shown). The dashed curve represent a second cycle to 100% made after the larger strain. This cycle was followed by 11 other identical cycles to 100%.*

Low-dose samples can sustain large strains while remaining conductive, but this comes at the cost of a very large hysteresis for a complete cycle, during which the strain is increased from 0 to s_{max}, and then decreased back to 0. Cycles were conducted at a slow speed (0.01 mm/s) for s_{max} between 10% and 160%. The data for the cycles from $0 - 100\%$ to $0 - 160\%$ are plotted in figure 5.8. The cycles characteristics exhibit a very large hysteresis whose amplitude increases with increasing maximal strain. For the loop up to 160% strain, the resistance difference for an identical strain is as high as 100 kΩ in the broadest portion of the hysteresis. This phenomenon is not observed on highly implanted samples: it was quasi nonexistant on the 800 pulses/cm^2 and the 700 pulses/cm^2 strips, as well on the sputtered ones.

If repeatedly stretched to the same maximal strain, the obtained resistance is very reproducible between the cycles. However, if a strip is stretched from 0 to s_1 and back to 0, followed by another deformation up to $s_2 > s_1$, and followed by a third cycle up to s_1 again, the two cycles $0 - s_1 - 0$ will have a drastically different resistance versus strain behavior. The figure 5.9 illustrates this phenomenon. A strip was extended to 100% and back (plain curve). Then it was stretched up to 170% and back (not shown on the graph). This large extension was followed by 12 cycles up to 100%. The first cycle after the large 170% strain is radically different from the initial cycle: the resistance at the end of the cycle is 2.4 times higher, and the hysteresis is much larger. With subsequent cycles at 100% (cycle 4, 8 and 12 are shown on the graph), the
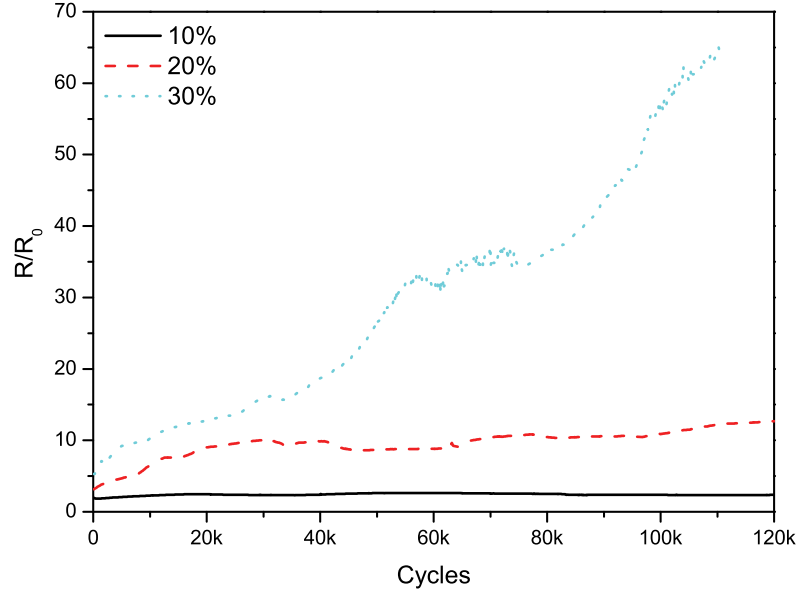
Figure 5.10: *Degradation of the resistance of a* 500 *pulses/cm^2 Au-implanted strip cyclically stretched to 10%, 20%, and 30% for 100k+ cycles.*

Table 5.1: *Parameters and measured values for the ageing test on a* 500 *pulses/cm^2 Au-implanted strip. R_0 is the initial unstretched resistance; $R_{max,0}$ and $R_{max,f}$ are respectively the resistance at maximal strain at the beginning of the test and at the end.*

s_{max}	R_0 (Ω)	$R_{max,0}/R_0$	cycles	$R_{max,f}/R_0$
10%	354	1.96	165k	2.60
20%	391	3.15	123k	12.9
30%	1205	5.24	111k	61.4

resistance at the maximal strain is gradually reduced to reach a value 8.2% higher than the original one, and the hysteresis' amplitude is also reduced, but remains more important than originally. Additional strain cycles did not further reduce the maximal resistance or the hysteresis, and were consequently similar to cycle number 12.

Ageing and degradation of the resistance was studied for cyclic stretching between 0 and $\hat{s}$ on a 500 pulses/cm^2 Au-implanted sample. The tested strip was cyclically stretched up to $\hat{s}$ and the resistance measured every 100 cycles. More than 100k cycles were made for $\hat{s}$ strain values of 10%, 20%, and 30%, and the resistance at peak strain divided by the initial zero strain resistance is plotted in figure 5.10, where R is the resistance of the stretched strip, and R_0 is the initial unstretched resistance. The resistance at the maximal strain increases with the number of cycles, and the increase rate depends on the strain
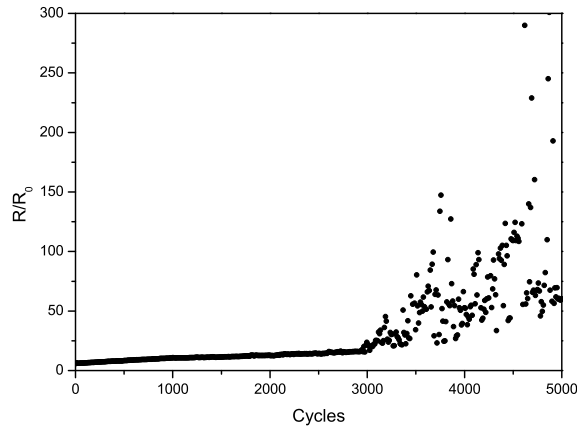
Figure 5.11: *Degradation of the resistance of a* 800 *pulses/cm^2 Au-implanted strip cyclically stretched to 20% strain. After 3000 cycles, the implanted layer is damaged, and the recorded resistance becomes unstable.*

level. For 10% strain, a small degradation is observed: the stretched strip's resistance exhibits only an increase of 32% over 165k cycles. Furthermore, the increase occurs during the first 10k cycles, and the resistance remains stable afterwards. For the 20% strain, the degradation is more important, and an increase of 310% of the stretched value is observed over 123k cycles. The degradation rate is higher for the first 30k cycles, but a positive degradation rate is observed throughout the test. Finally, the test at 30% shows a more important degradation with a stretched resistance's increase of a factor 12, and a degradation rate which increases with the number of cycles. Table 5.1 summarizes the parameters and results of this test.

The degradation for three different strains presented in the previous paragraph were conducted on the same implanted strip, which therefore survived 399k cycles while remaining conductive. Even though the strip's resistance underwent large increase, it is still electrically usable for DEA applications, which do not require a very low resistance, as the response speed of actuators is generally mechanically- rather than electrically-limited (cf. section 6.5). Similarly to what was observed for the maximal achievable strain, the degradation rate of a cyclically-stretched strip's resistance depends on the implanted metal dose. For highly implanted strips, the question is not about the increase of the resistance after a large number of cycles, but rather the number of cycles up to electrical failure of the layer. An example is given on figure 5.11 for a 800 pulses/cm^2 Au-implanted strip cyclically stretched to 20% strain. After 3000 cycles, the resistance ceases to increase regularly, and exhibit a noisy chaotic resistance due to irreversible damage to the microstructure. This is a drastically different behavior compared to the more lightly implanted samples, but part of the difference comes from the fact that a 20% strain represents 2/3 of the maximal strain for the high-dose strip, when it is only 12% of the low-dose strip's maximal strain.

It is difficult to compare the degradation of implanted electrodes with the other compliant electrodes' fabrication techniques (cf. subsection 3.4.1), be-
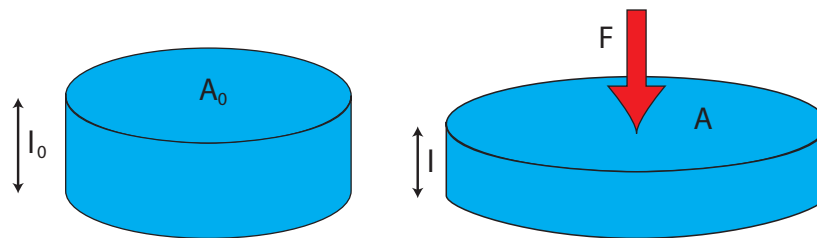
Figure 5.12: *Uniaxial compression tests were conducted on a cylinder of cross section A_0 and length l_0, which was placed on a lubricated plate. A moving lubricated upper plate applies a force F and deforms the cylinder.*

cause there is a crucial lack of literature on the reliability of these relatively new electrode developments. Among the few authors providing reliability data, Urdaneta and coworkers have conducted similar cyclic stretching tests on their Pt-salt electrodes and have observed a much higher degradation rate of the resistance for their electrodes [71]. For a similar cyclic test at 30%, they report an initial R/R_0 of 10, which is approximately 2 times more than for our Au-implanted layers, thus showing that the resistance increase versus strain is more important for the Pt-salt electrodes. The electrode cyclically strained at 30% fails after 1000 cycles, at which point the final R/R_0 is 800. This is 13 times more than what we get with our ion implanted electrodes after 100 time more cycles.

5.3   Mechanical properties

Precise determination of the mechanical (as well as geometrical) properties of the PDMS membranes is necessary to obtain good predictions of our actuators' behavior (displacement, mechanical work, etc.) by analytical models (cf. chapter 6). One of the most important parameters that determine a material's change of shape due to mechanical stress is the Young's modulus (cf. 2.3). Measuring the Young's modulus of non-implanted and implanted membranes not only allows to characterize our actuators' behavior, but also to quantify the stiffening impact of ion implantation on the elastomer's properties.

5.3.1   Compression tests

A first approach to determine the Young's modulus of the unimplanted PDMS was done by uniaxial compression tests. Compression was chosen rather than tension to get closer to the DEA actuation principle, i.e. compressive electrostatic force. Macroscale samples were fabricated in the form of cylinders $\varnothing 22$ mm $\times$ 14 mm. The tested cylinder was placed on a well-lubricated plate to ensure uniaxial stress when submitted to compression by the moving upper lubricated plate of a *Schenck* tension/compression machine (Fig. 5.12). From the measurement of the applied force and displacement, stress and strain (or stretch ratio) can be calculated.

The vertical stretch ratio, λ_z, defined as
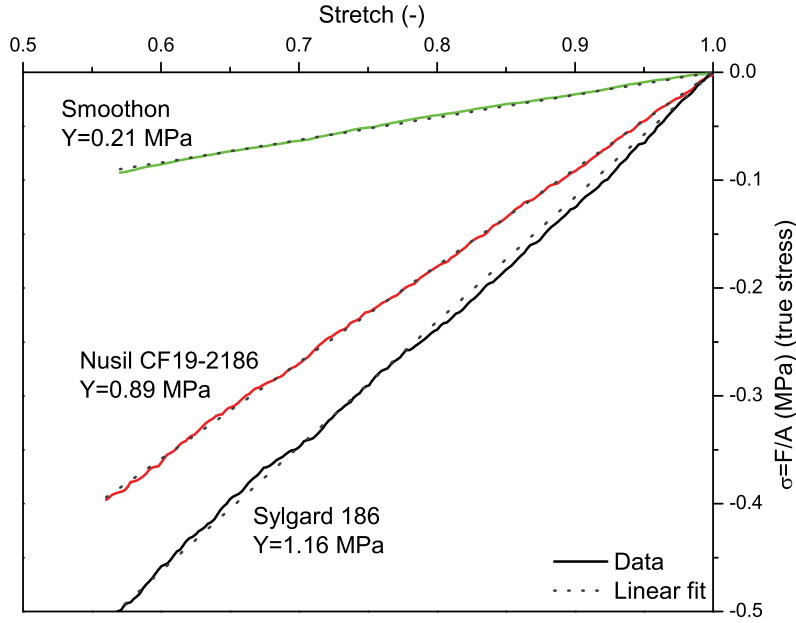
$$\lambda_z = 1 + s_z, \tag{5.1}$$

Figure 5.13: *True stress vs. vertical stretch ratio for three different PDMS: SmoothOn Dragon Skin, Sylgard 186, and Nusil CF19-2186. The slope of a line represents the Young's modulus of the PDMS.*

where s_z is the thickness strain, was varied between 1 and 0.6 during the compression tests. Due to the constant volume property of elastomers (Eq. 2.9), the important vertical compression ratio causes an equally important area stretch. The constant volume propertie (Eq. 2.9) can be rewritten as a function of the stretch ratios on the three principal axes:

$$\lambda_x \lambda_y \lambda_z = 1, \tag{5.2}$$

where $\lambda_{x,y,z}$ is the stretch ratio on the corresponding axis. As in the case of free boundary DEA actuation (cf. section 2.3), the two in-plane stretches are equal for uniaxial compression, leading to:

$$\lambda_x = \lambda_y = \sqrt{\lambda_a}, \tag{5.3}$$

where λ_a is the area stretch ratio. By combining equations 5.2 and 5.3, it can be seen that the area stretch ratio is inversely proportional to the vertical stretch ratio. The area stretch can therefore not be neglected while calculating the stress due to the large deformation involved.

When tension or compression tests are conducted with small strains ($< 5\%$), it is common to calculate the *engineering stress* σ_e out of the applied force F with:

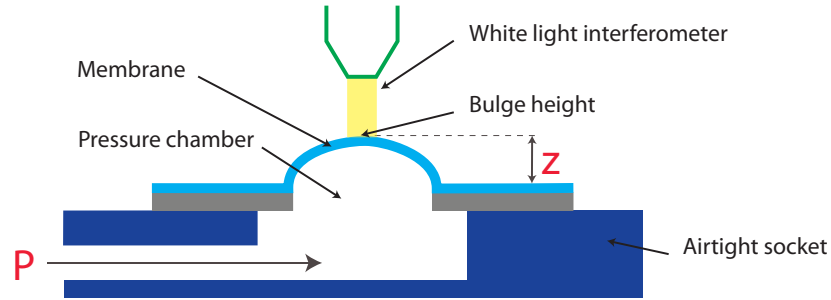$$\sigma_e = \frac{F}{A_0}, \tag{5.4}$$

Figure 5.14: *Schematic representation of a bulge test setup: A freestanding membrane is placed on an airtight socket and submitted to pressure on one of its sides. The deflection of the center of the membrane z is recorded for every value of the applied pressure p.*

where A_0 is the initial area of the sample. However, for larger strains, the change in area cannot be neglected, and the *true stress* σ needs to be calculated:

$$\sigma = \frac{F}{A} = \frac{F}{A_0 \lambda_a} = \frac{F \lambda_z}{A_0}. \tag{5.5}$$

Force and vertical displacement were recorded for our three different silicones. From the collected data, the vertical stretch and true stress were calculated and plotted (Fig. 5.13). It can be seen that for the stretch range tested (compression up to 60% of the initial height), the stretch-stress behavior is linear, thus justifying the use of Hooke's law made in section 2.3. The Young's modulus of the three elastomers can be calculated from the slope of their stretch-stress characteristic. The Dragon skin is clearly softer than the other two, with a Young's modulus of 0.21 MPa. The Nusil and Sylgard have similar Young's moduli of respectively 0.89 MPa and 1.16 MPa.

However, a simple calculation of the buckling voltage (i.e. the voltage at which the actuator starts moving, cf subsection 6.2.1) on our proof-of-concept Dragon Skin device, using the Young's modulus value obtained with the compression test, lead to a theoretical value of 200V, whereas measurements showed a real buckling voltage of 700V [28]. This discrepancy demonstrates the limitation of Young's modulus determination by compression tests on macroscale samples to predict the mechanical behavior of thin-film membranes. Indeed, many factors that can influence the mechanical properties of the membranes are not taken into account with the compression test, such as the effect of the solvent added for spin-coating the PDMS, the possible residual stress, and the stiffening effect of ion implantation. Consequently, an in-situ measurement of mechanical properties directly on the PDMS membranes is highly desirable to obtain valid data. We have therefore built and used a bulge test setup to characterize the mechanical properties of implanted and non-implanted thin PDMS membranes.

5.3.2   Bulge test measurement: principle and theory

The bulge test is a measurement technique used to characterize the material properties of thin films: Young's modulus, residual stress and Poisson ratio can

be determined with such a test. A freestanding membrane of known geometry (shape, size and thickness) is submitted to a pressure p on one of its sides (Fig. 5.14). The deflection of the membrane's center (z) is recorded, and material properties are extracted from the pressure-deflection curve, $p = f(z)$. This method has been successfully used to study the properties of silicon [75], silicon nitride [76], metallic [77, 78], and hard polymer [79, 80] thin films, as well as complex multilayer structures [81].

A bulge test setup designed and optimized to carry on measures on hard materials cannot be used to characterize thin PDMS membranes due to their extremely low Young's modulus, which is typically 4 to 5 orders of magnitude lower than that of metals. Indeed, a bulge test on hard materials requires the application of important pressures and the recording of small deflections. For PDMS thin films, however, small pressures need to be applied (< 2 kPa), and important deflections must be recorded (up to 300 μm for $\varnothing 3$ mm membranes). Additionally the high transmission of PDMS ($> 90\%$) renders the use of a laser interferometer to record the vertical displacement somewhat difficult. Evaporating a small gold circle at the center of the membrane to act as a mirror is not an acceptable method, as even a few nanometers of gold has an important impact on the membrane's stiffness, and would therefore influence the measurements.

We have built a bulge test setup specially designed for the measurement of soft films. The pressure is applied by a motorized syringe pump and a 10 cm^3 syringe through a large (300 cm^3) buffer volume, which allows to apply small pressure steps (< 1 Pa) per increment of the stepper motor. The applied pressure is measured by a barometric pressure sensor *MS5537* from Intersema[4] with a measurement range between 0 and 3 kPa and a resolution of 1 Pa. The measurement of the deflection is made with a white light interferometer *Wyko NT1100* from Veeco[5], which is well adapted for the measurement of our transparent membranes. Recording the deflection with the Wyko is much slower than with a laser interferometer, but it measures the height of a surface area and not just a single point. This allows to check for the membrane's flatness before starting, and to be sure to take the value of the deformed membrane's highest point during the measurement. The process is fully automated; a computer controls the different pieces of equipment (pump, pressure sensor, optical profiler) and stores the data. Typically, data is taken every 15 Pa between 0 and 600 or 1000 Pa.

The theoretical model which links the pressure on one side of the circular membrane to the deflection of its center is based on the assumption that the uniform pressure will deform the circular flat membrane into a spherical cap. In the case of thin membranes (thickness t much smaller than the radius r of the membrane), the relation between the biaxial stress σ in the membrane and the applied pressure p can be derived from the well-known equation for thin-walled spherical pressure vessels (Fig. 5.15). The equilibrium of forces along the z axis leads to:

$$\sigma 2\pi Rt = p\pi R^2 \ \Rightarrow \ p = \frac{2\sigma t}{R}, \tag{5.6}$$

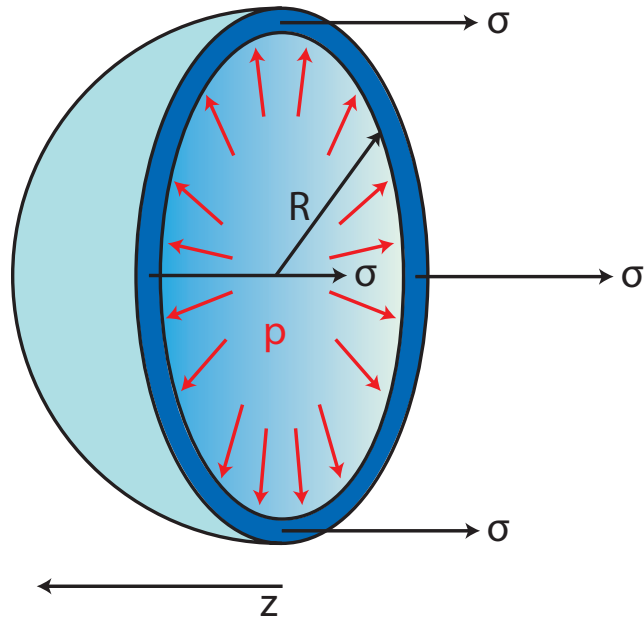[4]`www.intersema.ch`
[5]`www.veeco.com`

Figure 5.15: *Thin-walled spherical pressure vessel: the pressure p in a spherical pressure vessel of radius R creates an equi-biaxial stress σ in the vessel's membrane.*
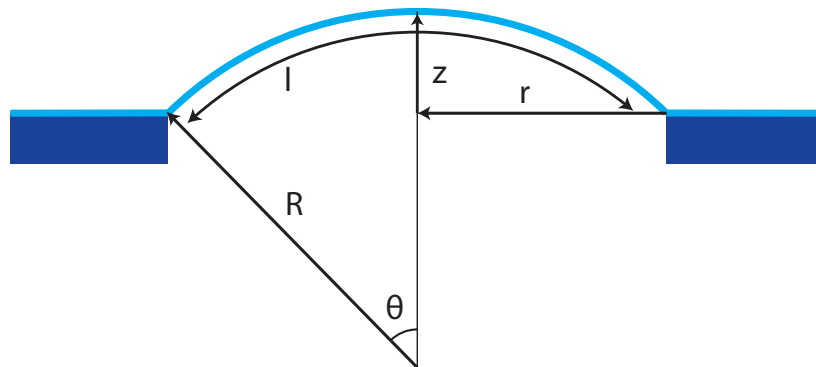

Figure 5.16: *When the circular membrane is deformed into a spherical cap, the radius r of the membrane and the vertical deflection of its center z determine the radius R of the sphere.*

where R and t are respectively the radius and thickness of the vessel. In the case of a circular membrane of radius r deformed into a spherical cap (Fig. 5.16), the radius R of the sphere can be calculated from the radius of the membrane, and the vertical deflection of its center z:

$$R^2 = (R - z)^2 + r^2 \;\Rightarrow\; R = \frac{z^2 + r^2}{2z}. \tag{5.7}$$

The membrane's deformation into a spherical cap will increase its area, and due to the constant volume properties of elastomer this will lead to a decrease of the membrane's thickness:

$$t = t_0 \lambda_z = \frac{t_0}{\lambda_a} = t_0 \frac{A_0}{A_{cap}} = t_0 \frac{\pi r^2}{\pi(r^2 + z^2)} = t_0 \frac{r^2}{(r^2 + z^2)}, \tag{5.8}$$

where $\lambda_{z,a}$ are respectively the thickness and area stretch ratios, and t_0 the initial membrane thickness. The bulge test equations found in the literature do not take this thickness reduction into account, as most of the reported results were obtained on hard thin-films, for which the vertical deflection reached during the test is often negligible compared to the diameter of the membrane ($z \ll r$). Furthermore, the fact that most of the tested material have Poisson coefficient around $0.2 - 0.3$ (typical of metals, silicon or silicon nitrides) contributes to limit the thickness reduction caused by the area expansion. For elastomers, however, this contribution can not be neglected, as the vertical deflection of thin PDMS membranes can reach 20% of the membrane's radius, leading to thickness decrease of 3.9%.

The link between the pressure, the stress, and the geometry of the membrane is obtained by introducing the equations 5.7 and 5.8 into equation 5.6:

$$p = \frac{4\sigma z t_0 r^2}{(z^2 + r^2)^2}. \tag{5.9}$$

The stress has two components: an elastic contribution due to the stretching, and the eventual presence of a residual stress σ_0, induced by the fabrication process, or by a voluntarily applied prestretch (cf. section 2.4):

$$\sigma = s\alpha Y^* + \sigma_0 = s\alpha \frac{Y}{1 - \nu} + \sigma_0, \tag{5.10}$$

where Y^* is the biaxial Young's modulus, Y the Young's modulus, ν is the Poisson coefficient, and s is the strain. α is a parameter that depends on the Poisson coefficient, and which accounts for the fact that the stress state at the membrane's border is not equi-biaxial due to the clamped boundary condition. Small and Nix have shown with numerical simulations that [82]:

$$\alpha \approx (1 - 0.24\nu), \tag{5.11}$$

The strain is calculated from the change of the arclength Δl divided by the initial arclength, and the arclength l is defined as (Fig. 5.16):

$$l = 2R\theta = 2\frac{z^2 + r^2}{2z} \arcsin\left(\frac{2rz}{z^2 + r^2}\right) \;\forall z \leq r, \tag{5.12}$$
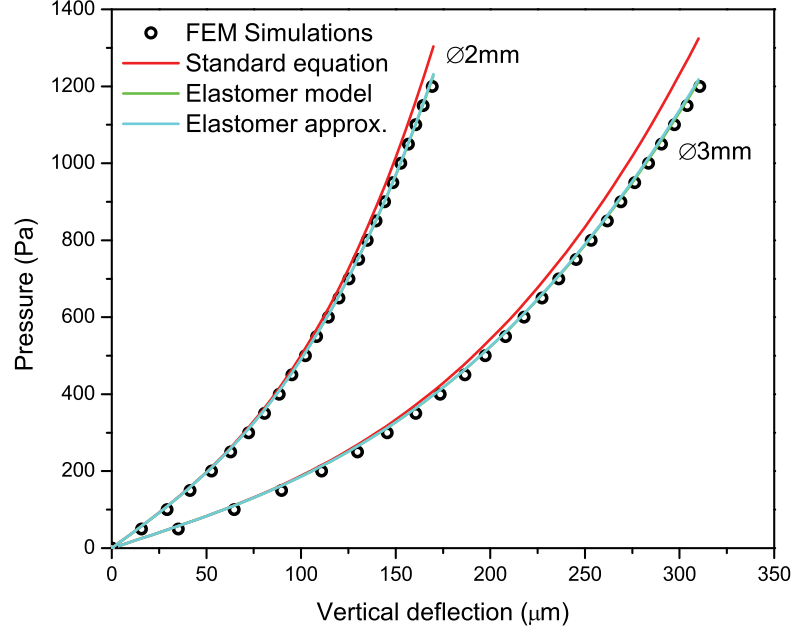
Figure 5.17: *Comparison of the three bulge test theoretical models (standard, elastomer, and elastomer approximation) with FEM simulations for $Y = 1$ MPa, $\sigma_0 = 30$ kPa, and $t_0 = 30$ μm. When the vertical deflection becomes important relatively to the membrane's diameter, the standard model diverges from the simulated data.*

which leads to the following formula for the strain:

$$s = \frac{l - 2r}{2r} = \frac{z^2 + r^2}{2zr} \arcsin\left(\frac{2rz}{z^2 + r^2}\right) - 1. \tag{5.13}$$

Finally, the relation between the pressure and the vertical deflection is obtained by combining the equations 5.9, 5.10, 5.11, and 5.13:

$$p = \frac{4(1 - 0.24\nu)Y}{1 - \nu} \frac{\left(\frac{z^2 + r^2}{2zr} \arcsin\left(\frac{2rz}{z^2 + r^2}\right) - 1\right) z t_0 r^2}{\left(z^2 + r^2\right)^2} + \frac{4\sigma_0 z t_0 r^2}{\left(z^2 + r^2\right)^2}. \tag{5.14}$$

A non-linear curve fit allows to extract the values of Y and σ_0 from the datapoints, knowing the geometrical properties of the membrane. The above formula can be simplified by replacing the arcsin function in the computation of the arclength (eq. 5.12) by the first two terms of its power series:

$$l \approx 2r(1 + \frac{2z^2}{3r^2}) \;\Rightarrow\; s \approx \frac{2z^2}{3r^2}. \tag{5.15}$$

For a vertical displacement over diameter ratio ($z/2r$) of 0.1, the strain calculated with the complete formula (eq. 5.13) is 2.65%, whereas the above approximation gives a strain of 2.67%, which is a very good approximation for

a considerably simpler formulation. Using this approximation to calculate the pressure-deflection law leads to:

$$p = \frac{8(1 - 0.24\nu)Y t_0 z^3}{3(1-\nu)(r^2+z^2)^2} + \frac{4\sigma_0 t_0 r^2 z}{(r^2+z^2)^2}. \tag{5.16}$$

The standard bulge test equations found in the literature for circular membranes (e.g. [79]) do not take the thickness change into account, and assume that the vertical deflection z is much smaller than the membrane's radius, which leads to a slightly different formula:

$$p = \frac{8(1 - 0.24\nu)Y t_0 z^3}{3(1-\nu)r^4} + \frac{4\sigma_0 t_0 z}{r^2}. \tag{5.17}$$

It can be observed that both equations gives the same pressure values when $z \to 0$.

A similar formula can be derived for square and rectangular membranes, but the situation is a little more complicated than for circular membranes, due to the lack of circular symmetry. Energy minimization methods can be used to obtain a relation linking the pressure to the vertical deflection [76]. By using rectangular membranes with different length over width ratios, the Poisson coefficient ν can be determined. However, for this study, ν was taken as a known parameter with a value of 0.5, and hence rectangular membranes were not used.

The validity of the three different models (elastomer model (eq. 5.14), elastomer approximation model (eq. 5.16), and standard model (eq. 5.17)) has been verified with FEM simulations. A model of a circular membrane with clamped boundary conditions was created with $ANSYS$[6] and submitted to a uniform pressure on one of its sides. The membrane's mechanical and geometrical parameters were chosen to be representative values for our samples. The Young's modulus, stress, and Poisson ratio were respectively set to 1 MPa, 30 kPa, and 0.5. The thickness of the membrane was chosen to be 30 μm, and two different diameters were used: 2 mm and 3 mm. The simulations were performed for pressures between 0 and 1200 Pa, with 50 Pa pressure steps. Using the same parameters, the theoretical curve $p = f(z)$ was calculated with the three models (Fig. 5.17). The standard model diverges from the numerical data when the vertical deflection becomes important relative to the membrane's diameter, because the assumptions on which it is based are no longer valid. This is particularly visible on the $\varnothing 3$ mm membrane, for which the $z/2r$ ratio exceeds 10% at 1200 Pa. The elastomer model provides a much better fit to the simulated data, and the elastomer approximation is indiscernible from the complete formulation, thus proving its validity in the deflection and pressure region of interest.

The FEM simulation data points were then used as a set of virtual experimental datapoints, and a non-linear curve fitting tool ($Origin~7.5$[7]) was used to extract the Y and σ_0 parameters using the standard model and the elastomer approximation model. The comparison with the expected values $Y = 1$ MPa and $\sigma_0 = 30$ kPa exposes the two models' capacity to accurately

---

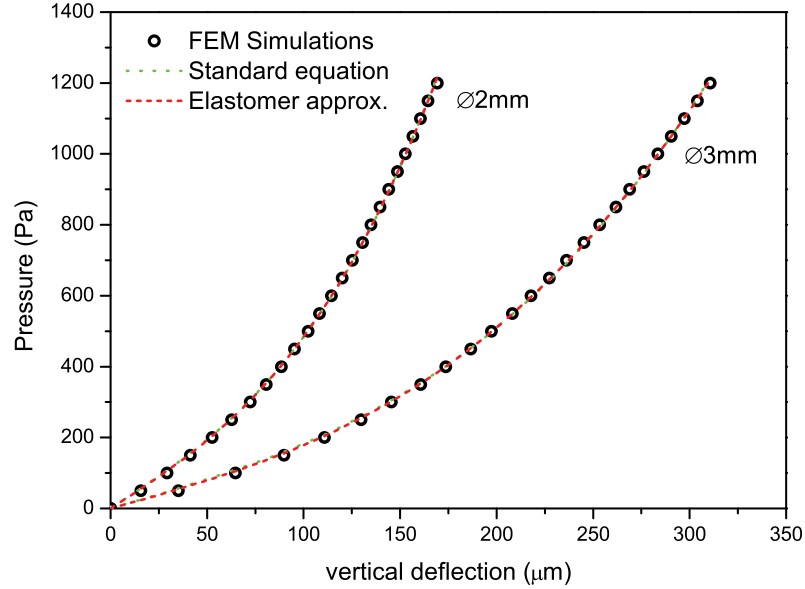[6]www.ansys.com
[7]www.originlab.com

Figure 5.18: *Fitting of the the standard and elastomer approximation models on the datapoints obtained from FEM simulations. Although both models lead to a good quality fit, the resulting parameters are different (table 5.2).*

Table 5.2: *Parameters extracted from the two models (standard and elastomer approximation) fitted on the simulation data, as well as relative error compared to the expected results, and fit quality χ^2/n.*

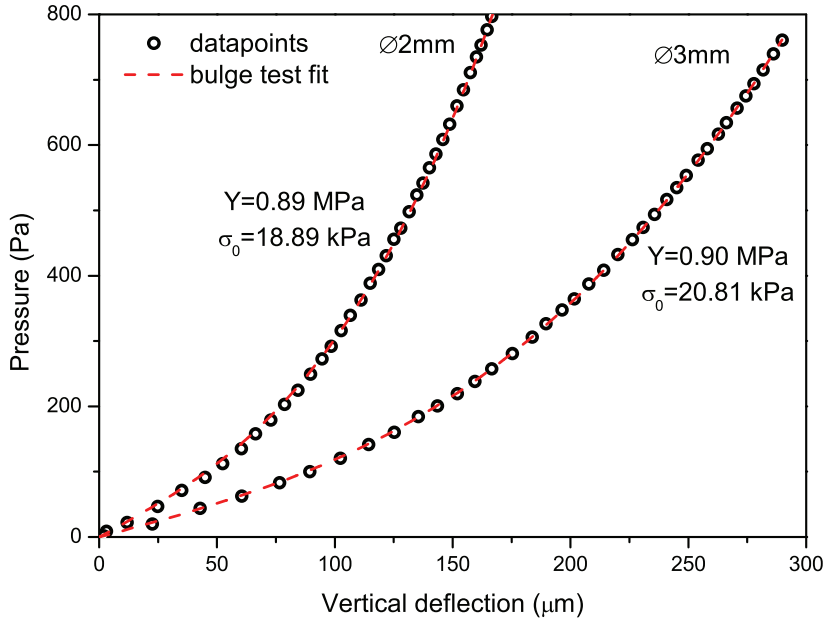| Model	Standard	Elastomer	Standard	Elastomer
$\varnothing$ (mm)	3	3	2	2
Y (MPa)	0.864 ± 0.009	1.009 ± 0.006	0.903 ± 0.011	1.012 ± 0.002
Y Error	-13.6%	$+0.9\%$	-9.7%	$+1.2\%$
σ_0 (kPa)	29.76 ± 0.35	28.53 ± 0.22	29.71 ± 0.27	29.27 ± 0.04
σ_0 Error	-0.8%	-4.9%	-1.0%	-2.4%
χ^2/n	43.9	15.8	38.4	2.1

Figure 5.19: *Data points and fit obtained on two circular $\varnothing 3$ mm and $\varnothing 2$ mm Sylgard 186 membrane 26.3 μm thick and polymerized at room temperature. The values of Y and σ_0 given by the fit are respectively 0.90 MPa and 20.8 kPa for the 3mm membrane, and 0.89 MPa and 18.9 kPa for the 2mm membrane.*

represent the dataset (Fig. 5.18 and table 5.2). The Young's modulus has a dominating influence at large deflections, and the standard model diverges from the numerical data for large values of z. Unsurprisingly, this model gives Young's modulus values about 10% lower than the expected value. The elastomer approximation model gives values of Y with a precision of about 1%. The standard model gives more correct values of σ_0 than the elastomer approximation, but this is a pure coincidence. Indeed, the stress has a strong influence at small deformations, at which bending energy – not taken into account in both models – has a non-negligible impact on the displacement-pressure characteristic. Consequently, the bulge test models, based exclusively on the membrane's stretching, are not expected to give accurate results for small values of vertical displacement. Coincidentally the bending-induced error and the imprecision of the standard model compensate each other and lead to better approximation of the stress. But the elastomer approximation model gives overall more accurate results, closer to the expected values, with less uncertainties, and with a better fit quality, as shown by the χ^2/n parameter, which represents the sum of the error squared divided by the number of degrees of freedoms (i.e. the number of datapoints minus the number of free parameters). The elastomer approximation model was used for the analyses presented in this document, and any further reference to a theoretical model for the bulge test implies the use of equation 5.16.

The measurement of the pressure and displacement values is very reproducible, and the measurement noise is quasi-nonexistent. The theoretical model

closely matches the datapoints and leads to excellent fit qualities (low χ^2/n values) and small uncertainties on the extracted parameters. Measurements on membranes of different sizes on the same chip lead to very similar values of the mechanical parameters of interest (Fig. 5.19). However, the accuracy of Y and σ_0 extracted from a bulge test measurement is directly linked to the precise determination of the different known geometrical parameters of the tested membrane. It is particularly important to have a precisely determined membrane's radius, as it is raised to the 4th power in the determination of the Young's modulus (eq. 5.17). De-bonding of the PDMS membrane from the Si substrate could cause a variation of the membrane's radius during the measurement and be the source of errors. However, even if it was not directly quantified, the O_2 plasma bonding of PDMS and silicon is very strong. Membranes have been inflated up to deformation ratios z/r of 1 (half-sphere) [83], without noticing any de-bonding. As a matter of fact, at high pressures, the membranes failed by tearing, but there was no damage to the bonded zone. As the Si chip's through-holes that define the membranes are patterned by photolithography and DRIE, their dimension is well controlled: mm-size holes can easily be patterned with a precision higher than ± 50 μm.

Both the residual stress and the Young's modulus directly depend on the membrane's thickness; an error in the thickness measurement will therefore directly impact the extracted values of Y and σ_0. Measuring the thickness of our PDMS membranes is not a straightforward step, and several techniques have been tried with moderate success. Mechanical methods such as alpha-step measurements deform the soft layer and lead to erroneous results, and most of the optical methods require precisely knowing the refractive index of the elastomer in order to obtain an accurate value. We use white light interferometry (the same equipment than for the bulge test) on a zone where the PDMS has been locally scratched to provide a step between the Si substrate and the PDMS surface. The downside of this technique is that the measurement is conducted on the bonded portion of the PDMS and not directly on the membrane. Furthermore, the scratching can create some local deformation of the PDMS. The accuracy of the measurement is estimated at ± 0.5 μm, which for a 30 μm-thick layer corresponds to an error of $\pm 1.6\%$. Combined with the other sources of error, the bulge test allows to determine Y with a precision of about 4%. The error on σ_0 is probably slightly higher due to the deviation of the bulge-test models at small displacement values caused by bending, as well as the measurement's extreme sensitivity to external perturbation (door motion, etc.) at small pressure values.

The deformed membrane's shape obtained with the simulations was compared to that of a spherical cap to control the validity of the deformed shape hypothesis on which the bulge test equations are based (Fig. 5.20). The clamped boundary condition on the membrane's edges makes it impossible to obtain a perfect spherical cap, but the deformed shape is nonetheless very similar to a portion of sphere.

5.3.3   Bulge test measurements on non-implanted PDMS

The first bulge test measurements we conducted on membranes that were polymerized in an oven at 100^oC showed the presence of a large residual tensile stress (above 50 kPa). To control that phenomenon in our layers, we tested
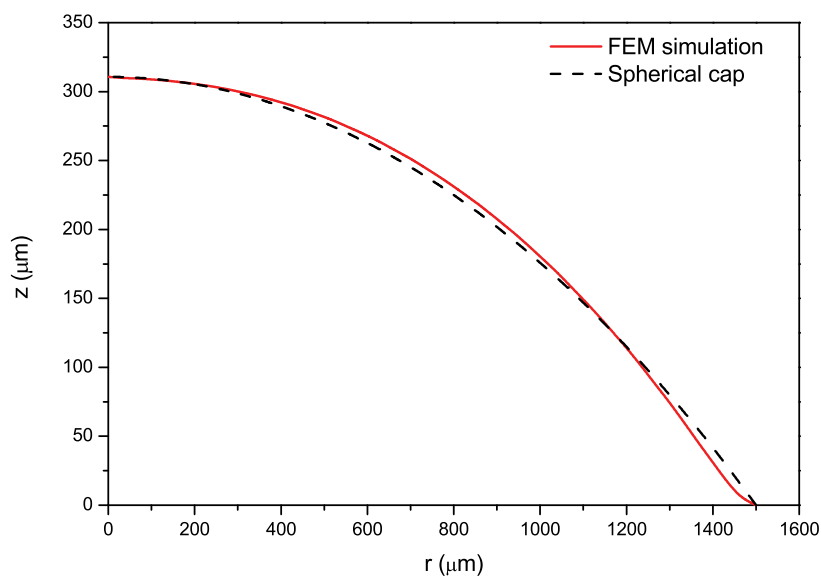
Figure 5.20: *Pressure-induced deformation along the radius of a circular membrane as calculated by FEM simulations. The membrane's parameters for the simulation are: $r = 1500$ μm, $t = 30$ μm, $p = 1200$ Pa, $Y = 1$ MPa, $\sigma_0 = 30$ kPa. The spherical cap deformation, on which the bulge test equations are based is also represented.*
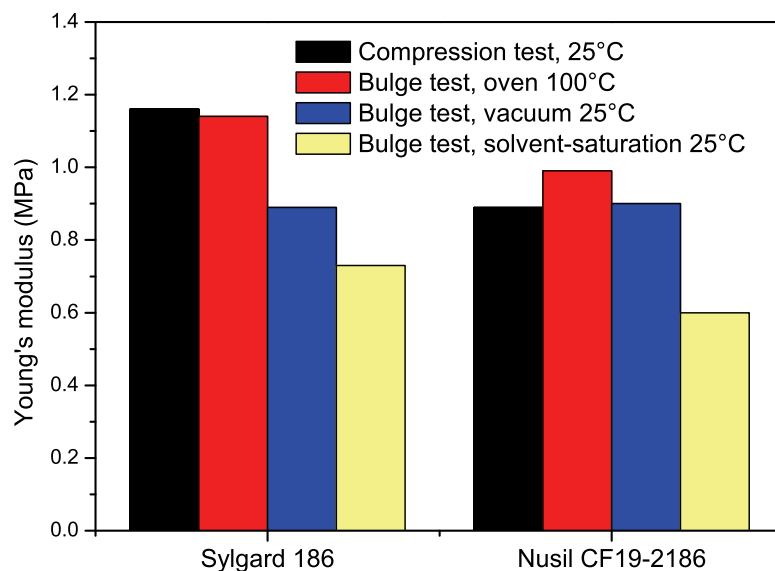

Figure 5.21: *Comparison of the Young's modulus of Sylgard 186 and Nusil CF19-2186 measured by uniaxial compression tests on macroscale samples, and by bulge test on suspended membranes. The macroscale samples were polymerized at room temperature, and three different curing conditions were used for the membranes.*
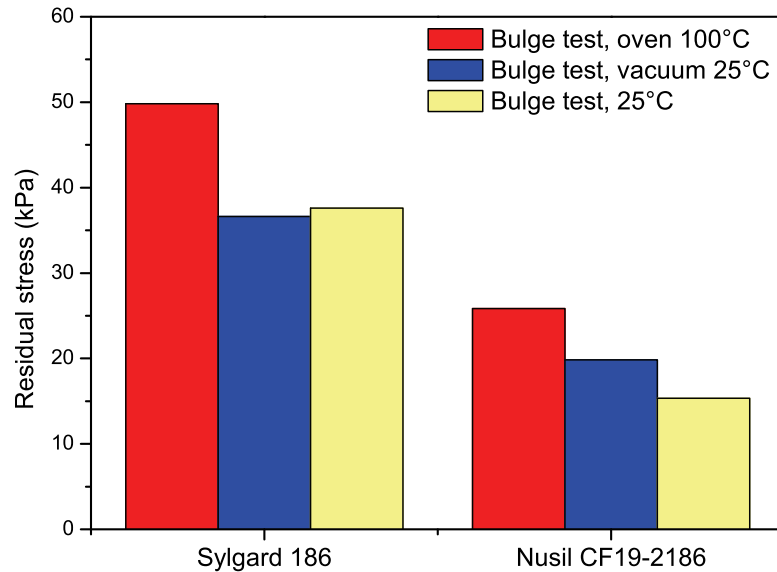
Figure 5.22: *Comparison of the residual stress of Sylgard 186 and Nusil CF19-2186 membranes, measured by bulge test. Three different curing conditions were used for the membranes' polymerization.*

two other curing methods in addition of the oven: polymerization in a vacuum desiccator in an attempt to remove the solvent from the PDMS before cross-linking occurs, and polymerization under a solvent-saturated atmosphere to keep the solvent in the PDMS during the polymerization and extract it afterward. Mechanical properties of membranes made with PDMS layers cured with the different methods described above were measured with the bulge test.

Results are presented in figures 5.21 and 5.22: mechanical properties are found to be strongly dependent on the external conditions during polymerization of the PDMS. Polymerization under the solvent-saturated atmosphere produced layers that remained sticky and less resistant to deformation, and which also have an elasticity modulus much lower than that obtained with other curing methods; consequently it has not been investigated further. For the two remaining methods, membranes made out of Nusil CF19-2186 exhibited a much smaller variation of its Young's modulus. The Nusil membranes polymerized under vacuum at room temperature have the same Young's modulus than the macroscale samples, which also were polymerized at room temperature.

Residual stress results (Fig. 5.22) show that polymerization at high temperature in an oven induces large tensile residual stress in the membranes, which is highly undesirable, for it increases the buckling voltage threshold of our actuators (cf. subsection 6.2.1). Nusil layers have lower residual stress than those made out of Sylgard. This lower residual stress combined with the smaller sensitivity of the Young's modulus to the curing conditions makes Nusil layers better candidates to make actuators.

Compared to compression tests on macroscale samples, bulge tests on membranes enabled us to quantify the non-negligible fabrication-induced tensile
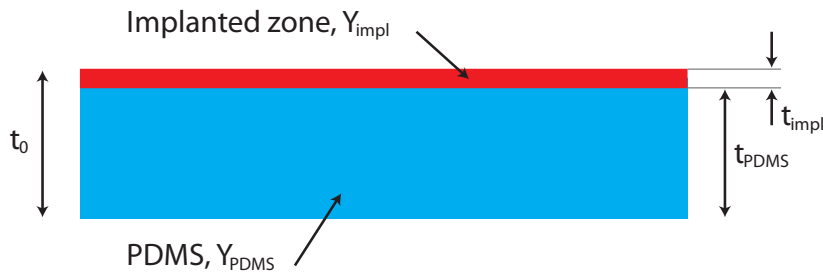
Figure 5.23: *Implantation on PDMS creates a bilayer with different Young's moduli and thicknesses.*

stress, and to monitor its – as well as the Young's modulus' – dependence on the PDMS curing conditions. Furthermore, bulge tests allow to quantify the change of a membrane's mechanical parameters induced by metal ion implantation, as described in the next subsection.

5.3.4 Bulge test measurements on implanted PDMS

Stretching tests have shown that electrodes created by metal ion implantation can sustain large deformations while remaining conductive (cf. section 5.2). However, another criterion must be taken into account in order to characterize the compliance of ion-implanted electrodes: the increase of Young's modulus induced by the addition of metallic particles into the PDMS. As exposed with the basic equations describing the deformation of a DEA with free boundary conditions (cf. eq. 2.12), the thickness strain – as well as the area strain – is inversely proportional to the Young's modulus of the PDMS. If the electrodes lead to an important stiffening of the actuator, its deformation capabilities for a given voltage will be reduced. A reasonable stiffening can be tolerated and compensated by the application of a higher voltage, but if the stiffening effect becomes too important, the voltage that needs to be applied to compensate for the stiffening may exceed the breakdown field limit and destroy the device.

Bulge test measurements were used to study the impact of metal ion implantation on the Young's modulus of suspended PDMS membranes. A set of membranes coming from the same PDMS sheet (i.e. with similar thickness, Young's modulus, and residual stress) were characterized with the bulge test, to extract their Y and σ_0. The membranes were then implanted with a given metal at 5 keV, and with different doses. A second bulge test measurement was made on the membrane to quantify the modification of their main mechanical parameters caused by the implantation. Each tested chip had two membranes of different lateral dimensions: 2mm and 3mm.

The bulge test on implanted membranes gives a global Young's modulus value, as if the membrane was an homogeneous compound with a constant Y value throughout its entire thickness. In reality, the implanted PDMS membrane is composed of two layers with different moduli: The PDMS layer of thickness t_{PDMS} with a Y equal to its value before implantation, and an implanted layer ~ 50 nm thick with a Y which is much higher than that of the PDMS (Fig 5.23). When the membrane is deformed into a spherical cap of height z larger than the membrane's thickness t_0, one can assume that stretch-

Table 5.3: *Initial parameters for the series of PDMS membranes used for quantifying the implantation-induced stiffening*

Implantation	t (μm)	Y (MPa)	σ_0 (kPa)
Gold	24.2 ± 1.2	0.86 ± 0.05	51.0 ± 2.4
Palladium	35.3 ± 0.3	1.22 ± 0.03	27.4 ± 1.4
Titanium	25.7 ± 0.3	0.69 ± 0.05	22.8 ± 0.4

ing dominates, and that the two layers are in an isostrain condition. The global modulus of the compound can be calculated from the addition of the two Young's moduli, ponderated by the volume fraction of each layer (Voigt model [7]):

$$Y_c = \frac{Y_{PDMS} \cdot t_{PDMS} + Y_{impl} \cdot t_{impl}}{t_{PDMS} + t_{impl}} \approx \frac{Y_{PDMS} \cdot t_0 + Y_{impl} \cdot t_{impl}}{t_0}, \quad (5.18)$$

where the indices c, PDMS, and impl respectively refer to the composite, the PDMS unaltered by implantation, and the layer affected by implantation. To simplify the expression, the following assumptions were made: $t_{PDMS} \approx t_0$, and $t_{PDMS} + t_{impl} \approx t_0$. The value of the Young's modulus extracted from bulge tests on implanted membranes is equal to the composite modulus Y_c given by equation 5.18.

For a given dose of metal, the isostrain Voigt model can be used to estimate the Young's modulus of the compound, if the metal forms a continuous metallic film on the surface of the PDMS (i.e. in the case of deposition on the PDMS' surface). This value can then be compared to the one measured on implanted membranes by the bulge test, in order to expose the difference of stiffening between *implantation* and the *deposition* of a continuous thin-film at the surface of the PDMS. If a dose D of atoms of a given element forms a continuous layer, the thickness t_d of this deposited layer can be calculated by the following equations: the weight per unit area w of the deposited metal is given by:

$$w = \frac{D \cdot M_m}{N_A} \text{ (g/cm}^2\text{)}, \quad (5.19)$$

where M_m is the molar mass (g/mol), and N_A is Avogadro number (at/mol). With the volumic mass ρ (g/cm^3) of the element, one can calculate the volume per surface area, i.e. the thickness t_d:

$$t_d = \frac{D \cdot M_m}{N_A \cdot \rho} \text{ (cm)}. \quad (5.20)$$

Using this calculated thickness value, as well as the Young's modulus of the metal in equation 5.18 gives the expected Young's modulus of the bi-layer structure, in the case where the metal forms a continuous layer at the surface of PDMS. For example, using gold's intrinsic properties ($\rho = 18.9$ g/cm^3, $M_m = 197$ g/Mol, and $Y = 78$ GPa [84]), one can calculate that a gold dose of $1.5 \cdot 10^{16}$ at/cm^2 leads to a continuous film thickness of 2.60 nm. If this film is deposited on a 25 μm-thick PDMS membrane with a Young's modulus
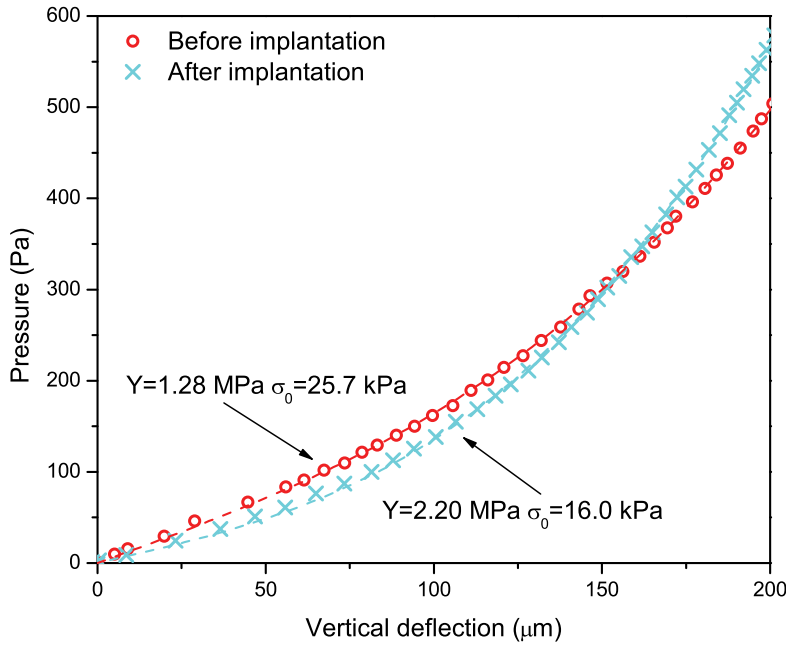
Figure 5.24: *Bulge test on a 3 mm membrane made before and after implantation with $1.2 \cdot 10^{16}$ at/cm^2 of Pd ions. The smaller slope at the origin for the implanted measurement shows the presence of a smaller residual tensile stress, while the faster pressure rise at higher displacements is the sign of an increased Young's modulus value.*

of 1 MPa, the isostrain Voigt model (eq. 5.18) predicts a resulting Young's modulus of 9.1 MPa for the bilayer structure, which corresponds to a 810% relative increase of the modulus, and would lead to a dramatic decrease of the actuator's performance.

For the case of implantation, the relative change of the Young's modulus $((Y_{impl} - Y_{PDMS})/Y_{PDMS})$ was calculated to represent the stiffening effect of implantation on PDMS. The measurement of the stiffening impact of implantation was made for membranes implanted with Au, Pd, and Ti. The membranes used for an implantation series with the same metal had very similar properties (Young's modulus, residual stress and thickness), but the three series had different properties, as summarized in table 5.3.

An example of a bulge test measurement made before and after implantation is given for a 3 mm membrane implanted with a a dose of $1.2 \cdot 10^{16}$ at/cm^2 of Pd ions (Fig. 5.24). The impact of implantation is clearly visible by comparing the measurement before the implantation to the one made after the implantation. The reduced slope at the origin after implantation shows that the residual stress has decreased. However, the slope is still positive, meaning that the stress has remained tensile, but with a smaller value than before implantation. In the other hand, the faster pressure rise at higher displacement values is due to an increase of the Young's modulus. For pressures between 0 and 300 Pa, the
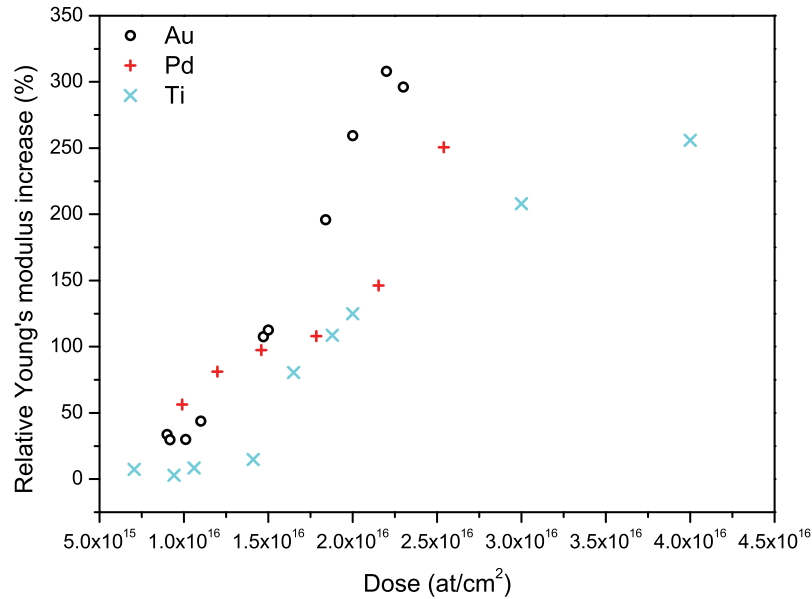
Figure 5.25: *Stiffening of PDMS membranes for Au, Pd, and Ti implantations at different doses. Direct comparison between the three metals is difficult because of different properties of the unimplanted membranes for the three series.*

implanted membrane exhibits larger displacement than before implantation due to the tensile stress reduction. Above 300 Pa the situation is reversed because the Young's modulus increase dominates.

The increase of the Young's modulus for different doses and metals as obtained from bulge test measurements is shown on figure 5.25. It appears from the measurement that titanium has a lower stiffening impact, followed by palladium, and gold. But if presenting the relative increase of the Young's modulus caused by implantation has the advantage of giving a figure that is both meaningfull and easy to understand, it is unfortunately dependant on the initial non-implanted parameters of the membrane, mainly thickness and Young's modulus. Indeed, given the same implantation parameters, the relative increase of modulus will be different on a 1 μm-thick membrane from a 100 μm one, and it will also be different on a PDMS with $Y = 0.2$ MPa from a PDMS with $Y = 10$ MPa. It should then be kept in mind that the values presented here are valid only for membranes whose initial Young's modulus, and PDMS thickness are comparable to the values of the membranes used for these tests.

It is consequently difficult to compare the stiffening between the three metals, due to the dissimilar properties of the unimplanted membranes for the three series (table 5.3). The fact that Pd implantations were conducted on thicker and stiffer membranes tends to lower the relative increase due to implantation compared to the other two metals. To solve this issue, the Voigt model can be used to separate the membrane into two separate layers, as mentioned above: the thin implanted layer, and the PDMS membrane, whose proper-
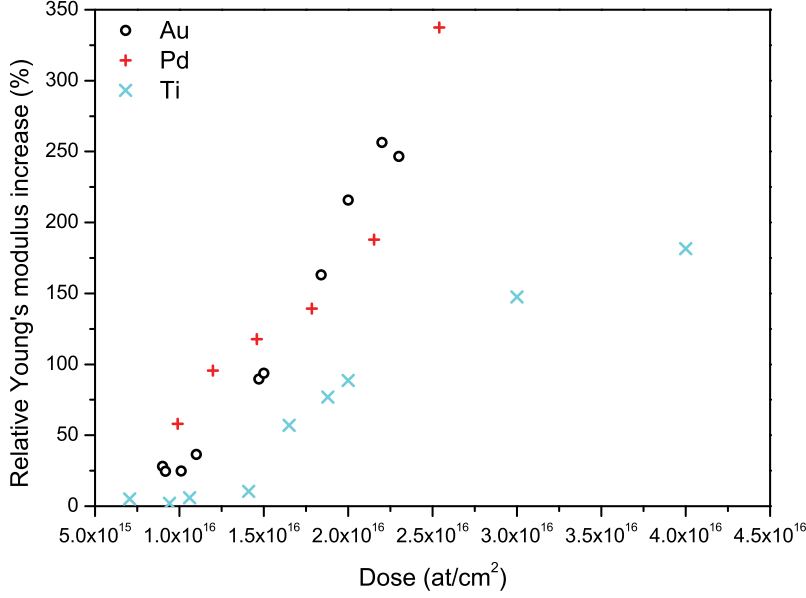
Figure 5.26: *Corrected stiffening of Au, Pd, and Ti implantations at different doses for a reference membrane with $Y_{ref} = 1$ MPa and $t_{ref} = 25$ μm.*

ties remains the same than before implantation. The implanted layer Young's modulus-thickness product can be calculated (eq. 5.18):

$$Y_{impl} \cdot t_{impl} = (Y_c - Y_{PDMS})t_0 \qquad (5.21)$$

This product characterizes the effect of implantation and depends on the process parameters (ions type, dose, energy, etc.). It is therefore quasi independent from the the properties of the PDMS layer underneath it, and it can therefore be used to calculate the stiffening caused by the same implantation on a reference membrane of initial Young's modulus Y_{ref} and thickness t_{ref}. The corrected Young's modulus Y_{corr} after the implantation of this reference membrane is defined by:

$$Y_{corr} = \frac{Y_{ref} \cdot t_{ref} + Y_{impl} \cdot t_{impl}}{t_{ref}} = \frac{Y_{ref} \cdot t_{ref} + (Y_c - Y_{PDMS})t_0}{t_{ref}} \qquad (5.22)$$

To be able to compare the stiffening of Au, Pd, and Ti implantations, the bulge test results were corrected according to equation 5.22 for a reference membrane of $Y_{ref} = 1$ MPa and $t_{ref} = 25$ μm (Fig. 5.26). The Pd implantation's points are the most affected by the correction, which shows that the stiffening due to Au and Pd implantation versus dose is very similar. Titanium implantation is shown to have the smallest impact on the stiffening of the PDMS membranes. The saturation observed for Ti at high dose (last two points) can be attributed to a possible sputtering phenomenon (i.e. an effective ion dose smaller than calculated from the number of pulses), similarly to the observation of surface resistance saturation for Au implantation at high doses
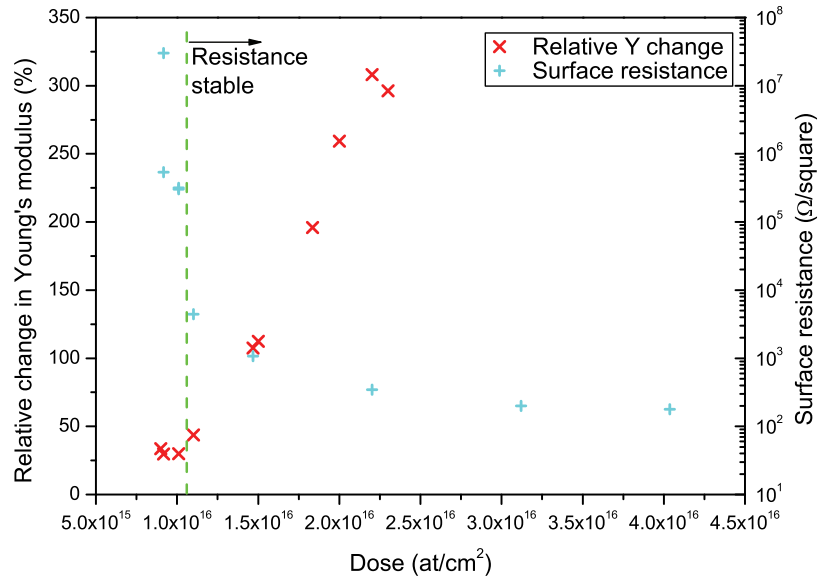
Figure 5.27: *Surface resistance and (uncorrected) Young's modulus increase versus dose for gold ion implantation on PDMS.*

(cf. section 5.1), or it can also be caused by the apparition of cracks in the implanted layer.

Determining which metal is the most suitable to make compliant electrodes for DEAs can not be based solely on measurement of the stiffening caused by the implantation. If this measurement shows that Ti seems the most appropriate of the three tested metals, one has to keep in mind that titanium implantations failed to produce layers that had a time stable resistance (cf. section 5.1). It is therefore necessary to relate the implantation-induced variation of the mechanical parameters with the surface resistance obtained for the same implantation parameters. Figure 5.27 shows the surface resistance and Young's modulus increase versus dose for gold ion implantation. It can be seen that the sharp decrease in surface resistance observed at the percolation threshold (around $1 \cdot 10^{16}$ at/cm^2) coincides with an increasing stiffening impact of implantation on the PDMS. There is however a narrow dose region, between $1.1 - 1.5 \cdot 10^{16}$ at/cm^2), in which a stable and low surface resistance can be obtained (< 10 kΩ/square), combined with a low impact on the Young's modulus increase (50-100%). This is approximately 8 times less than the calculations made above for a continuous thin-film. Not only does implantation allow to create electrodes that can sustain much larger strains compared to continuous thin films, but it also considerably reduces the stiffening impact of the electrode on the PDMS-electrode composite.

The ion dose information that appears on the last three figures is finally not a vital information to characterize the difference of properties obtained by implantation with the three metals. The two principal parameters that need to be analyzed are the surface resistance and the stiffening of the membrane. Plot-
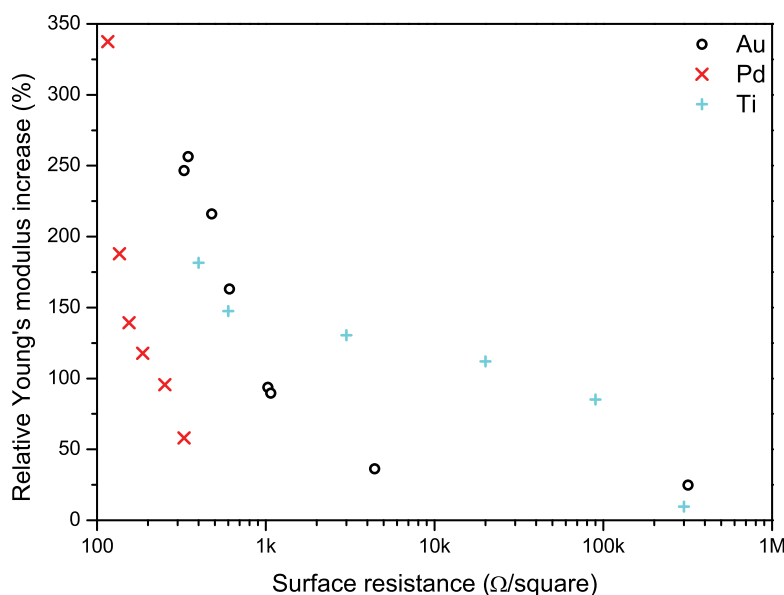
Figure 5.28: *Corrected relative increase of the Young's modulus versus surface resistance obtained for the implantation of Au, Ti and Pd on PDMS.*

ting the stiffening as a function of surface resistance (Fig. 5.28) clearly shows the general tradeoff between surface resistance and increase of Young's modulus, as well as the difference of properties obtained with the three implanted elements. Indeed, by looking solely at the stiffening versus dose measurements (Fig. 5.26), one doesn't see any major difference between Au and Pd implantations. Adding the surface resistance information shows that Pd implantations allow to obtain a better surface resistance for an equal stiffening compared to Au implantations.

Minimizing the stiffening of the membrane should be the priority for EAP devices, because having a very low resistance value is not necessary for electrostatic devices, as long as it is stable in time. Titanium is therefore not usable with its unstable surface resistivities (cf. section 5.1). While the stiffening versus resistance plot indicates that Pd is the most appropriate of the three metals to make compliant electrodes, the fact we were not able to obtain large strains while keeping electrical conduction for low-dose Pd implantations reduces the interest of this metal for DEA-related applications.

With the help of TEM crossections, Niklaus was able to measure the ion penetration into PDMS to ~ 50 nm. Using this value as t_{impl}, and the Y_c obtained by bulge tests, he was able to calculate Y_{impl}, the Young's modulus of the implanted layer, using the Voigt model. The obtained values were seen to be only a fraction of the Young's modulus of the bulk metal [62].

Implantation also has an influence on the residual stress of the suspended PDMS membranes, although the data is more difficult to analyze (Fig. 5.29). For all the tested doses and metals, implantation leads to a decrease of residual stress in the membrane. This is attributed to the inclusion of particles in
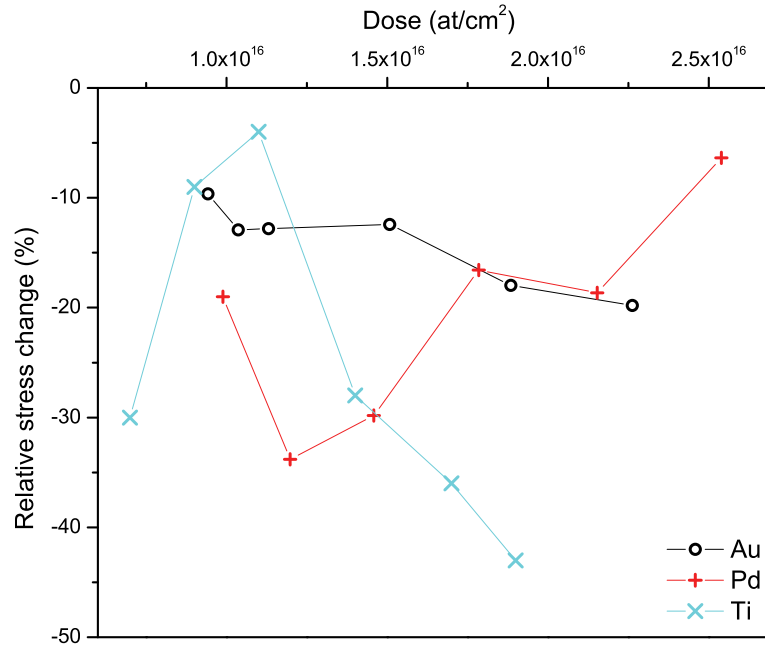
Figure 5.29: *Relative change in residual stress for different doses of Au, Pd, and Ti ions. The straight lines linking the points together are only a guide for the eye.*

the first tens of nanometer below the PDMS surface, thus creating a compressively stressed layer at the surface, which decreases the overall tensile stress in the membrane. However, the stress reduction versus dose behavior is difficult to interpret: If Au implantations exhibit a monotonous decrease of the stress with dose, this is not the case of Pd and Ti implantations for which a non-monotonous behavior is observed. No straightforward explanations for this behavior can be proposed, but the small stress values combined with the uncertainties on the stress computation by the bulge test could explain this phenomenon. The important message to keep in mind is that metal ion implantation on our membranes under tensile stress leads to a (not easily quantifiable) decrease of the stress. The residual tensile stress plays an important role in the displacement characteristics of our actuators (cf. chapter 6), and should be minimized. Ion implantation helps reduce the fabrication-induced stress of the membranes.

5.4   Dielectric breakdown field

Compared to carbon-based or metal-thin film electrodes, ion implanted electrodes will modify the surface of PDMS, due to ion penetration into the PDMS. Carbonization, chains scission and increase of surface roughness are likely to appear due to damage created by the dissipation of the incoming ions' energy. Concerns can be raised on the influence of ion implantation on the dielectric breakdown of the PDMS, as it is possible that the implantation-induced
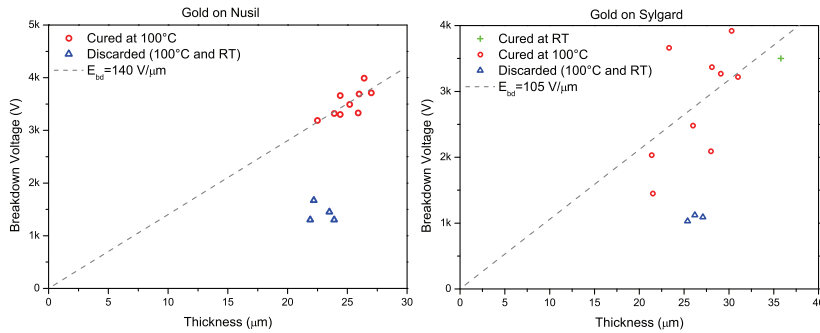
Figure 5.30: *Breakdown voltage of Au-implanted Nusil (left) and Sylgard (right) layers at 5 keV, for different PDMS thicknesses.*
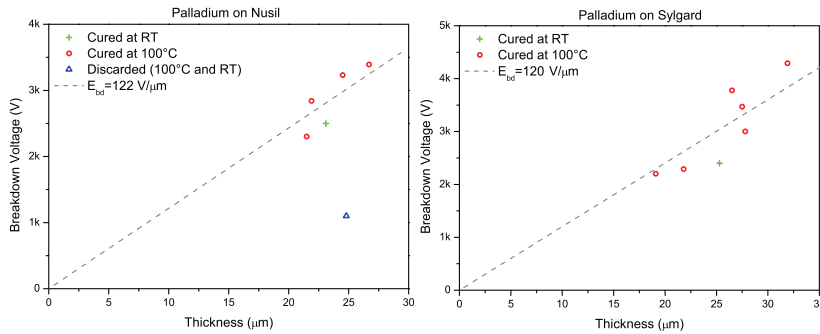

Figure 5.31: *Breakdown voltage of Pd-implanted Nusil (left) and Sylgard (right) layers at 5 keV, for different PDMS thicknesses.*

damage leads to a decrease of the dielectric strength of the PDMS. It is additionally possible that the use of solvent to lower the PDMS viscosity impacts the dielectric strength of the material. We have conducted extensive dielectric breakdown field measurements on different PDMS (Dow Corning Sylgard 186 and Nusil CF19-2186) of varying thicknesses ($19 - 35$ μm) to determine the maximal electric field that can be applied to our implanted membranes. Samples were prepared in such a way that the capacitor zone in which dielectric breakdown occurs was free from mechanical deformation due to the application of the electrical contacts, thus preventing them to have an influence on the measurement (cf. section 4.5).

Values of breakdown voltage versus PDMS thickness are reported in figure 5.30 for Au-implantations, and in figure 5.31 for Pd-implantations, with a linear fit to estimate the breakdown E field. Some datapoints with low breakdown voltages were discarded from the E field evaluation, as electrical failure for those samples was probably due to defects in the PDMS, such as dust or air bubbles. Although the electrostatic stress is important for applied electrical potentials around the breakdown voltage, there is no thickness reduction of the PDMS in this configuration, as the PDMS layer is bonded to the glass microscope slide and can not expand. This is specially true in the case where the electrode size is much larger than the PDMS thickness, which corresponds
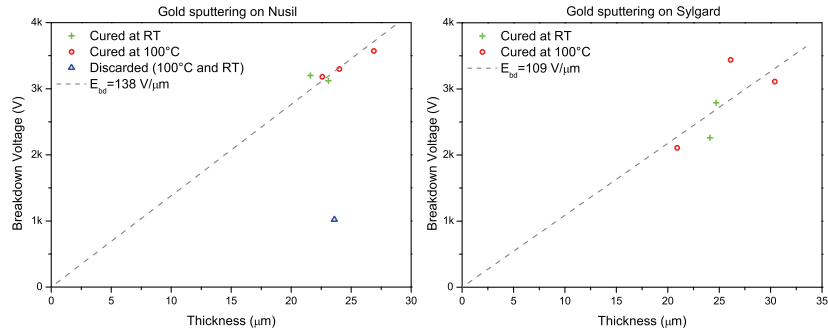
Figure 5.32: *Breakdown voltage of Gold-sputtered Nusil (left) and Sylgard (right) layers, for different PDMS thicknesses.*
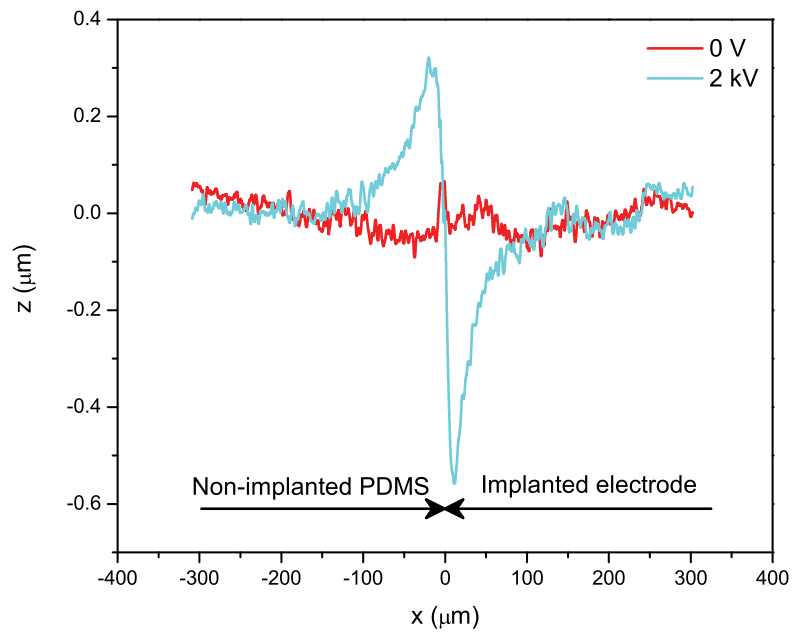

Figure 5.33: *Deformation induced at the electrode's periphery by a 2 kV electrical potential on a 29 μm-thick PDMS layer whose backside is bonded on a rigid substrate.*

Table 5.4: *Dielectric breakdown fields measured for two different PDMS (Sylgard 186 and Nusil CF19-2186) for different conditions: Not implanted, Pd- and Au-implanted*

	Sylgard 186 (V/μm)	Nusil CF 19-2186 (V/μm)
PDMS only	109	138
Pd implantation	120	122
Au implantation	106	140

to our situation with an electrode of 5×5 mm^2 and a PDMS thickness of $20 - 35$ μm. A localized deformation apprears at the electrode's border with a small dip on the implanted side, and a bump on the non-implanted side. Due to this local reduction in thickness at the electrode's periphery, the electric field is locally increased in this zone, but it was not taken into account to calculate the breakdown field, because it was measured with an optical profiler to be a fraction of a micrometer (Fig. 5.33), which is less than the PDMS thickness non-uniformity due to the spin-coating process (± 1 μm).

To compare the dielectric strength of implanted PDMS to that of the pristine material, similar samples were prepared, but the implanted electrode was replaced by a gold-sputtered electrode. Because sputtering creates a metallic layer on top of the PDMS (as opposed to implantation, which creates an electrode inside it), the breakdown field measured between the sputtered top and bottom electrode is taken to be the breakdown field of the tested pristine PDMS (Fig. 5.32). Table 5.4 summarizes the obtained results for dielectric breakdown measurements.

The measurements show that ion metal implantation does not alter the dielectric strength of the PDMS on which it is conducted, at least not at the low energies involved here (5 keV). Indeed, the breakdown fields obtained for implantation (for Au as well as Pd) are very close to those of unimplanted PDMS, and even superior in some cases, which shows that the damages provoked by the incoming ions are not the dominant factor in PDMS dielectric breakdown. Ion implantation can therefore be used to make compliant electrodes for DEAs without fear of altering the elastomer's dielectric strength. One can also observe that measurements made on Sylgard have more scatter than those made on Nusil. Nusil CF19-2186 is also easier to spin-coat than Sylgard 186 and leads to more uniform thickness on the wafer surface. This can be observed on the measurements by the wider range of thicknesses obtained with Sylgard, although the same rotation speeds were used for the 2 different PDMS: from a reproducibility standpoint, Nusil CF19-2186 appears to be more suitable.

Although we have seen with the bulge test that the curing temperature of the PDMS has an important influence on the mechanical parameters of the resulting cured PDMS layer (Young's modulus and residual stress) (cf. subsection 5.3.3), it does not have any impact on the dielectric strength of the PDMS, as the datapoints from layers cured at room temperature lie on the same line as data from the layers cured at 100^oC (Fig. 5.30–5.32). Consequently, the curing temperature can be selected in order to tune the membranes mechanical properties for a given application, without fear of an influence of the dielectric strength of the structure.

The measured dielectric strength of both PDMS is much higher than the value given by the manufacturer (13 V/μm for Sylgard 186 and 28.7 V/μm for Nusil CF19-2186). The differences may come from a security margin given by the manufacturer. Additionally, dielectric strength of thin-film may be higher than that of the bulk material due to the alignment of the polymer chains. Other authors also report on high breakdown field for those two polymers (as well as others) [15].

This study attracted our attention to the unexpected lower breakdown voltage that we observed on our actuators made on a silicon chip (< 60 V/μm) [85]. This was attributed to the creation of a high field zone induced by deformation of the PDMS layer at the external electrical contact points and was solved by replacing the Si chip by a Pyrex chip (cf. subsection 4.7.2).

5.5   Optical transmission of implanted membranes

Another interesting property of ion implanted electrodes is their optical transparency. Transmission measurements in the visible domain were conducted on Au- and Pd-implanted membranes at different doses (Fig. 5.34 and 5.35). Optical transmission is somewhat decreased after implantation due to light reflection from the metallic particles at the interface.

Au implantations were conducted on Sylgard 186 membranes, and Pd implantations were made on Nusil membranes. Both PDMS have a high optical transmission (93% for Sylgard, and 89% for Nusil for 25 μm membranes). Transmission decreases only weakly with dose, while remaining relatively high. Palladium implantations exhibit a monotonic relation between wavelength and implantation dose, with curves at different doses parallel to each other. At the highest tested dose, transmission remains above 56%. For gold implantation, transmission depends on the wavelength and is lower (35% for the highest dose) for red light, due to the very high reflection of IR by gold. The rather weak dependance on dose (clearly visible for palladium) is because reflection – rather than absorption – dominates. The transmission is decreased due to reflection at the air/PDMS+clusters interface, and the quantity of metal particles does not play a dominating role (Fig. 5.34). For Pd implantation, one can expect $\sim 40\%$ reflection at each interface.

Before implantation, the membrane is very smooth (surface roughness of pristine PDMS is below 2 nm RMS, as measured with an AFM) and interferences at the membrane's interfaces can be seen in the measurements. This is less visible on the implanted samples, particularly those with Pd, due to surface roughness increase caused by the implantation process. This relatively good transmission properties are unique to implanted electrodes and can not be achieved with thin-film or most of the carbon-based electrodes. This opens up a broad new field of applications for DEAs: those for which optical transmission is desirable. However, the increase in surface roughness due to implantation[8], may be an important drawback for the most demanding applications (such as imaging). One envisaged application of our diaphragm actuators is tunable lens arrays to make optical tweezers, in order to trap and move cells or small particles. In that case, the smoothness of the membrane is not the key parameters. However, the DEA membrane would have to sustain large amounts of

---
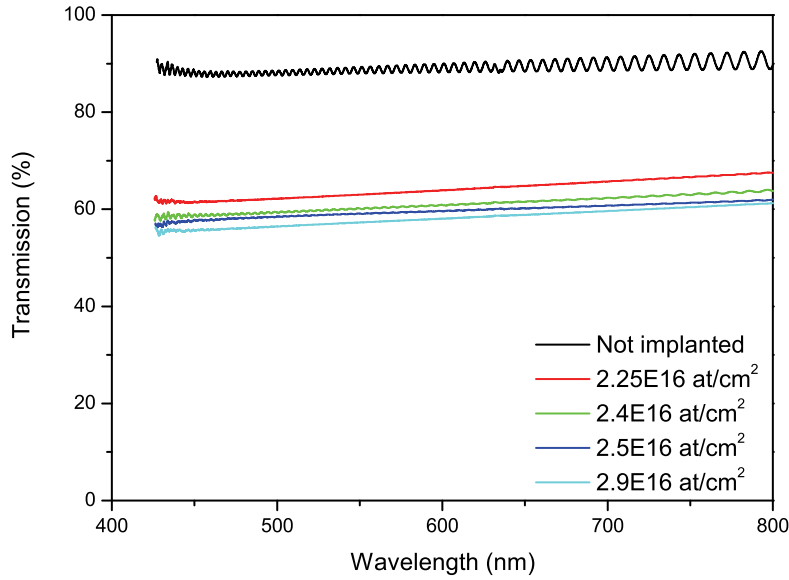
[8]Work of M. Niklaus, not yet published

Figure 5.34: *Optical transmission in the visible domain of PDMS layers (t = 25 μm) implanted with palladium on a Nusil layer.*

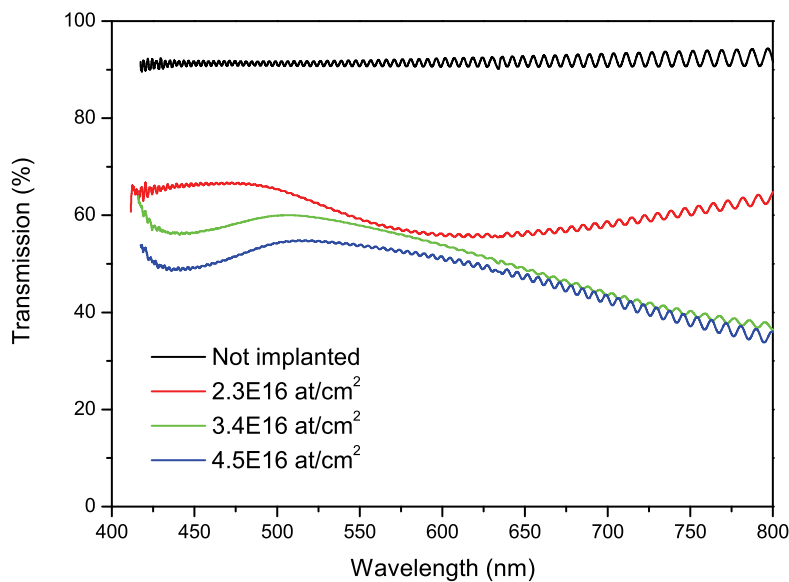**Figure 5.35:** *Optical transmission in the visible domain of PDMS layers (t = 25 μm) implanted with gold on a Sylgard 186 layer.*

light power without burning or degrading. We have tested the resistance of implanted PDMS membrane to high energy laser irradiation by submitting some samples to a pulsed IR laser beam. 1000 pulses of 10 ns with energy densities between 0.75 mJ/(mm$^2 \cdot$ pulse) and 3.5 mJ/(mm$^2 \cdot$ pulse) where sent through the membranes at rates varying between 5 and 20 Hz.

The PDMS membranes were undamaged by those tests, but the optical transmission after irradiation increased, which is probably caused by vaporization of part of the implanted/deposited layer. Further measurements are currently being made to quantify the change of electrical properties after irradiation, and the impact on actuator's performance. It should also be noted that the optical tweezers application mentioned above requires a continuous beam of moderate power (≈ 100 mW), compared to the high power ns pulses of the irradiation tests.

5.6   Concluding remarks

The applicability of metal ion implantation to make compliant electrodes for DEAs was shown in this chapter through different measurements and characterization methods. A time-stable resistance, high maximal strain before loss of electrical conduction, and a low stiffening impact on the elastomer are the three crucial parameters which characterize compliant electrodes. The results presented in this chapter showed that the three tested metals (gold, palladium and titanium) exhibit very different behavior in respect of these three criteria. Gold is the only tested metal that outstandingly fulfill the requirements of compliant electrodes. The strips implanted with doses of $400-500$ pulses $\cdot$ cm^{-2} combine a low resistance ($150-200 \, \Omega$/square) with a high maximum strain ($> 170\%$), a low degradation and a low impact on the elastomer's Young's modulus ($+50\%$ to 100%). The measurements show the existence of an optimal dose at which the best performance is obtained for the most important parameters: the samples which remain conductive at the largest strains are also the ones which have the longest lifetime in terms of cycles (slowest degradation). By comparison, the Pt electrodes of Urdaneta et al. exhibit low degradation for a Pt-salt concentration which yields electrodes with small maximum strain, and faster degradation for conditions yielding electrodes with larger maximum strain [71].

The important difference in strain capabilities between Pd and Au implantations remains partly unexplained at this time, but the microstructure of the elastomer layer affected by the implantation was shown to be different for the two metals by TEM observation of implanted PDMS crossections. Pd clusters are larger than gold clusters at comparable dose. Pd-implantations lead to lower sheet resistance than gold, but also to much smaller strains before loss of electric conduction, due to its larger clusters' size. If Au is the most suitable among the three tested metals, it is not necessary the best of all possible metals, and further investigation will be conducted with other elements, such as copper and aluminium. It is maybe possible to find a metal that will cause a smaller stiffening impact, while keeping the large strains capabilities and the stable resistance.

The field of application of ion-implanted electrodes goes well beyond DEA-related devices. Indeed, the emergence of the use of polymers as functional materials, as well as the fabrication of electronic circuits on flexible and deformable

substrates, have brought the need for reliable stretchable and deformable electrodes. Expandable and rollable displays [64, 86] as well as flexible electronics [87] are two examples of applications that require important deformation or stretching of a conducting material. The amount of strain that the electrode must be able to sustain without damage, as well as the number of strain cycles to which the electrode will be submitted depends on the application. It can vary from a single deformation of a few percent (for example for an implantable sensor that needs to adapt its shape to the environment in which it is inserted), to repeatable stretching above 100% strain in the case of DEAs, which clearly represent a very demanding application for compliant electrodes. The results and related discussions presented in this chapter were targeted on DEAs. For other applications, different conclusions would be reached as to the best metal and dose to use.

The results and developments of this chapter were presented at the SPIE's Electroactive Polymer Actuators and Devices (EAPAD) conference in 2007 [88] and 2008 [89], as well as accepted for publication in Advanced Functional Materials (October 2008).

Chapter 6

Application of metal ion implantation to diaphragm dielectric elastomer actuators

The previous chapter has demonstrated the outstanding compliant properties of ion-implanted electrodes, which are characterized by low surface resistance, low stiffening impact on the elastomer, and large strain capabilities (cf. chapter 5). This chapter focuses on the use of these implanted electrodes to make miniaturized circular diaphragm DEAs, as well as on the characterization of these devices. Analytical models describing the behavior of the membranes will be introduced and analyzed. Next, the results of the measurements will be presented: static deflection, behavior under a mechanical load, and dynamic response. Examples and dimensioning of a few applications of the diaphragm actuators will conclude this chapter.
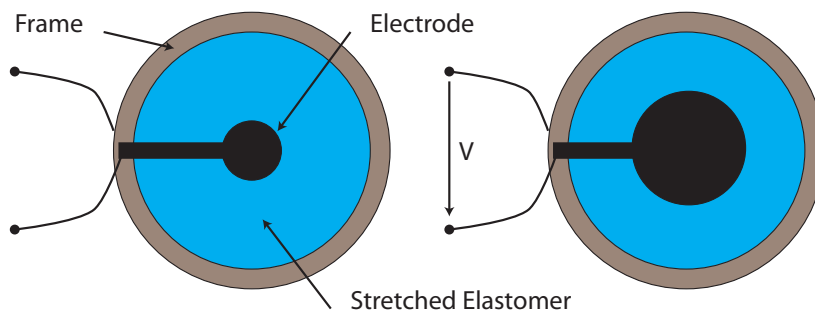

Figure 6.1: *Schematic representation of a typical area strain DEA. The circular electrodes are patterned on both sides of a prestretched elastomer film. Upon application of a voltage, the surface of the compliant electrodes increases dramatically.*
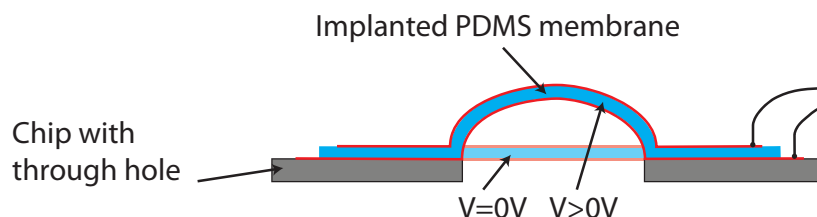
Implanted PDMS membrane

Chip with
through hole

V=0V V>0V

Figure 6.2: *Our diaphragm actuators consist of non-prestretched suspended PDMS membranes implanted on both sides over the whole surface. Because of the clamped boundary conditions, applying a voltage causes the formation of a bump, whose height can be controlled by the applied voltage.*

6.1   Geometrical configuration

A large number of DEA demonstrators are based on a highly prestretched membrane with a circular electrode [2, 12, 15, 24]. Upon application of a voltage, the zone covered by the electrode expands, and the prestretch-induced tensile stress relaxes in the zone which is not covered by the electrode (Figure 6.1). A camera is used to record the change in area of the electrode, in order to measure the area stretch versus voltage. Due to the high prestrain levels of this kind of actuators, the pull-in limit (cf. sections 2.3 and 2.4) can be exceeded, and area strains above 100% can be obtained [15], which makes very impressive demonstrators. However, we have not retained this configuration to make ion-implanted miniaturized demonstrators. We indeed wanted to have a process flow as compatible as possible with standard microfabrication steps. Our elastomer layers, for example, are obtained by spin-coating an uncured PDMS mixture on a substrate, and can consequently not be prestretched. Bulge test measurements on non-implanted PDMS have shown that our process produced PDMS layers under a slight tensile stress (cf. subsection 5.3.3). However, the obtained values correspond to a prestretch smaller than 5%, which is ten to forty times less than the intentional prestrain that is usually applied to these circular strain actuators. The second reason that kept us away from this actuator configuration is the difficulty to make anything useful out of it. They may be visually impressive, but it is not trivial to convert the area strain they produce into usable mechanical work, although Lacour et al. demonstrated a possible solution by fixing a solid block on the actuator, which was put into horizontal motion by the area strain of the DEA [27, 90].

Our demonstrator actuators combine the design and fabrication simplicity of the area strain actuators described in the previous paragraph with out of plane motion which can be directly converted into mechanical work. They consist of suspended circular PDMS membranes with electrodes that cover the entire membrane surface. The PDMS is not prestretched (except for the $15 - 50$ kPa of tensile stress induced by the fabrication process), and applying a voltage between the electrodes leads to a surface expansion. Because of the clamped boundary condition, in-plane deformation of the membrane cannot occur, and the PDMS membrane forms an out-of-plane bump whose height can be modulated by the applied voltage (Figure 6.2). Three versions of these diaphragm actuators were fabricated: on a silicon chip (cf. subsection
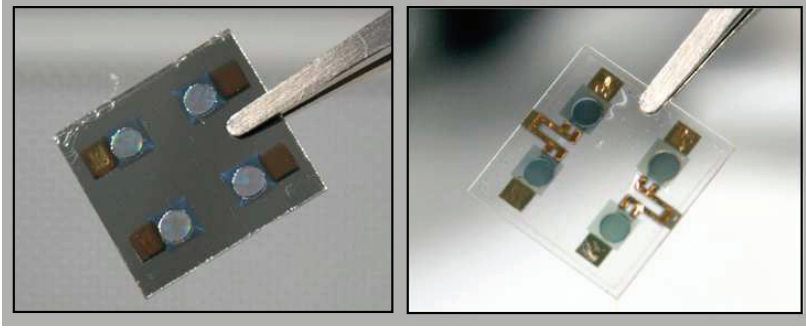
Figure 6.3: *Pictures of the actuator on Pyrex (left), and the actuator with patterned backside implantation for a good electrical contact (right).*

4.7.1), on a Pyrex frame (cf. subsection 4.7.2), and on a Pyrex frame with a patterned backside implantation (cf. subsection 4.7.3). The behavior and governing equations of these three actuator versions are identical, and they only differ by their response speed or maximal applicable voltage before breakdown. Figure 6.3 shows the finished diaphragm actuators.

6.2 Analytical model of the actuators

6.2.1 Buckling analysis

The situation of the suspended membrane submitted to an electric field is very similar to the general example describing DEAs' actuation (cf. section 2.3), except that in the case of a suspended membrane the in-plane area expansion cannot take place due to the fixed boundary condition at the diaphragm's periphery. In the case of stress vectors along the three principal axes, the 3D generalized Hooke's law lead to a strain vector $\overrightarrow{s}$ which is linked to the stress vector by:

$$\overrightarrow{s} = \frac{1}{Y} \begin{bmatrix} 1 & -\nu & -\nu \\ -\nu & 1 & -\nu \\ -\nu & -\nu & 1 \end{bmatrix} \begin{pmatrix} \sigma_x \\ \sigma_y \\ \sigma_z \end{pmatrix}. \tag{6.1}$$

In the case of an unstressed suspended PDMS membrane with clamped boundary conditions, and for a small applied voltage on the electrodes, the in-plane strain will be null ($s_x = s_y = 0$), the two in-plane stresses will be equal (i.e. equi-biaxial stress, $\sigma_x = \sigma_y = \sigma_p$, where σ_p is defined as the in-plane stress), and the vertical stress is given by the basic DEA electrostatic pressure equation (eq. 2.7). Taking the incompressibility property of elastomer into account ($\nu = 0.5$), this leads to the following equation:

$$\begin{pmatrix} 0 \\ 0 \\ s_z \end{pmatrix} = \frac{1}{Y} \begin{bmatrix} 1 & -1/2 & -1/2 \\ -1/2 & 1 & -1/2 \\ -1/2 & -1/2 & 1 \end{bmatrix} \begin{pmatrix} \sigma_p \\ \sigma_p \\ \sigma_z \end{pmatrix}, \tag{6.2}$$

from which the following equalities can be obtained:

$$s_z = 0 \tag{6.3}$$

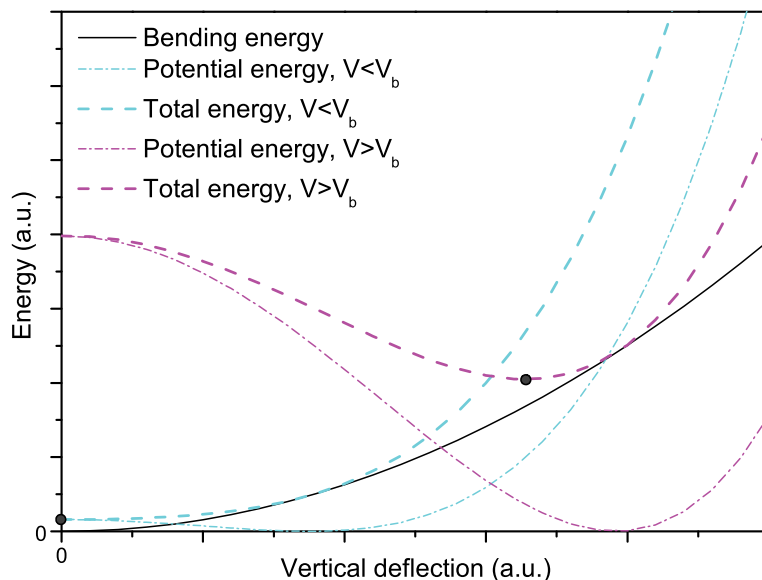$$\sigma_p = \sigma_z = -\epsilon_0 \epsilon_r E^2. \tag{6.4}$$

Figure 6.4: *Schematic representation of the bending energy (independent of the applied voltage), the potential energy (for two different voltage values, one above and one below V_b), and the total energy versus membrane's displacement. The equilibrium point is reached for a minimal energy and is indicated with a dot. For voltages below the buckling threshold, the equilibrium point is obtained at $z = 0$.*

Due to the incompressibility condition, the absence of area expansion leads to no thickness reduction and an isostatic stress condition. The stress on the three principal axes are equal, and the strain components on the same axes are null. The electrostatic field modifies the stress state of the membrane, but doesn't cause any displacement. Applying an electric field on an initially unstressed membrane creates a compressive isostatic stress in the membrane.

Similarly to a compressed spring, the activated membrane stores mechanical energy, and mechanical elements under compressive stress are unstable and are subject to buckling if the stress reaches a critical level, known as the elastic stability limit. Below this limit, also known as the buckling threshold, the total mechanical energy (the sum of the stored potential energy due to the electric field and of the bending energy of the deformed membrane) is minimized when the membrane is flat, and no motion is observed. But for compressive stresses higher than the buckling threshold (σ_b), the minimized energy is obtained when the membranes deforms vertically along the z axis (Figure 6.4). Consequently, out-of-plane deflection is observed for stress values higher than σ_b, and as the compressive stress is directly controlled by the voltage applied on the membrane, the vertical deflection can be voltage-modulated (Figure 6.5). Because the energy functions are symmetric, there are two stable equilibrium points above the buckling voltage for $z = \pm z_{eq}$.

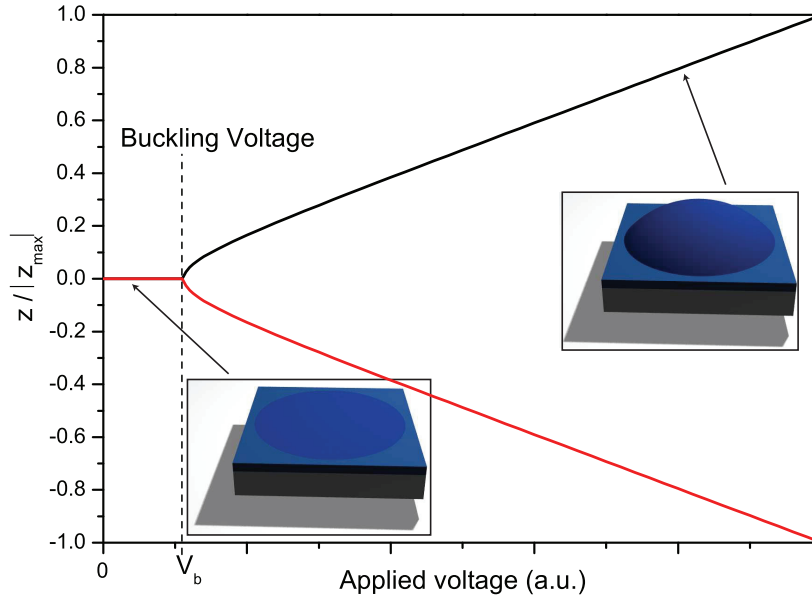The critical compressive stress σ_b at which first-mode buckling occurs for

Figure 6.5: *Schematic representation of the displacement versus voltage behavior for the diaphragm actuators. No displacement is observed for voltages below the buckling limit. For higher voltages, the displacement can theoretically occur either upwards or downwards.*

clamped circular membranes is given by [91]:

$$\sigma_b = -1.22 \frac{Y}{1-\nu^2} \left(\frac{t_0}{r} \right)^2 . \tag{6.5}$$

It depends on the Young's modulus of the PDMS used for the membrane, and on the membrane's geometry. Figure 6.6 shows critical stress values for different membrane sizes with a PDMS whose Young's modulus is 2 MPa. For a 30 μm-thick $\varnothing 2$ mm membrane, the critical stress equals -2.93 kPa. Because of the isostatic stress state in the membrane up to the buckling point, the compressive electrostatic stress σ_z must reach this limit before one can observe out-of-plane deflection, and the buckling voltage can be calculated by combining equations 6.5 and 2.7 in the case of an initially unstressed membrane.

However, one has to keep in mind that our PDMS membranes present a residual tensile stress between 20 and 50 kPa (cf. subsection 5.3.3), which has a non-negligible impact on the buckling voltage. Due to the superposition principle, equation 6.4 can be modified to take into account the residual in-plane stress in the membrane σ_0:

$$\sigma_p = \sigma_0 + \sigma_z = \sigma_0 - \epsilon_0 \epsilon_r \left(\frac{V}{t_0} \right)^2 . \tag{6.6}$$

Buckling occurs when the in-plane stress reaches the critical level σ_b, and combining equations 6.5 and 6.6 allows to determine the voltage V_b at which this
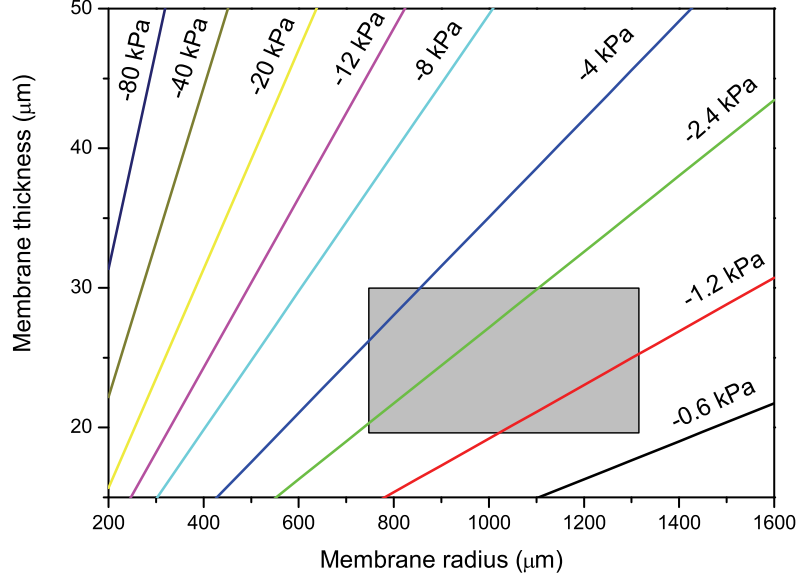
Figure 6.6: *Calculated critical buckling stress for circular elastomeric membranes of different radius and thickness for a material with Y=2 MPa, which is representative of our implanted membranes. The typical membrane's geometries used for our actuators fall within the gray rectangle.*

instability occurs:

$$\sigma_b = -1.22\frac{Y}{1-\nu^2}\left(\frac{t_0}{r}\right)^2 = \sigma_0 - \epsilon_0\epsilon_r\left(\frac{V_b}{t_0}\right)^2 \Rightarrow$$

$$V_b = \frac{t_0}{\sqrt{\epsilon_0\epsilon_r}}\sqrt{\sigma_0 + 1.22\frac{Y}{1-\nu^2}\left(\frac{t_0}{r}\right)^2} \qquad (6.7)$$

The previous equation shows that the applied voltage (and therefore, its related electrostatic pressure) will have first to compensate the residual tensile stress σ_0, and then to reach the compressive critical stress in order to obtain vertical motion. For our membrane's geometries ($\varnothing = 1.5-3$ mm, $t_0 \approx 20-30$ μm), the dominating component is clearly the residual tensile stress, which (on implanted membranes) varies between $10-40$ kPa, compared to the critical stress which (for a $Y = 2$ MPa) is typically smaller than -5 kPa. As it is desirable to decrease the voltage needed to actuate the devices, care should be taken to minimize the buckling voltage. It is consequently necessary to make PDMS layers with the lowest possible residual stress, hence our investigations to find a curing method for the PDMS that minimizes this issue (cf. subsection 5.3.3). In parallel, the critical buckling stress can be minimized by using membranes with a low t_0/r ratio. If this ratio is low enough, the buckling voltage depends only on the residual stress and becomes independent from the membrane's diameter: membrane of different sizes should start moving at the same voltage. Reducing the thickness is particularly interesting, because it decreases the critical stress

needed for buckling, and it also lowers the voltage necessary to obtain the electrostatic pressure corresponding to the stability limit. If the residual stress and/or the t_0/r ratio are too high, the electric field needed to reach the elastic stability limit may exceed the breakdown field of the PDMS, and the device would fail before any motion can be observed, which was an issue that plagued our first actuators on Si chips made with Sylgard 186 polymerized at $100^o C$.

The buckling voltage calculated by equation 6.7 is a theoretical value based on the assumption of a perfectly flat membrane. In practice, initial deformation of the membrane causes small displacements even for an applied voltage lower than V_b. Depending on the membrane's initial flatness, the buckling threshold can be more or less visible, as it will be presented later (cf. section 6.3).

6.2.2 Prebuckling behavior

As explained above, when a voltage below V_b is applied to the diaphragm actuator, no vertical deflection is observed. However, the stress state of the membrane is modified by the applied electrostatic pressure. As the resonance frequency of membranes is dependant on the in-plane stress, it is possible to voltage-tune the resonance frequency of suspended membranes from an initial value f_0, down to 0 at the buckling limit.

Resonance frequencies of circular bodies can be easily calculated for two particular situations: 1) for membranes, which are characterized by a negligible thickness ($t_0 << r$) and an important tensile stress (drum membranes for example), and 2) for plates, which are thin unstressed circular body ($t_0 < r$). The first mode (i.e. 1 nodal circle, 0 nodal diameter) resonance frequency of circular drum membranes (f_{drum}) is given by [92]:

$$f_{drum} = \frac{0.383}{r}\sqrt{\frac{\sigma_p}{\rho}}, \qquad (6.8)$$

where σ_p is the membrane's in-plane stress, and ρ, the membrane's density. The first mode resonance frequency of a circular plate (f_{plate}) is given by [92]:

$$f_{plate} = \frac{1.623 \cdot t_0}{r^2}\sqrt{\frac{Y}{12(1 - \nu^2)\rho}}. \qquad (6.9)$$

The membranes used throughout this project are too thick relative to their diameter to neglect bending and to apply the stress-controlled membrane model for the determination of their resonance frequency. In the other hand, their residual stress is too high to consider them as pure bending-dominated plates. In other words, both tension and bending have an influence on the resonance frequency of the PDMS membranes. Strictly speaking, using the word *membrane* to describe our PDMS diaphragms is an abuse of language, as their behavior – partly bending-, partly stress-dominated – lies somewhere between that of plates and that of membranes. However, we will keep using the words membranes and diaphragm indifferently to describe our suspended PDMS structures.

We have used a Rayleigh-Ritz energy method to calculate the resonance frequencies of our circular diaphragms, by assuming an identical first mode shape for the bending- and stress-dominated resonance frequencies. The time-

dependant deflection $\tilde{w}(x, y, t)$ is given by [93]:

$$\tilde{w}(x, y, t) = \tilde{w}(x, y)\cos(\omega t), \qquad (6.10)$$

where $\tilde{w}(x, y)$ is the assumed mode shape, which is modulated by a cos wave of frequency $\omega/2\pi$. The velocity of each surface elements depends on the position (x, y) and the time t. The maximal velocity v_{max} is obtained for $t = \pi/2\omega$, i.e. when the membrane is flat:

$$v_{max}(x, y) = \left.\frac{\partial \tilde{w}(x, y, t)}{\partial t}\right|_{t=\pi/2\omega} = -\omega\tilde{w}(x, y). \qquad (6.11)$$

This allows to calculate the maximal kinetic energy $\hat{E}_k$ by integrating the maximal kinetic energy density on the whole membrane's area a:

$$\hat{E}_k = \frac{1}{2}\int_a v^2\rho t_0 da = \frac{\omega^2\rho t_0}{2}\int_a \tilde{w}(x, y)^2 dxdy. \qquad (6.12)$$

The density is assumed to be constant over the whole membrane's surface $(\rho(x, y) = \rho)$.

For linear second order systems at resonance ($\omega = \omega_0$), the maximal kinetic energy (when the membrane is flat) is equal to the maximal potential energy $\hat{E}_{pot}$ (when the membrane is at its maximal deflection) [93], which can be written:

$$\hat{E}_{pot,drum} = \frac{\omega_{0,drum}^2\rho t_0}{2}\int_a \tilde{w}(x, y)^2 dxdy \qquad (6.13)$$

$$\hat{E}_{pot,plate} = \frac{\omega_{0,plate}^2\rho t_0}{2}\int_a \tilde{w}(x, y)^2 dxdy \qquad (6.14)$$

$$\hat{E}_{pot,tot} = \frac{\omega_{0,tot}^2\rho t_0}{2}\int_a \tilde{w}(x, y)^2 dxdy. \qquad (6.15)$$

The total maximal potential energy is the addition of the plate and drum modes. With the help of the previous equations, and assuming that the mode shape $\tilde{w}(x, y)$ is identical for the plate and drum contributions, one can write:

$$\hat{E}_{pot,tot} = \hat{E}_{pot,drum} + \hat{E}_{pot,plate} \Rightarrow \omega_{0,tot}^2 = \omega_{0,drum}^2 + \omega_{0,plate}^2. \qquad (6.16)$$

The total resonance pulsation (and therefore frequency) is equal to the square root of the sum of the pulsation of each mode squared. Introducing the resonance frequencies of the drum and plate modes (equations 6.8 and 6.9) leads to:

$$f_0 = \frac{1}{r\sqrt{\rho}}\sqrt{0.147 \cdot \sigma_p + \frac{2.634 \cdot t_0 Y}{12 \cdot r^2(1 - \nu)}}, \qquad (6.17)$$

where f_0 is the first mode resonance frequency of the PDMS circular diaphragms. The voltage dependence of the resonance frequency is obtained by combining equations 6.6 and 6.17:

$$f_0 = \frac{1}{r\sqrt{\rho}}\sqrt{0.147 \cdot \left(\sigma_0 - \frac{\epsilon_0\epsilon_r V^2}{t_0^2}\right) + \frac{2.634 \cdot t_0 Y}{12 \cdot r^2(1 - \nu)}}. \qquad (6.18)$$

Table 6.1: *Thickness of the PDMS membrane obtained by two different methods: optical measurement on a mechanically scratched zone and calculated from resonance frequency as a function of applied voltage. The mechanical parameters Y and σ_0 obtained from a bulge test measurement are also given for the two different thicknesses.*

	t_0 (μm)	σ_0 (kPa)	Y (MPa)
Scratching	28.6	43.4	2.60
Resonance	29.24	40.1	2.52

The resonance frequency depends on both the Young's modulus of the membrane and its residual stress. Resonance frequency measurements in the absence of an electric field were used to verify the values of Y and σ_0 obtained by bulge test. But resonance frequency measurements become even more interesting when a voltage is applied to a PDMS membrane with electrodes. Indeed, it is possible to rewrite equation 6.18 as:

$$f_0(V)^2 = \frac{1}{r^2\rho}\left(0.147 \cdot \sigma_0 + \frac{2.634 \cdot t_0 Y}{12 \cdot r^2(1-\nu)}\right) - \frac{\epsilon_0 \epsilon_r}{r^2 \rho t_0^2}V^2 = c_0 + c_2 V^2. \quad (6.19)$$

The resonance frequency squared is linked to the applied voltage by a quadratic law, which has a coefficient of degree 0 (c_0) and a coefficient of degree 2 (c_2). It can be observed that c_2 does not depend on the mechanical parameters Y and σ_0. And if one assumes that the density ρ and the relative permittivity ϵ_r of the PDMS used to make the membrane are known, then c_2 can be used to determine the membrane's thickness. As it was exposed in subsection 5.3.2, measuring the thickness of PDMS membranes is not easy, and a precise thickness determination is important to obtain precise mechanical parameters values from bulge test measurements. Resonance frequency measurements can therefore be made for several voltage values, from 0 up to the buckling voltage, and the membrane's thickness can be determined from the degree 2 coefficient of a quadratic fit on the $f_0(V)^2$ measurement data. This thickness value can then be used to calculate the Young's modulus and residual stress values from a bulge test made on the same membrane. This allows to obtain a better accuracy on the mechanical parameters, but can only be made on complete DEAs with two electrodes, and not on non-implanted membranes, or membranes with implantation made on a single side, such as those used to quantify the stiffening impact of implantation with bulge test measurements (cf subsection 5.3.4).

For example, the mechanical parameters of a ⌀2 mm actuator made with Sylgard 186 cured at room temperature were measured by a bulge test. To extract Y and σ_0 from the bulge test measurement, the thickness of the PDMS was measured by scratching the PDMS on a small zone to expose the Si chip on which it is bonded. Then the height of the step was recorded with a white light interferometer. The first mode resonance frequency of the membrane was measured with a laser Doppler vibrometer (*MSV400* from *Polytec*[1]). The excitation signal was soundwaves which were generated by a loudspeaker located below the membrane. Using the thickness value obtained by scratching and
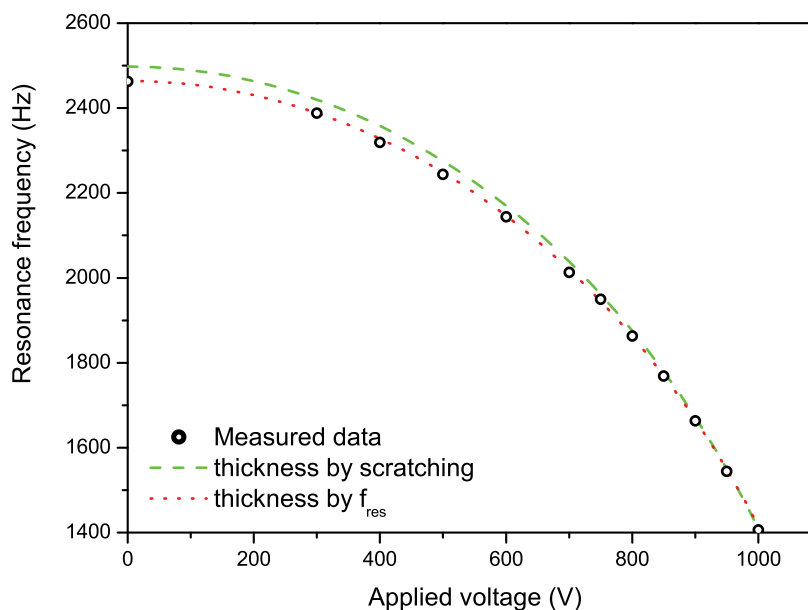
---

[1] www.polytec.com

Figure 6.7: *Measured first mode resonance frequency versus applied voltage on a ∅2 mm actuator (circles), and theoretical law calculated with the thickness obtained by scratching (dashed line) and with the corrected thickness obtained from the resonance frequency datapoints (dotted line).*

the mechanical parameters from the bulge test (table 6.1), the theoretical resonance frequencies for different voltages were calculated (equation 6.18) and compared with the measured data (Figure 6.7, circles and dashed line). The density was taken equal to 1.12 g/cm^3, and the relative permittivity to 3, according to the manufacturer's indications. The graph shows that we get a somewhat good fit between the theory and the measured data, with a 34 Hz difference at zero volt. As the difference between the theory and the data is not constant with the voltage (it tends to decrease for increasing voltages), it is the sign that the thickness measured by scratching is not accurate. Equation 6.19 was then fitted on the frequency measurement data to extract the thickness of the membrane out of coefficient c_2. This new thickness value was then used to correct the Young's modulus and residual stress obtained by the bulge test (table 6.1). Using these new values, the theoretical resonance frequency was re-calculated (Figure 6.7, dotted line). The new theoretical curve fits the data point much better, and it can be concluded that the thickness obtained from resonance frequency measurements is more accurate than the one obtained by scratching. Furthermore, it allows to determine the thickness of a PDMS layer without physically damaging it by scratching. However, as mentioned above, this technique can only be used on actuators, and not on non-implanted membranes.

For diaphragm actuators that produce out-of-plane motion, the prebuckling voltage range should be kept as small as possible, principally by fabricating suspended PDMS membranes with the lowest possible stress. It is however
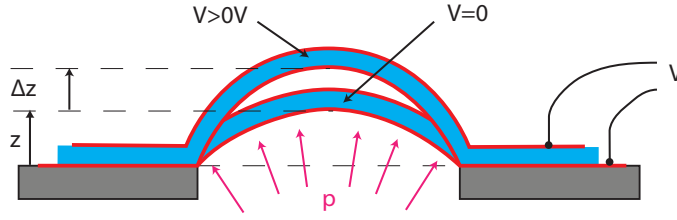
Figure 6.8: *Diaphragm DEA under a uniform distributed load (pressure): without applied voltage, the membrane is deformed in a spherical cap and its center moves to a position z. When a voltage is applied between the electrodes, the tensile stress (which is composed of the residual stress plus the deformation induced stress) is reduced by the electrostatic pressure, and the equilibrium position is shifted to $z + \Delta z$.*

possible to intentionally expand the pre-buckling voltage range by increasing the stress in the membranes, as well as by using small diameter membranes. This allows to make suspended membranes whose resonance frequency can be tuned on large frequency range, and can have application in the fabrication of tunable acoustic filters or for active damping of devices resonating in the kHz range [94].

6.2.3 Postbuckling behavior

The interesting voltage range for our diaphragm actuators is observed for $V_b < V < V_{bd}$, where indices b and bd respectively refer to buckling and breakdown. It is indeed in this voltage interval that out-of-plane motion is observed. As mentioned in the previous subsection, vertical motion will only be observed if $V_b < V_{bd}$. This was a major issue on our first Si-chip devices which were made with oven-cured PDMS (i.e. large residual stress, high buckling voltage, and low breakdown voltage (cf. section 4.7)). Most of these devices failed before any observable vertical motion.

The equilibrium vertical deflection z of the center of the membrane can theoretically be calculated with a similar reasoning than the one made to calculate the elastic stability limit. Assuming a deformation shape for the membrane, the bending energy can be calculated, as well as the potential mechanical energy induced by the electrostatic field as a function of the height of the membrane's center. The equilibrium position is the value of z for which the sum of the two energies is minimized. However, taking the bending energy as the unique contributor to the deformation is only acceptable for very small deformations relative to the membrane's thickness, when the stretching of the deformed membrane can be neglected. This procedure is considered valid for $z < t_0/2$ [91]. As vertical displacement which are much larger than the membrane's thickness are expected, we are in a stretching-dominated situation where bending can be completely neglected.

Because bending can be neglected, the fact that the boundary of the membrane is clamped only has a weak influence, appart from fixing the vertical displacement of the membrane's periphery to 0. The situation becomes therefore very similar to the one described for the bulge test and its spherical cap
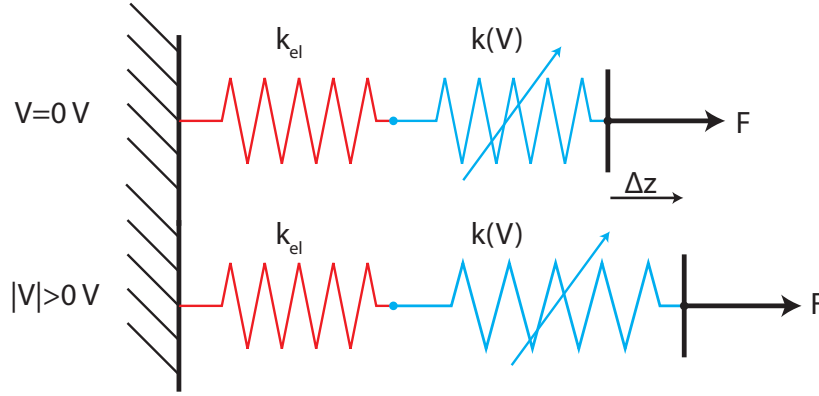
Figure 6.9: *Spring analogy of the loaded membrane. The stiffness of the right spring is reduced by applying a voltage, which causes a shift of the equilibrium point.*

deformation (cf. subsection 5.3.2). This similarity allows to add the voltage-induced stress in the pressure-deflection model developed for the bulge test, which can then describe the equilibrium position of a mechanically unloaded actuator (when the applied pressure is null), as well as the equilibrium position of actuators submitted to a uniform distributed force. If a membrane is submitted to a pressure p on one of its sides, it will deform, and its center will move vertically to the equilibrium position z, described by the bulge test equation (equation 5.16). The deformed membrane is under tensile stress σ which is the sum of the residual tensile stress, and the deformation-induced stress (equation 5.10). If an electrostatic field is applied on this equilibrated membrane, the in-plane stress will be reduced by the electrostatic pressure, and the equilibrium position z will be increased by the voltage-induced displacement Δz (Figure 6.8). The diaphragm DEA can be represented by two springs connected in series (Figure 6.9). The first one, with a fixed stiffness represents the elastic behavior of the membrane, and the second one has a voltage-variable stiffness and represents the internal stress (residual plus electrostatic pressure). Upon application of a voltage, the stiffness of the second spring is reduced, and the equilibrium position moves (Δz).

To take into account the reduction of tensile stress upon application of a voltage, equation 5.10 can be modified and a third term – the electrostatic pressure – can be added to the residual and stretching-induced stresses:

$$\sigma = s(1 - 0.24\nu)\frac{Y}{1-\nu} + \sigma_0 - \epsilon_0\epsilon_r\left(\frac{V}{t}\right)^2. \qquad (6.20)$$

The thickness t of the membrane is not equal to the initial thickness t_0 in the case of the deformed membrane. As a spherical cap shape is assumed, equation 5.8 can be used to calculate the thickness as a function of the initial thickness, the membrane's radius and the vertical deflection of the membrane's center. The previous equation can therefore be re-written as:

$$\sigma = s(1 - 0.24\nu)\frac{Y}{1-\nu} + \sigma_0 - \epsilon_0\epsilon_r\left[\frac{V(r^2 + z^2)}{t_0 r^2}\right]^2. \qquad (6.21)$$
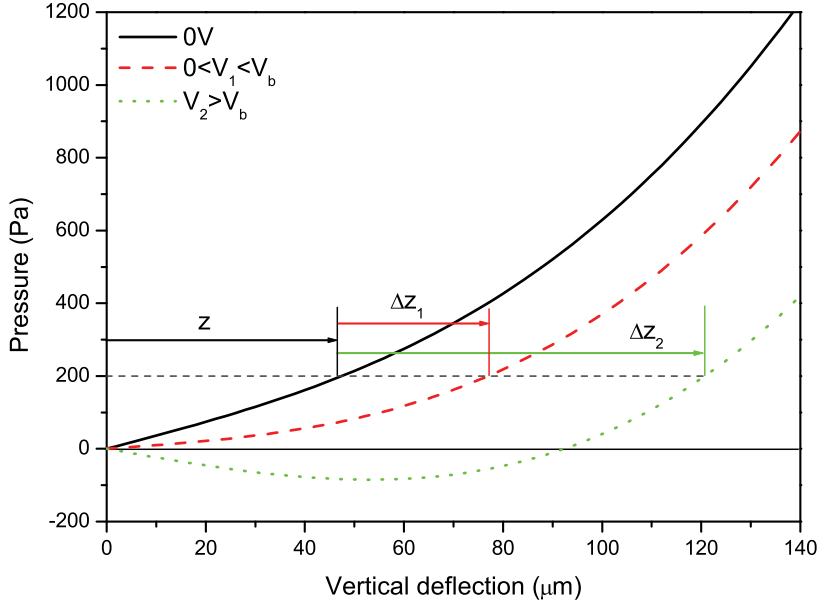
Figure 6.10: *Calculated pressure-deflection characteristics of a ⌀2 mm 30 μm-thick membrane with a Young's modulus of 2 MPa and a stress of 30 kPa for three different voltage values: 0V, smaller than the buckling voltage, and higher than the buckling voltage. The equilibrium positions for an applied pressure of 200 Pa are shown on the graph.*

This voltage-dependent stress value can then be combined with equations 5.9 and 5.15 to obtain the following relation, which describes the equilibrium position of a membrane submitted to voltage and distributed force (pressure):

$$p = \frac{8(1 - 0.24\nu)Y t_0 z^3}{3(1 - \nu)(r^2 + z^2)^2} + \frac{4\left[\sigma_0 - \epsilon_0\epsilon_r \left[\frac{V(r^2 + z^2)}{t_0 r^2}\right]^2\right] t_0 r^2 z}{(r^2 + z^2)^2}$$

$$p = \frac{8(1 - 0.24\nu)Y t_0}{3(1 - \nu)(r^2 + z^2)^2} z^3 + \frac{4\sigma_0 t_0 r^2}{(r^2 + z^2)^2} z - \frac{4\epsilon_0\epsilon_r V^2}{t_0 r^2} z \qquad (6.22)$$

This equation has two special cases: When the applied voltage is zero, it is the bulge test equation that describes the equilibrium position of a membrane of given geometrical and mechanical parameters submitted to a uniform distributed force. And when the applied pressure is zero, the model describes the unloaded displacement behavior of the membrane.

Figure 6.10 illustrates the application of the deflection model for a ⌀2 mm 30 μm-thick membrane with a Young's modulus of 2 MPa. The solid curve shows the pressure-deflection characteristic in the absence of an applied voltage. This is therefore the bulge test curve, from which the mechanical parameters Y and σ_0 can be calculated. For a given pressure (200 Pa in this example), the membrane's center reaches the equilibrium position z. The dashed curve shows the same characteristic in the case of an applied voltage smaller than the buckling voltage. The smaller slope at the origin indicates that the electro-

static pressure has reduced the stress in the membrane, but the slope having
remained positive, the residual stress at 0 deformation is still tensile. One can
easily see that the voltage is below the buckling voltage: for 0 pressure, there
is no displacement. For the trial pressure of 200 Pa, the equilibrium position
moves from z to $z + \Delta z_1$: if a pressure is applied, there is a voltage-induced
deflection, even though the voltage is below the buckling limit. The dotted
curve represents the pressure-deflection characteristics for an applied voltage
above the buckling threshold. The slope of the curve at the origin is negative,
which indicates that the stress is now compressive when the membrane is flat.
There are three equilibrium points when there is no applied force on the mem-
brane: $z = 0$ which is the unstable flat equilibrium point, $z = z_{eq}$ which is the
stable equilibrium point visible on the graph (for this example, $z_{eq} \approx 92$ μm),
and finally, as equation 6.22 is anti-symmetric[2], $z = -z_{eq}$ which is not visible
on the graph. All the points with negative pressures (between $z = 0$ μm and
$z = 92$ μm) are unstable equilibrium points: if a small negative pressure is ap-
plied, the membrane will snap to a negative height in the portion of the graph
which is not drawn. When a pressure of 200 Pa is applied to the membrane, the
equilibrium point moves from z to $z + \Delta z_2$. As shown through this example,
the deflection model can be used to determine the vertical displacement of the
center of a membrane for any value of voltage and pressure.

The buckling voltage predicted by this model is not exactly the same than
equation 6.7, which is based on the widely accepted critical stress formula for
clamped circular membranes. Indeed the present model does not take bending
into account. Consequently, it predicts buckling as soon the residual tensile
stress is canceled by the electrostatic pressure, which is characterized by an
horizontal tangent at the origin of the pressure versus deflection curve for
$V = V_b$. The critical stress compressive stress of a $\varnothing 2$ mm 30 μm-thick
membrane with $Y = 2$ MPa is -2.93 kPa. If the membrane has a residual
tensile stress of 20 kPa, the complete model that takes bending into account
predicts buckling for a voltage of 881 V. With the model that doesn't take
bending into account, the buckling voltage is reduced to 824 V. It is however
difficult to observe a clear buckling threshold on our membranes, as initial
deformations cause motion even for voltages below the buckling limit. The
presented model is expected to be well adapted to describe the behavior of
mechanically loaded membranes, but the unloaded case is at the limit of the
hypotheses on which the model is based. The results section of this chapter
will present displacement data and compare the experimental values with those
predicted by the model (cf. section 6.4).

The analytic relation describing the deformation of a loaded circular mem-
brane (equation 6.22) gives the applied pressure corresponding to a displace-
ment z and a voltage V, i.e. $p = f(z, V)$. It would be more convenient to
isolate the displacement and express z as a function of applied voltage and
pressure: $z = f(p, V)$. However, it is not possible to analytically inverse the
model, and the equation must be numerically solved to find z, for known values
of p and V. An example of the vertical deflection obtained for different values
of applied voltage and distributed force for a $\varnothing 2$ mm 20 μm-thick membrane
with $Y = 2$ MPa, and $\sigma_0 = 20$ kPa is given on figure 6.11. The pressure is
given in terms of distributed force, which represents the pressure integrated
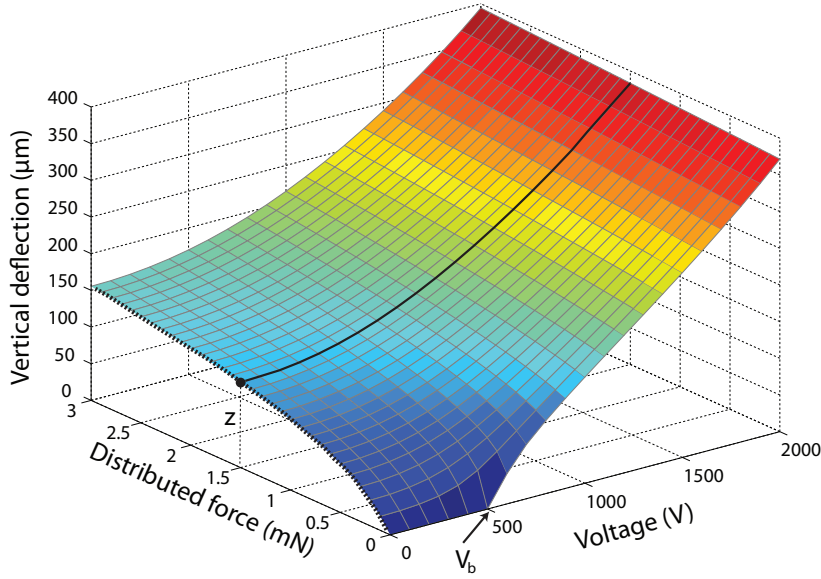
---

[2]$p(z) = -p(-z)$

Figure 6.11: *Graphical representation of the theoretical vertical displacement of a $\varnothing 2$ mm 20 μm-thick membrane with $Y = 2$ MPa, and $\sigma_0 = 20$ kPa.*

over the membrane's surface. The line obtained at 0 volt (dotted line) is the bulge test characteristic and allows to determine the mechanical parameters of the actuator. The line obtained for F=0 mN is the unloaded displacement curve. It shows a buckling voltage of 500 V, with no displacement for smaller voltages, and a displacement of 370 μm at 2000 V, which represents 18.5% of the membrane's diameter. For highly prestretched actuators, such as (but not limited to) VHB-based devices, the buckling voltage is much higher than the breakdown voltage, and they can not exhibit out-of-plane displacement in the absence of a loading force. If such a motion is desired, a mechanical biasing scheme must be used [95].

Except for the 0 pressure case, for which the vertical deflection is solely due to the electrostatic force, the displacement of all the other points of the surface is caused partly by the electrostatic action, and partly by the mechanical loading. To show only the displacement caused by the electrostatic force, the voltage-induced deflection (or Δz, as shown on figures 6.8 to 6.10) is calculated: for each point on a line at constant distributed force (for example the black line at 1.5 mN on figure 6.11), the static un-activated equilibrium position z (the black dot) is removed:

$$\Delta z(p, V) = z(p, V) - z(p, 0\,\mathrm{V}). \tag{6.23}$$

It should be noted that this way of calculating the voltage-induced deflection assumes that the mechanical load (pressure) does not vary when the membrane moves upon application of the voltage from equilibrium position z to $z + \Delta z$. This is not generally true, as in most case the bias force will decrease with the deflection of the membrane. For example, if the pressure is applied by a gas enclosed in a sealed cavity beneath the membrane, the pressure will decrease when a voltage is applied to the DEA, as the membrane's height –
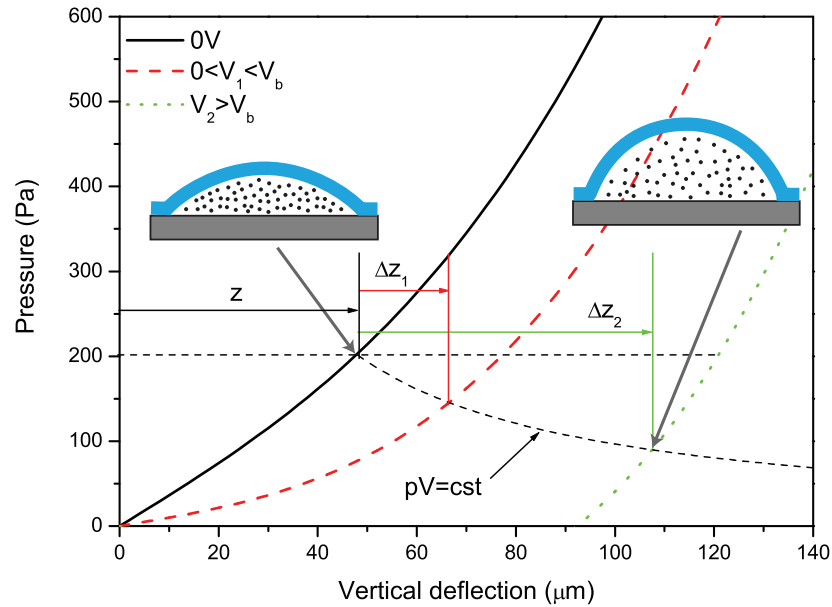
Figure 6.12: *Voltage-induced deflection for a $\varnothing 2$ mm 30 μm-thick membrane with a Young's modulus of 2 MPa and a stress of 30 kPa. To calculate the equilibrium position the number of gas molecules is assumed to be constant ($pV=cst$).*

and hence the cavity's volume – increases. Similarely to what was shown on figure 6.10, voltage-induced deflection for a $\varnothing 2$ mm 30 μm-thick membrane with a Young's modulus of 2 MPa and a stress of 30 kPa was calculated, but this time assuming a constant number of gas molecules in a closed chamber formed by the membrane, and a plate that would seal the membrane on the backside (Figure 6.12). An initial pressure of 200 Pa deforms the membrane to the equilibrium position z, and when the membrane's deformation increases, the pressure decreases, following the $p \cdot V = cst$ law, in the case of the perfect gas assumption, in the absence of a temperature change. It can be seen that the Δz values are smaller in that case, compared to the constant pressure case.

The case represented on the graph is the worst-case scenario: the volume of the spherical cap only is taken into account. In practical situations, there will most certainly be a fixed buffer volume beneath the membrane, that will reduce the volume change when the membrane deforms. If the buffer volume is much larger than the volume created below the deformed membrane, the volume change can be neglected and the pressure remains constant during the deformation. On our test setup, pressure is applied through a large (300 cm^3) buffer volume, and does not change when a voltage is applied to the tested membranes. The external force can also be applied by a spring [95], which also produce a mechanical bias which varies with the membrane deflection. However, the present model can not be applied for the spring-case, because the deflection shape is not a spherical cap in the case of a localized force.

Figure 6.13 shows the voltage-induced deflection Δz for a $\varnothing 2$ mm 20 μm-thick membrane with 3 different values of Y and σ_0, assuming that the pressure

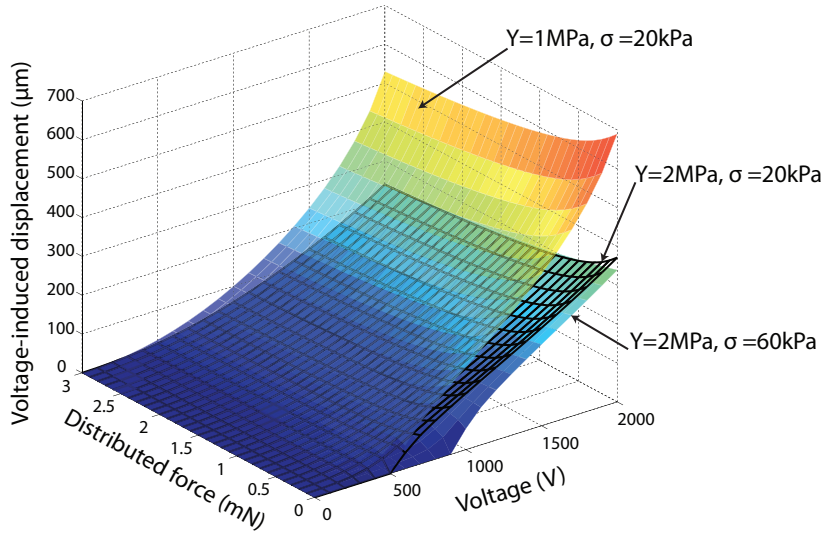**Figure 6.13:** *Voltage-induced deflection (Δz) for a $\varnothing 2$ mm 20 μm-thick membrane with 3 different values of Y and σ_0, and for different values of voltage and distributed force.*

does not change during the deformation. The first plane, with $Y = 1$ MPa and $\sigma_0 = 20$ kPa shows the voltage-induced displacement that could be expected in the case of ideal electrodes that do not change the initial Young's modulus of the PDMS. Without external applied force, the buckling voltage is predicted at 500 V. Then the deflection increases at a constant rate up to ~ 1700 V, above which the deflection rate increases, as the pull-in region is approached. Application of a mechanical load (pressure) logically decreases the voltage-induced deflection. The second plane (wireframe) represents a membrane with $Y = 2$ MPa and $\sigma_0 = 20$ kPa, which represents the typical stiffening effect of two low-dose gold electrodes. The membrane has the same mechanical parameters than the one used in figure 6.11, from which the wireframe plane can be directly calculated. The higher Young's modulus has no effect on the buckling voltage, which remains at 500 V, but the postbuckling displacement is greatly reduced, which shows the importance of minimizing the stiffening impact of the ion implantation on the PDMS membranes: at 2000 V, the unloaded displacement is 1.85 times lower for the stiffer membrane. Finally, the third plane represents an implanted membrane with $Y = 2$ MPa and with a stress of 60 kPa, which could for example build-up in the membrane if the PDMS is cured at high temperature. The high stress level increases the buckling voltage up to 900 V, which means that higher voltages need to be used to move the actuator. However, for non-null applied forces, or higher voltages, the plane converges with the previous one. Therefore, large displacement can also be obtained with high stress levels, but this necessitates to work at higher electrical field, and is therefore more prone to cause a failure of the device. These three planes show the importance to keep the stiffening of the membranes, as well as their residual stress, as low as possible.

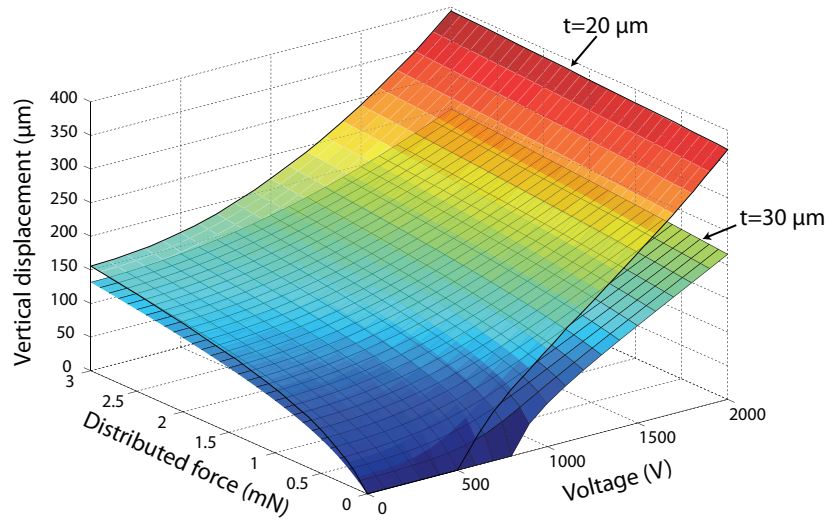The membrane's thickness also has an important influence on the displace-

Figure 6.14: *Graphical representation of the theoretical vertical displacement of a* ∅2 mm *membrane with* $Y = 2$ MPa*, and* $\sigma_0 = 20$ kPa *for two different thicknesses:* 20 μm *and* 30 μm.

ment characteristic of the actuators. On the mechanical side, an increase of the thickness stiffens the membrane, which will deform less for a given applied pressure. Hence it decreases the pressure-induced equilibrium position z. Additionally, the electric field for a given voltage directly depends on the membrane's thickness: for a thicker membrane, the electrostatic force – and hence displacement – is reduced for a given voltage value. These two effects both contribute to reduce the vertical deflection $z(p, V)$ of thicker membranes, and to increase the displacement of thinner membrane, as shown on figure 6.14 for two membranes with identical parameters, but different thicknesses: 20 μm and 30 μm. On the thicker membrane, the displacement of every points is reduced. The mechanical stiffening can be seen on the bulge test line (for $V = 0$) which shows a smaller equilibrium position. The lower electric field for a given voltage is put in evidence by a higher buckling voltage and a lower displacement for $V > V_b$.

The voltage-induced deflection for these two membranes is given on figure 6.15 left for the two extremes of the applied force: 0 mN, and 3 mN. Unsurprisingly, the thicker membrane exhibit a smaller voltage-induced deflection, independently of the applied force, because the electric field (and force) is smaller for an identical voltage. Keeping the voltage as low as possible is preferable for safety and technical reasons, but from a practical point of view, comparison should rather be done as a function of applied electric field, rather than voltage (Figure 6.15). At identical Electric field, the situation is different: without any applied external force, the electrostatic-force-induced deflection is independent of thickness. When an external force is applied to the membrane, the thicker membrane exhibit a higher Δz. This is due to the fact that thicker membranes are stiffer, and their deflection is less reduced when a distributed force is applied on them.

When the membrane is loaded with a distributed force and actuated, it
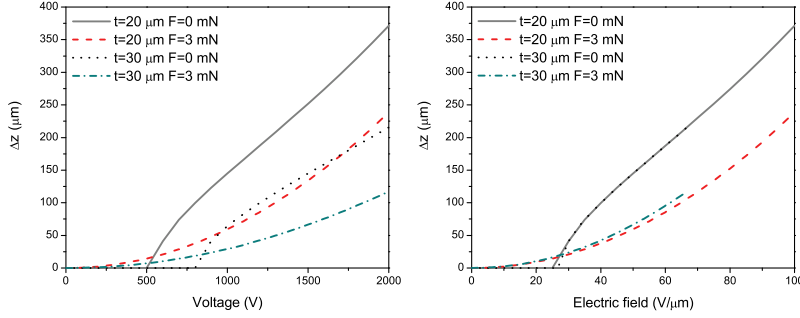
Figure 6.15: *Left: Voltage-induced deflection (Δz) for the 20 μm and 30 μm membranes for two different applied distributed forces: 0 mN and 3 mN. Right: Electric field-induced deflection for the same membranes under the same loading conditions.*

produces a mechanical work, as it moves a load on a certain distance. The deflection model can be used to calculate the expected mechanical work. As the membrane's displacement depends on the position of each surface elements of the membrane ($z = z(p, V, \rho, \theta)^3$), the work W must be calculated by integrating the displacement of each point over the whole membrane's surface:

$$W(p, V) = \int_{\theta=0}^{2\pi} \int_{\rho=0}^{r} \rho \int_{z=z(p,0V,\rho,\theta)}^{z(p,V,\rho,\theta)} p(z) dz d\rho d\theta \qquad (6.24)$$

The integration limits along z depends on the position of the surface element. In the case of deformation into a spherical cap the equation describing the displacement is given by:

$$z(p, V, \rho, \theta) = z_{max}(p, V) + \left(\sqrt{R^2 - \rho^2} - R \right), \qquad (6.25)$$

where z_{max} is the pressure- and voltage-dependant displacement of the membrane's center, as given by the model, and R is the radius of the spherical cap (equation 5.7).

In the case of a pressure that does not depend on the membrane's deformation (i.e. large buffer volume), the work equation can be simplified as follows:

$$W(p, V) = p \int_{v_0}^{v_0+\Delta v} dv, \qquad (6.26)$$

where v is the volume of the cavity formed by the membrane. In the case of a spherical cap oh height z:

$$v(z) = \frac{\pi z(3r^2 + z^2)}{6} \Rightarrow dv = \frac{\pi(r^2 + z^2)}{2} dz. \qquad (6.27)$$

Equation 6.26 can consequently be rewritten as a function of the displacement of the membrane's center:

$$W(p, V) = p \int_{z_0}^{z_0+\Delta z} \frac{\pi(r^2 + z^2)}{2} dz$$

---

^{3}the previous considerations on $z = z(p, V)$ were a particular case for the center of the membrane, when polar coordinates ρ and θ are both equal to zero
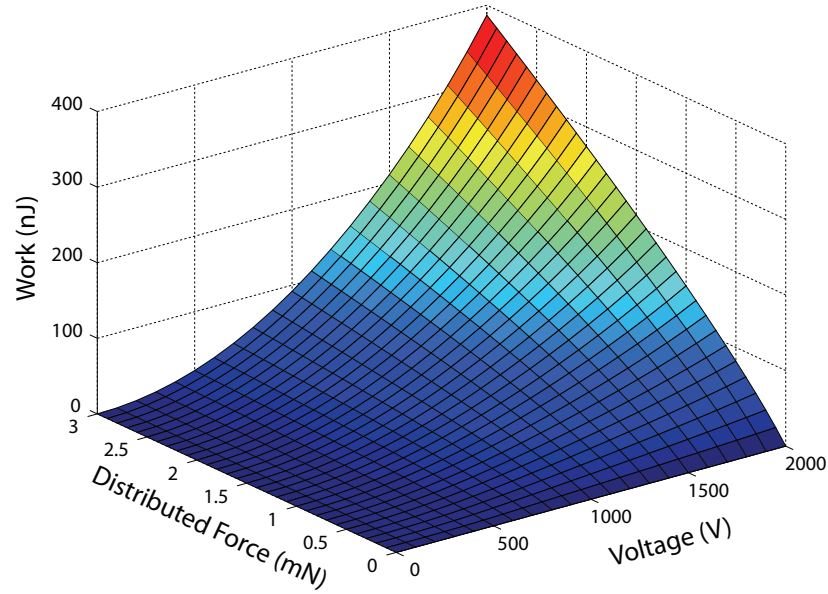
Figure 6.16: *Theoretical work for a ∅2 mm 20 μm-thick membrane with $Y = 2$ MPa, and $\sigma_0 = 20$ kPa.*

$$W(p, V) \quad = \quad p\frac{\pi \Delta z(\Delta z^2 + 3\Delta z \cdot z_0 + 3(r^2 + z_0^2))}{6}, \qquad (6.28)$$

where $z_0 = z_0(p)$ is the equilibrium position of the membrane's center when a pressure p is applied, and $\Delta z = \Delta z(p, V)$ is the voltage-induced displacement for given values of voltage and pressure. Figure 6.16 shows the graphical representation of the theoretical mechanical work (equation 6.28) for a ∅2 mm 20 μm-thick membrane with $Y = 2$ MPa and $\sigma_0 = 20$ kPa when the voltage is stepped from 0 V to a given voltage. It can be seen that the mechanical work increases when the external applied force increases, because the smallest displacements induced by the applied force is less important compared to the force increase. The model does not predict an optimum force above which the mechanical work decreases, because for large applied distributed forces the theoretical voltage-induced displacement tends to a constant value for a given voltage value. Hence the work is expected to increase linearly with the applied force. This is not a realistic behavior and it draws the attention on the limits of validity of the model, which will be discussed in the next paragraph.

The model that was introduced in this document has the advantage of being simple and easy to apply, but it is necessary to investigate the limits of its validity. There are two main limitations: geometrical and mechanical. The geometrical limitations concern the approximations that were made to derive the equations. The arclength of the spherical cap is calculated by replacing the arcsin function by the two first terms of its series development (equation 5.15). This approximation was used for the bulge test, for which displacements were limited to 10%-15% of the membrane's diameter. In the case of the actuator this displacement can be much higher, as one expects unloaded displacements over diameter ratios up to 20%. When an external force, is added, the displacement

can be furthered increased, up to the membrane's rupture for large forces. For $z/2r$ of 20% the relative error of the polynomial approximation compared to the complete formulation is -0.3%. For deformation ratios $z/r = 1$ (half-sphere), this error increases to -6.1%. For large deformations, the full formulation for the arclength should be used (equation 5.12). Deformations larger than the half-sphere are possible without breaking the membrane [83], but equation 5.12 is only valid for $z \leq r$. The complete formulation of the arclength $\forall\, 0 \leq z < \infty$ is given by:

$$
\begin{cases}
l = 2\frac{z^2+r^2}{2z} \arcsin\left(\frac{2rz}{z^2+r^2}\right) & \forall |z| \leq r \\
l = 2\frac{z^2+r^2}{2z} \left[\pi - \arcsin\left(\frac{2rz}{z^2+r^2}\right)\right] & \forall z > r.
\end{cases}
\tag{6.29}
$$

Using this formula to describe the arclength as a function of the displacement of the membrane's center z ensures a geometrically correct formulation for every possible value of z.

However, the model also has mechanical limitations. It was already discussed in the bulge test section (cf. subsection 5.3.2) that neglecting the bending energy causes the model to be inadequate for very small displacement (smaller than the membrane's thickness), which is not much of a concern for our application. The most important mechanical limitation comes from the fact that the model assumes a Young's modulus which is not strain-dependant, i.e. it assumes a perfectly linear Hookean behavior. The PDMS we use were shown to exhibit a linear behavior for compressive stretch ratios between 1 and 0.6 (Fig. 5.13). In the case of unloaded and unstressed membranes, the deformation is limited by the pull-in phenomenon, which occurs at a stretch ratio of 0.66, and the model is therefore applicable in that case. For membranes that are submitted to a distributed force, and which consequently presents a deformation without applied voltage, one must fix a limit of validity of the model. If one admits a linear strain-stress behavior up to a thickness stretch ratio of 0.5 for initially unstressed membranes, the model is applicable up to the half-sphere deformation ($z = r$), at which point the initial membrane's surface has doubled. This corresponds to very large deflection, much larger than the examples given above, and the measured data which will be presented later. However, there may be applications for which it would be useful to work with a highly deformed membrane, and the model would not be applicable for these cases. The initial stress in the membrane also plays an important role. In the case of residual stresses corresponding to a few percent strain, such as the fabrication-induced residual stress of our PDMS membranes, it has no influence. But in the case of intentionally applied prestretch of several hundred percents, the model cannot be used, as the non-linear hyperelastic behavior of the material has a dominating influence even for small deformations. It would be possible to modify the equation describing the stress in the membrane (equation 5.10) by a more complex model that would account for the hyperelastic behavior of these highly prestretched materials.

Several authors have published out-of-plane measurements of mechanically loaded membranes [95,96], but without presenting a model describing the situation. The theoretical model enables to predict the actuator's behavior before actually fabricating it. This allows to tailor the actuator's properties (size, thickness, etc.) to a desired output force and displacement.
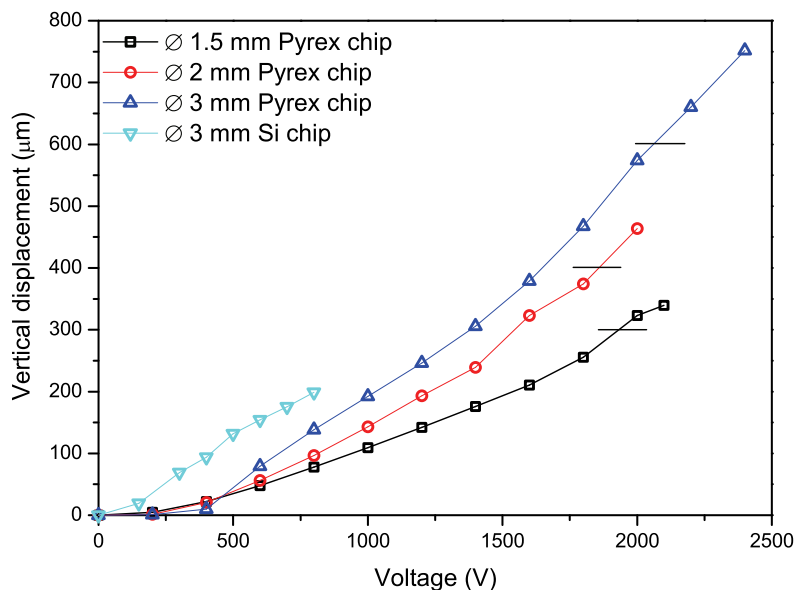
Figure 6.17: *Out of plane deflection of the membrane's center for different actuator diameters and chip material. The Si-chip actuator was tested up to dielectric breakdown, which is not the case for the Pyrex actuators. The Si-chip actuator fails at much lower electric field and exhibits a maximum displacement 4 times lower than an actuator of similar size on Pyrex. The horizontal black lines indicate a displacement over diameter ratio of 20%.*

Table 6.2: *Mechanical parameters of the four membranes used for the unloaded out-of plane deflection measurement presented on figure 6.17.*

Actuator	t_0 (μm)	Y (MPa)	σ_0 (kPa)
$\varnothing$1.5 mm Pyrex	25	2.6	11
$\varnothing$2 mm Pyrex	17.5	2.4	22
$\varnothing$3 mm Pyrex	26	2.4	11
$\varnothing$3 mm Si	22.5	0.75	17.4

6.3 Unloaded displacement

The out-of-plane deflection of circular diaphragms was measured with a white light interferometer *Wyko NT1100* (as for bulge test measurements) for different applied voltages. In accordance with the conclusions of chapter 5, Au-implantations with an acceleration potential of -2.5 kV were systematically used for the electrodes of the actuators presented in the remaining of this chapter.

Figure 6.17 shows the out-of-plane vertical deflection of actuators on Pyrex and silicon chips with 3 different diameters: 1.5, 2 and 3 millimeters. The mechanical properties of the different actuators are summarized in table 6.2. The Young's modulus and stress values of the membranes on Pyrex are ap-
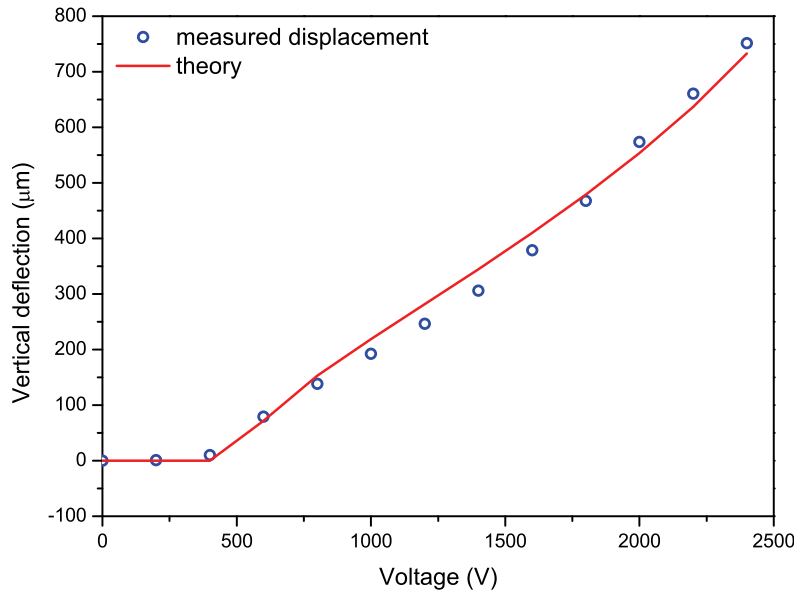
Figure 6.18: *Vertical deflection vs. voltage for the ∅3 mm Pyrex actuator, and theoretical model (eq. 6.22).*

proximate and were obtained from the datapoints. The buckling voltage was used to determine the residual stress, and the Young's modulus was chosen to obtain the best fit between the theoretical law and the datapoints (Fig. 6.18 for an example with the ∅3 mm Pyrex actuator). The mechanical parameters of Pyrex actuators can not be obtained by bulge test measurements, due to the issue of improper bonding of the implanted back electrode (cf subsection 4.7.3). The mechanical parameters of the actuator on silicon were obtained by bulge test and are therefore more accurate. The next section will study in detail the behavior of actuators made on Si chips with an applied voltage and distributed force, as well as the accuracy of the theoretical model to describe their vertical displacement. The Pyrex actuators of diameter 1.5 mm and 3 mm were made with the same PDMS layer and consequently have similar thickness and mechanical properties.

The static deflection of the actuators (Fig. 6.17) shows that vertical deflection above 20% of the membrane's diameter can be obtained for all three Pyrex actuators. In the case of the ∅3 mm device, for which a higher maximum voltage was applied, a vertical displacement over diameter ratio of 25.1% was obtained for 2400 V (92 V/μm). In contrast, the actuator of the same size but fabricated on a conducting Si chip exhibits a maximum displacement over diameter ratio of only 6.7% before dielectric breakdown, for an electric field of 36 V/μm. The maximal applied voltage on Si chip is limited due to breakdown at the electrical contact points, as explained in subsection 4.7.2.

Pimpin and coworkers have fabricated DEAs of similar sizes with evaporated gold thin-film electrodes [18, 19]. In the case of plain unpatterned electrodes, they obtained a vertical displacement/diameter of 0.5%, which is ex-

plained by the lack of compliance and very high stiffening effect of a uniform
gold film at the elastomer's surface. The most important part of their work con-
sisted in replacing the non-compliant continuous metallic thin-film by a gold
thin-film electrode patterned in concentric rings. With this technique, they
obtained displacement over diameter ratios up to 5.6%, which is 11.2 times
higher than the unpatterned electrode. As ion implanted electrodes are even
more compliant than the patterned thin-film, our actuators can produce out of
plane displacement which are 4.5 times larger.

The actuator on silicon was implanted with a much smaller dose and ex-
hibits a lower Young's modulus. This fact, combined with a thinner PDMS
layer, explains why the displacement of the actuator on Si is larger at the same
actuation voltage than that of the actuator on Pyrex of the same size. If an
implanted PDMS layer with the same properties than the ones of the actuator
on Si was bonded on a Pyrex frame, the maximum vertical deflection observed
would most certainly be even larger than our 25% record. The theoretical
maximal deflection is limited by pull-in, which occurs for a thickness stretch
ratio λ_z of 2/3 for a strain-independant Young's modulus (cf. section 2.3). The
relation between the thickness stretch ratio λ_z and the vertical displacement
over actuator diameter z/d is given by:

$$\frac{z}{d} = \frac{1}{2}\sqrt{\frac{1}{\lambda_z} - 1}. \tag{6.30}$$

For $\lambda_z = 2/3$, the theoretical maximum z/d that can be achieved is 35%. By
optimizing the parameters of the implanted layers on Pyrex chips, this limit
can probably be reached with our actuators.

As mentioned in subsection 6.2.1, the theoretical buckling voltage threshold,
which describes the voltage above which out-of-plane motion takes place, is
not often observed on our actuators, due to small initial deformations of the
membrane. Among the 4 actuators presented on figure 6.17, only the ⌀3 mm
Pyrex actuator shows a clear threshold with no displacement for voltages up
to 400 V. The three other actuators exhibit out-of plane displacement even for
small applied voltages.

The behavior of an actuation cycle was investigated by applying voltages
between 0 V and 2000 V, and then back to 0 V by steps of 200 V. The measure-
ment was carried out twice to check the repeatability of the cyclic actuation
(Fig. 6.19). The figure shows a clear buckling threshold, with no motion up to
400 V, above which the actuator starts to move downwards. As the datapoints
were taken every 200 V, the buckling voltage lies between 400 V and 600 V.
For voltages higher than 1500 V, a saturation of the deflection is observed,
which is not predicted by the theory. As this phenomenon is only observed on
downwards-deflecting membranes, it is attributed to a mechanical interaction
at large deformations between the membrane's backside and the hole's periph-
ery. When the voltage is decreased after having reached 2000 V, an hysteresis
is observed as soon as the actuator leaves the saturation zone. There is up to
a 50 μm-difference in the displacement at the same voltage for one cycle. A
good reproducibility is observed between the first and second measurement.

The low optical reflection of the PDMS membranes, coupled with the fact
that their deformed shape leads to a surface which is not perpendicular the
the light beam (except at the membrane's apex), forces us to use the higher
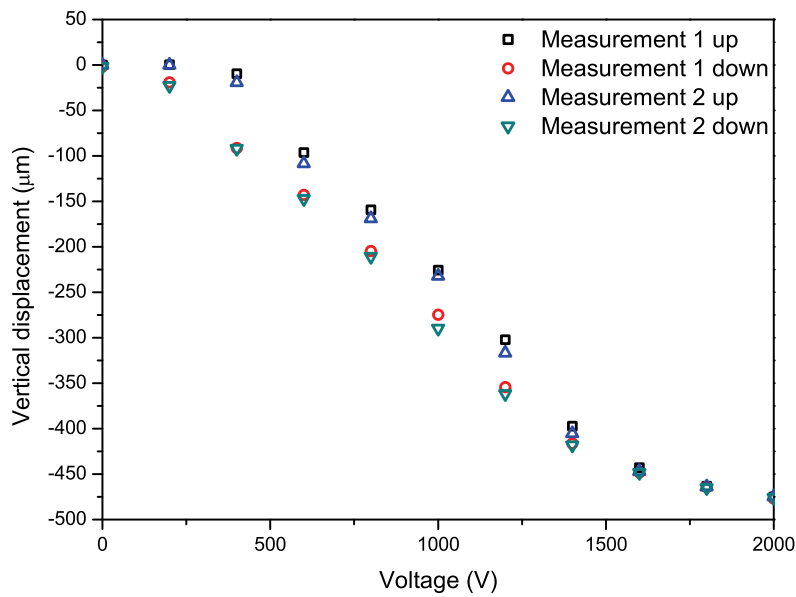magnification objective on the white light interferometer (50x, leading to a

Figure 6.19: *Vertical deflection of a ⌀2 mm actuator on Pyrex for two cycle measurement up to 2000 V and back to 0 V. This actuator was moving downwards. The buckling threshold is well visible and occurs between 400 V and 600 V. A saturation is also observed for voltages above 1500 V.*
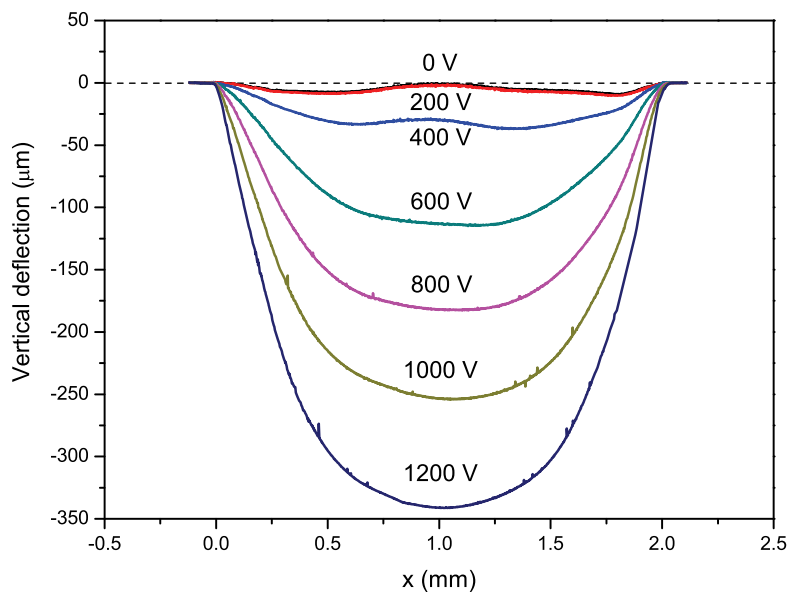

Figure 6.20: *Cross-section of a ⌀2 mm downwards-moving membrane for different voltage values. The cross-section shows the initial un-flatness of the membrane, which promotes downwards motion.*

Figure 6.21: *Left: picture of a ⌀3 mm actuator without applied voltage. Right: picture of the same actuator at 1800 V. For high applied voltages, the deformed shape diverges from the spherical cap, and exhibits a complex shape.*

field of view of 245×183 μm^2). Consequently, only a small portion of the topography can be recorded. To characterize the vertical deflection of the membranes, the objective is located at their center, and one can therefore only determine the maximal deflection of the membrane at a given voltage, i.e. the deflection of the membrane's center (Fig. 6.17 and 6.19). However, to obtain the overall shape of an activated membrane, stitching was used to combine several measurements taken next to each other, in order to cover a line going from one side of the membrane to the other. This gives the cross-section of the deformed membrane along its diameter.

Figure 6.20 shows the cross-section for a membrane located on the same chip as the actuator used for the cyclic test. The section shows the initial membrane deformation without applied voltage, which leads to the observed downwards displacement. This wavy profile is still visible at 400 V, but for higher voltages, the membrane snaps into a spherical cap shape. It was not possible to record the membrane's 2D profile for voltages higher than 1200 V, as the slope of the layer near the hole's border was too high to acquire datapoints with the optical profiler, even with the highest magnification objective.

For membranes producing upward motion, which do not show any saturation of the deflection vs. voltage characteristic, larger out-of-plane deflections are observed. The membrane's deformed shape takes a complex configuration for high voltages, close to the dielectric breakdown. Instead of the expected spherical cap shape, one observes several local maxima and minima, as shown on figure 6.21. This phenomenon is attributed to inhomogeneities in the membrane's thickness, which creates zones where the electrostatic force is higher. Because there isn't any external force on the membrane, these local inhomogeneities of the electrostatic force, lead to a complex membrane shape for the minimum energy configuration. Because the force depends on the square of the electrostatic field, this behavior is more pronounced at high voltages and large deformations values (the latter contribution is due to the thickness strain). In the next section, we will see that applying a small bias force on the membrane solves the problem.

The out-of-plane deflection of 4 different ⌀2 mm actuators located on the same 20×20 mm^2 chip was measured (Fig. 6.22). The actuators on this chip presented downwards motion. The very similar displacement values observed up to the saturation region (1500 V), shows that the properties of the 4 actuators do not vary much. This means that on a single chip, the PDMS layer's
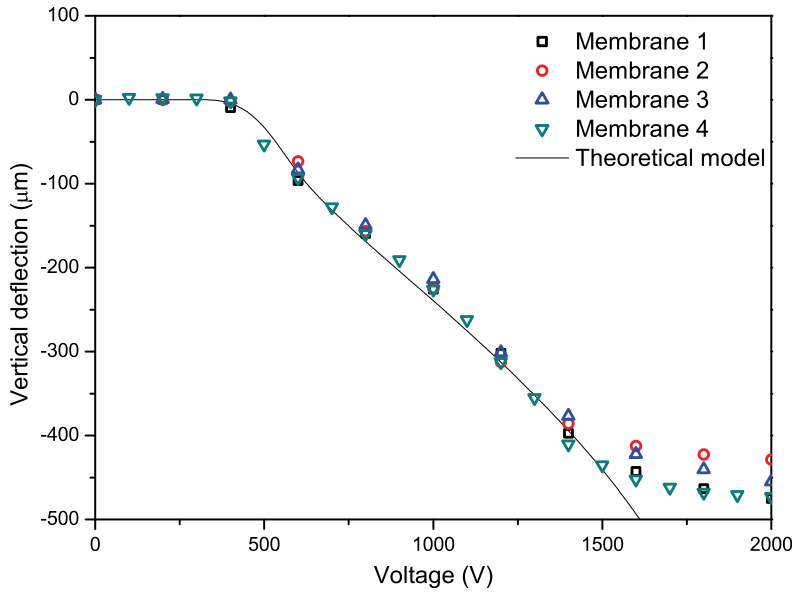
Figure 6.22: *Out-of-plane deflection of four ∅2 mm located on the same chip, as well as theoretical model for Y = 2.4 MPa, σ$_0$ = 22 kPa, and t$_0$ = 17 μm. The fact that the four chips exhibit very similar displacement vs. voltage characteristics shows that the PDMS properties as well as the impact of implantation is homogeneous on the whole chip's surface. Membrane number 4 has data points taken every 100 V, while the three other membranes have a data spacing of 200 V.*

properties (thickness, Young's modulus, stress), and the implantation (dose, stiffening impact) are very homogeneous. A theoretical displacement curve with $Y = 2.4$ MPa, $\sigma_0 = 22$ kPa, and $t_0 = 17$ μm was added to the figure and shows that the datapoints follow the theoretical model, up to the saturation point. The thickness was measured with the white light optical profiler, but the values of stress and Young's modulus are rough estimations obtained in a similar manner than the data of table 6.2.

6.4 Force–displacement characterisation

The behavior of the actuators under the action of a distributed force, and the comparison between the measured data and the theoretical model presented in subsection 6.2.3 were investigated by mounting actuators on the air-tight socket used for bulge test measurements, and by applying a pressure difference p on one side of the membrane, as well as an electric potential V between the two electrodes. The displacement of the membrane's center $z = z(V, p)$ was measured with the white light interferometer.

Because of the issues reported in subsection 4.7.3, the actuator on Pyrex could not be used for this test, which was therefore conducted with actuators on silicon, at the cost of a smaller maximal applied electric field (and hence a

Table 6.3: *Properties of the three membranes before and after implantation. Ion dose is for each electrode.*

Membrane	∅	Thickness	Before Impl.		Ion Dose	After Impl.	
			Y	σ		Y	σ
	(mm)	(μm)	(MPa)	(kPa)	(cm^{-2})	(MPa)	(kPa)
1	3.0	22.5	0.52	20.9	$1.0 \cdot 10^{16}$	0.75	17.4
2	2.0	29.2	1.07	48.3	$1.5 \cdot 10^{16}$	2.54	42.4
3	3.0	24.4	0.98	32.2	$2.0 \cdot 10^{16}$	5.57	9.8
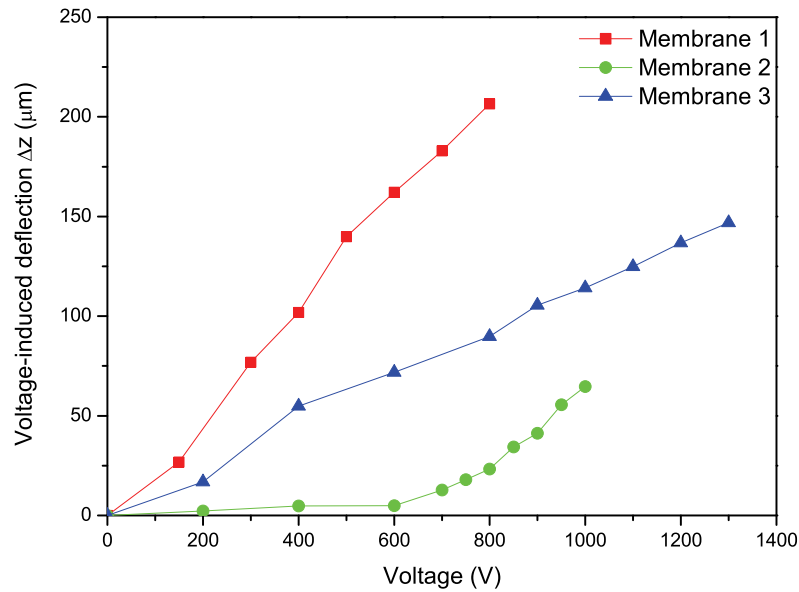
Figure 6.23: *Unloaded out-of-plane deflection for the three actuators of table 6.3. The membrane number two has a higher residual tensile stress and exhibit a high buckling voltage. Membrane 1 and 3 have the same diameter, but the lower Young's modulus of membrane 1 leads to higher displacements.*

smaller maximal displacement). Three actuators with different size, thickness, mechanical properties of the PDMS layer, and gold ion dose were fabricated. The geometrical and mechanical properties of the three actuators are given in table 6.3.

The unloaded out-of-plane displacement, similar to what was presented in the previous section, is shown on figure 6.23. It can be seen that with its higher residual tensile stress, membrane 2 presents a high buckling voltage. With its smaller diameter, it also produces smaller displacements. Membrane 1 and 3 have the same diameter, but membrane 1 has a much lower Young's modulus and therefore exhibits larger displacements.

The out-of-plane deflection measurements were then conducted with different applied pressure on the membrane's backside, up to 1000 Pa, which corresponds to a distributed force of 7 mN for the ∅3 mm membranes, and 3.1 mN for the ∅2 mm membrane. Membrane 1 is the membrane which has the
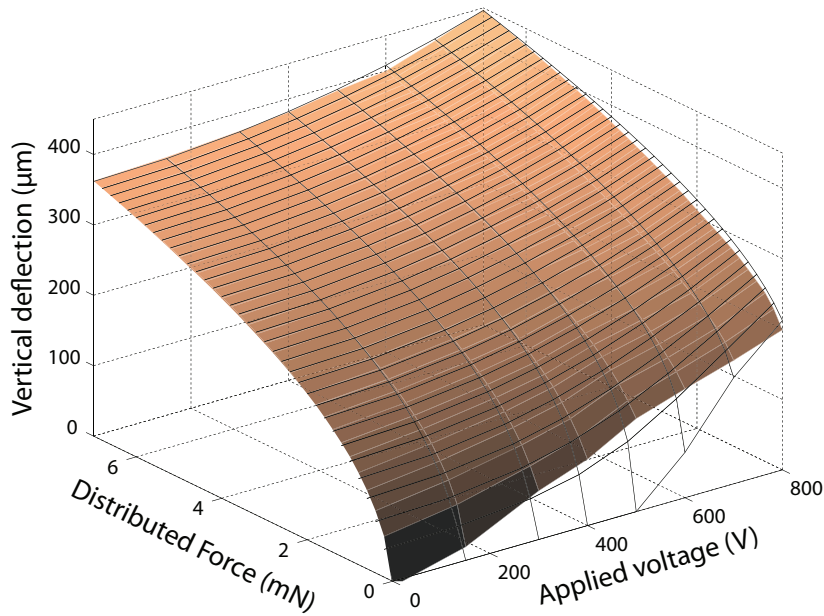
Figure 6.24: *Vertical displacement of the center of membrane 1 for voltages between* 0 V *and* 800 V *(dielectric breakdown), and applied distributed force between* 0 mN *and* 7 mN *(*0 − 1 *kPa). Wireframe: Theoretical model. Plane: datapoints.*

lowest Young's modulus, hence it is easily deformed by voltage or mechanical loading (Fig. 6.24). At the dielectric breakdown limit (800 V or 35.6 V/μm) the free-strain displacement is 207 μm which represents 6.9% of the actuator's diameter. When the maximal distributed force of 7 mN is applied, the displacement goes from 362 μm for 0 V to 448 μm for 800 V, this corresponds to a voltage-induced displacement of 86 μm (2.9% of the actuator's diameter), or a volume change of 326 nl.

The analytical model presented in subsection 6.2.3 (wireframe grid in the figure) shows an excellent agreement with the data points. The biggest discrepancy is observed for the unloaded actuator: buckling as predicted by the model is not observed in the measurement because of initial deformation of the membrane, as exposed in the above section. Furthermore, the irregular deformed shape taken by the membrane in the absence of a mechanical bias (Fig. 6.21) represents an additional cause of the discrepancy between the model and the theory. But as soon as a non-null distributed mechanical force is applied on the membrane, the analytical model is in excellent agreement with the datapoints. A picture of an actuator with a small pressure applied on the backside of the membrane shows that the small mechanical bias allows to obtain a deformed shape which is much closer to that of a spherical cap, on which the theoretical model is based (Fig. 6.25, to be compared with Fig. 6.21). The spherical cap deformation shape is conserved even with larger applied mechanical bias, as shown on figure 6.26 for a 950 Pa pressure.

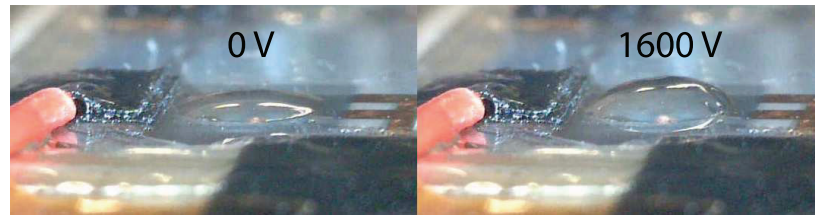The mechanical parameters used to calculate the theoretical model of figure

Figure 6.25: *Left: picture of a $\varnothing 3$ mm actuator with a pressure of 125 Pa applied on the membrane's backside, and without applied voltage. Right: picture of the same actuator at 1600 V. The small applied distributed mechanical bias allows to obtain a deformed shape much closer to the spherical cap, on which the analytical model is based.*

Figure 6.26: *Left: picture of a $\varnothing 3$ mm actuator with a pressure of 950 Pa applied on the membrane's backside, and without applied voltage. Right: picture of the same actuator at 1400 V. With a higher mechanical bias, the spherical cap deformation shape is conserved.*

6.24 were obtained by bulge test, i.e. by fitting the bulge test equation (eq. 5.16) on the datapoints obtained without any applied voltage. The thickness was measured as usual, by locally scratching the PDMS where it is bonded to the chip and measuring the step height with the white light interferometer. Then the whole wireframe grid was calculated by using the membrane's mechanical and geometrical parameters with equation 6.22.

Because the vertical deflection is due to the combined effect of the mechanical bias and of the electrostatic force, it is interesting to separate both contributions, and to calculate the voltage-induced deflection Δz, around the equilibrium position z (Fig. 6.27). Because the pressure is applied through a large buffer volume, the pressure applied on the membrane's backside doesn't change when the actuator moves, and hence using equation 6.23 is justified. Unsurprisingly, the maximum voltage-induced deflection is obtained in the absence of a mechanical force. As mentioned in the previous paragraph, at the highest tested voltage the voltage-induced displacement reaches 6.9% of the membrane's diameter. The voltage-induced displacement is reduced by the application of a mechanical load. With the highest applied force (1 kPa or 7 mN) and voltage (800 V), Δz is reduced to 2.9% of the actuator's diameter.

The mechanical work is calculated from the displacement of the actuator by applying equation 6.28. For membrane 1, the mechanical work as a function of distributed force and applied voltage is plotted on figure 6.28. The mechanical work produced by the electrostatic force is logically null in the absence of an applied voltage and mechanical force. Indeed, without voltage,
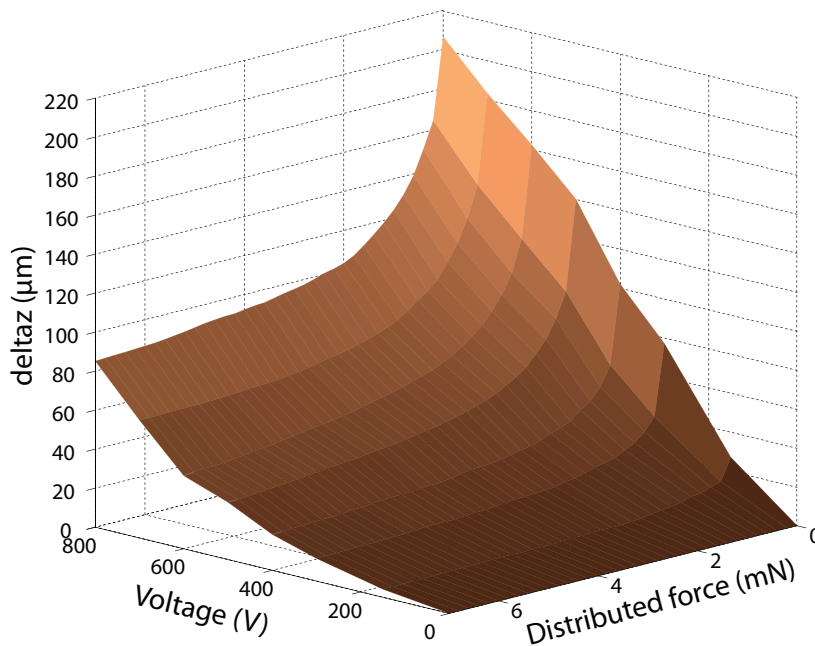
Figure 6.27: *Voltage-induced deflection (Δz) of membrane 1. At the maximum voltage (800 V) the free-strain displacement is 207 μm which represents 6.9% of the actuator's diameter. This displacement is reduced when a mechanical force is applied on the membrane. With the maximal distributed force (7 mN) and maximal voltage, Δz is reduced to 86 μm (2.9% of the actuator's diameter)*

there is no voltage-induced displacement, and without an applied force, large displacements are observed, but these do not produce a mechanical work (unloaded displacement). Consequently, the two borders of the experiment plane where $V = 0$ and $F = 0$ present a zero mechanical work, and the corner of the plane with the highest applied voltage and distributed force shows the highest mechanical work with a value of 320 nJ per cycle.

The actuators 2 and 3, with their different properties (cf. table 6.3), exhibit a different displacement characteristic compared to the first actuator (Fig. 6.29). But for the three actuators, the general observation on the displacement prediction by the theoretical model remains the same: except in the absence of an applied distributed force, where the datapoints do not follow the theoretical model for the different reasons that were exposed above, one observes that the theoretical model offers a very good description of our actuators' behavior in the region of interest.

The high residual tensile stress of membrane 2 leads to a theoretical buckling voltage which is above the dielectric breakdown of the device (1000 V). In practice, however, displacement is observed below the buckling threshold, for voltages above 600 V, which is much higher than the two other actuators. Membrane 3, with its higher ion dose, has the lowest residual stress and highest Young's modulus, in accordance with the observations of the implanta-
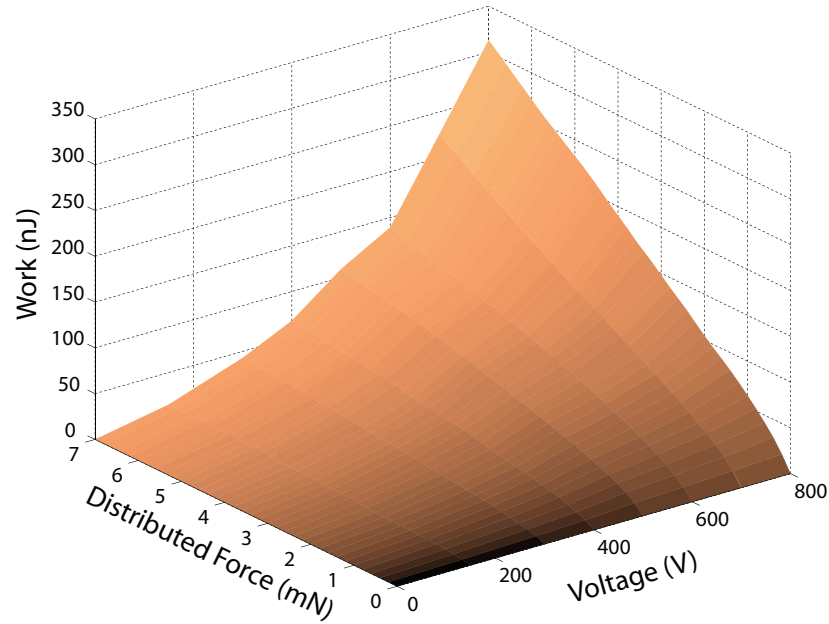
Figure 6.28: *Mechanical work of membrane 1 as a function of applied voltage and distributed force. The highest value of the mechanical work, reached with the highest applied voltage and distributed force is* 320 *nJ.*
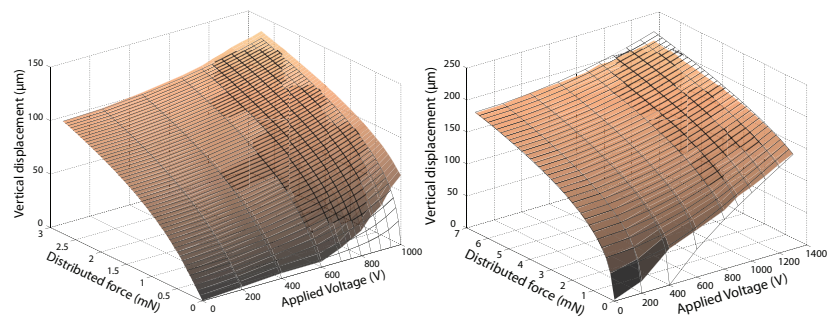

Figure 6.29: *Vertical displacement of membrane 2 (left) and 3 (right) as a function of applied voltage and distributed force. The theoretical model exhibits a good fit to the datapoint, except in the absence of applied mechanical bias (unloaded case).*
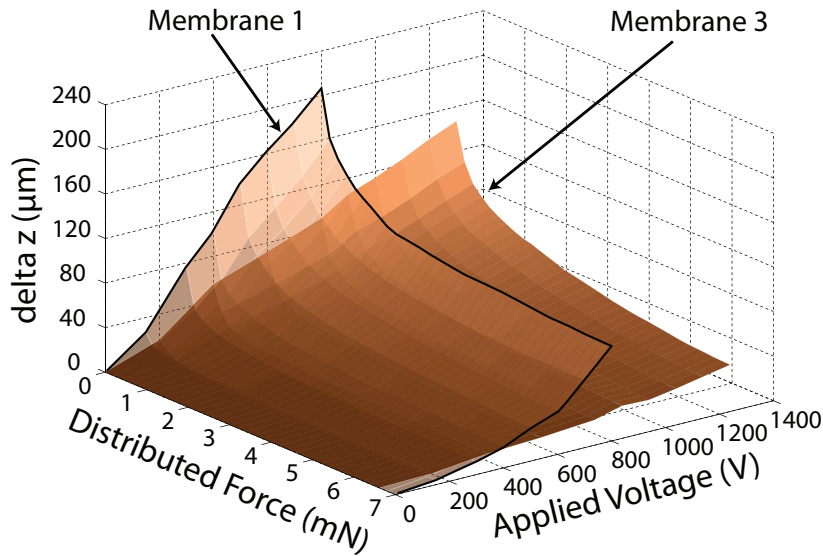
Figure 6.30: *Comparison of the voltage-induced displacement of membrane 1 and 3 (∅3 mm), as a function of applied voltage and distributed force. Due to its much higher Young's modulus, membrane 3 exhibit a much smaller vertical displacement.*

tion's impact on the mechanical properties of PDMS, investigated in subsection 5.3.4. Consequently, it shows the lowest theoretical buckling voltage, but its high Young's modulus (7.4 times higher than that of membrane 1) considerably reduces the vertical displacement of the membrane (Fig. 6.30). For the actuator 1, the unloaded voltage-induced deflection reaches 6.9% of the membrane's diameter at an electric field of 35.6 V/μm. At the same electric field, the voltage-induced deflection of membrane 3 is only half of this value. This demonstrates that reducing the residual stress with a higher implantation dose is not an interesting solution, because it causes a too important stiffening of the membrane. The best performance is obtained with membranes that have a very low internal stress before the creation of electrodes, and with the lowest possible dose which is sufficient to create a conductive surface, thus having a small impact on the membrane's Young's Modulus.

Due to its larger vertical displacement, membrane 1 is able to produce a higher mechanical work with a maximum of 320 nJ per cycle. Membrane 2, with its smaller size, produces the smallest amount of work (45 nJ max), but also occupies a smaller surface on the chip, and it is consequently difficult to compare the mechanical work of two membranes which do not have the same size. The work density (work divided by the volume of the actuator) is a better representation to compare the three different membranes (Fig 6.31). The work density is given for the 3 membranes as a function of pressure for an identical electric field. As expected, the membrane implanted with the lowest dose exhibits the best performance. Membrane 2, with its intermediate gold dose performs slightly better than the highly implanted membrane for applied pressure larger than 400 Pa. For lower pressures, the mechanical work output
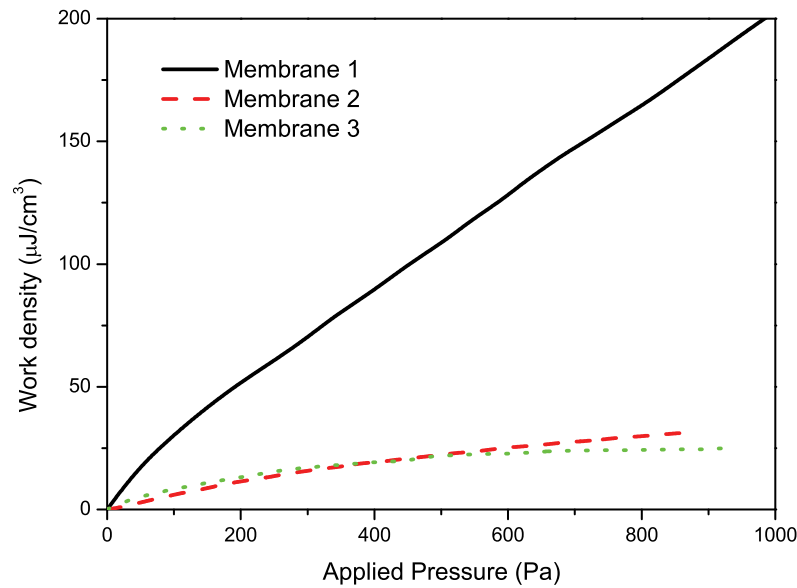
Figure 6.31: *Mechanical work density as a function of applied pressure for the three membranes for an electric field of* 35.6 V/μm. *The electrostatic energy stored in the dielectric is not taken into account.*

is limited by the relatively high buckling voltage due to the smaller size and the highest residual tensile stress.

6.5 Dynamic response

Dynamic characterization was performed by measuring the transient response to a high voltage step with a laser Doppler vibrometer (*Polytec MSV–400*). The frequency response was also measured with the laser Doppler vibrometer by applying a sinusoidal excitation signal with a DC component, in order to obtain a motion at the same frequency than the electrical input signal. Due to the limitation of our high voltage amplifier, the maximal applied voltage was $v(t) = 135 \text{ V} \cdot (1 + \sin(\omega t))$, leading to small displacement values of the actuators. All the dynamic measurements were conducted without any applied mechanical force on the membranes.

The actuators that were fabricated on silicon chips presented a broad range of response times, varying from chip to chip, between 50 ms and 500 ms. An example of an actuator's out-of-plane response to a 490 V voltage step is given on figure 6.32. The response time of the actuator was measured during the fall time only due to the impossibility to get a fast enough rising edge transition with our high voltage source. The membrane used for the measurement has mechanical properties very similar to those of membrane 1 (cf. table 6.3), but with a diameter of 2 mm. The figure shows the transient response of the membrane to a time-variant signal. The rising edge shows buckling with a rapid jump to a height of 10 μm. Then the membrane continues to move

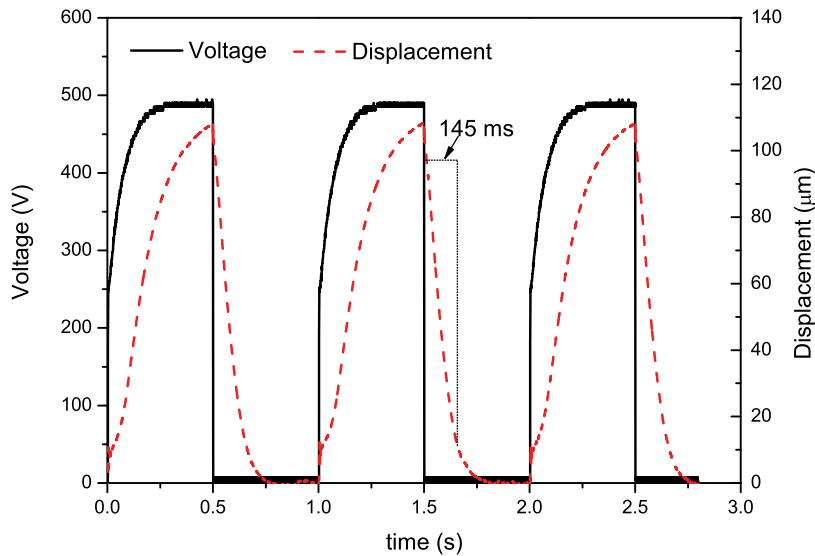**Figure 6.32:** *Dynamic response to a* 1 Hz 490 V *step signal for a* ∅3 mm *actuator on a Si chip. Measurement of the displacement of the membrane's center. The long time constant is due to a large RC product stemming from poor contact to the backside electrode.*

upward more slowly. The fall response time, defined as the time taken by the actuators to move from 90% to 10% of the full step height, is 145 ms for this actuator. This is higher than expected, given the membrane's mechanical resonance frequency of 2 kHz.

The different response speeds measured on actuators which have similar mechanical properties and implantation parameters, combined with the fact that the frequency response of the actuator is very different from the mechanical response of the membrane are indications that the actuators' response speed is electrically- (rather than mechanically-) dominated. In other words, it takes time for the electric charges to be stored on the electrodes, and the electrostatic force builds up only slowly when a voltage step is applied between the two electroded. Given the typical capacitance of the actuators ($2 - 10$ pF), having high RC values is therefore the symptom of a high series resistance. As already exposed in the fabrication chapter, fabricating the backside electrode by making a post-bonding implantation through the substrate's holes is convenient in terms of process simplicity, but leads to a very poor electrical contact between the the implanted layer and the ground electrode. This issue concerns the actuators on the Si chip (cf. subsection 4.7.1) and the actuators on Pyrex without patterned backside electrode (cf. subsection 4.7.2). For the latter, the problem is even more severe, due to the non-conducting nature of the substrate which was compensated by a metallization. The step coverage and the roughness of the laser-drilled holes can be the cause of a sub-optimal electrical contact to the implanted zone. Rise and fall time of more than 1 second were observed for this type of actuators.
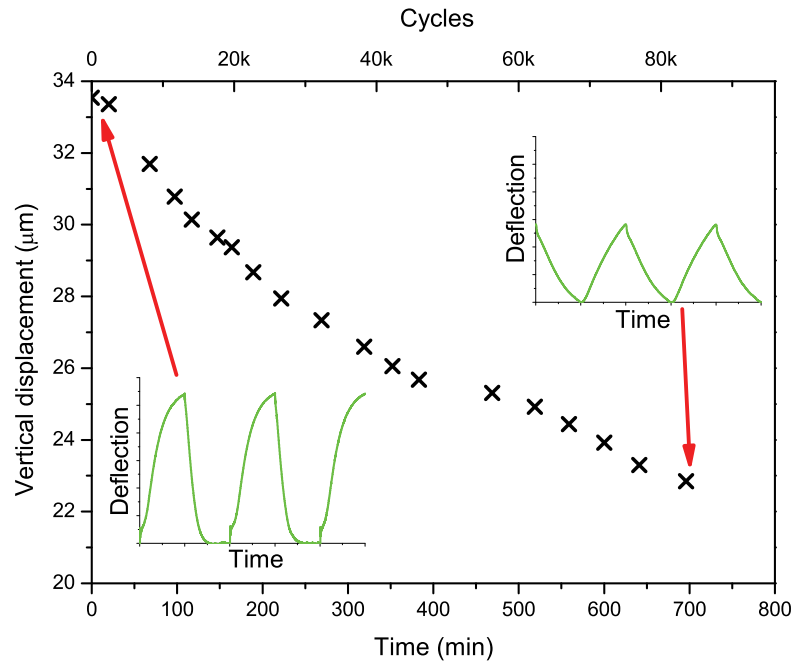
Figure 6.33: *Degradation of the deflection with the number of cycles for an actuator on Si. Starting from the initial characteristic of figure 6.32 (left inset), the deflection decreases. After 84k cycles, the new step characteristic (right inset) exhibits much higher rise and fall times.*

The initial high resistance due to the poor contact between the backside electrode and the chip/metalized zone is subject to degradation when the actuator is cyclically actuated. Starting with the characteristics presented above, the actuator of figure 6.32 was then submitted to a 2 Hz sinusoidal signal between 0 V and +270 V. The amplitude of the deflection was regularly monitored and was seen to decrease from 33.5 μm to 22.5 μm in 700 min (or 84k cycles). Then, the step response was re-measured in the same conditions (490 V step at 1 Hz) and exhibited much larger rise and fall times, larger than 500 ms, so the actuator doesn't move to the full step height before the end of the step (Fig. 6.33).

The frequency response of the actuator was also measured by applying a sinusoidal signal on a high DC voltage, as described at the beginning of the present section (Fig. 6.34). The frequency was swept from 250 mHz to 5 kHz, and it can be seen that the actuator's response is attenuated as soon as the frequency increases. At 2 kHz, the mechanical resonance peak is observed, but its amplitude is only 1/3 of the DC displacement.

The unreliable electrical contact between the actuators' backside electrode and the ground plane was solved by adding a patterned backside implantation before the bonding step, as described in subsection 4.7.3. However, this comes at the cost of a slightly more complex process flow. The new design ensures a good electrical contact between the ground pad and the backside electrode, and leads to much faster response time.
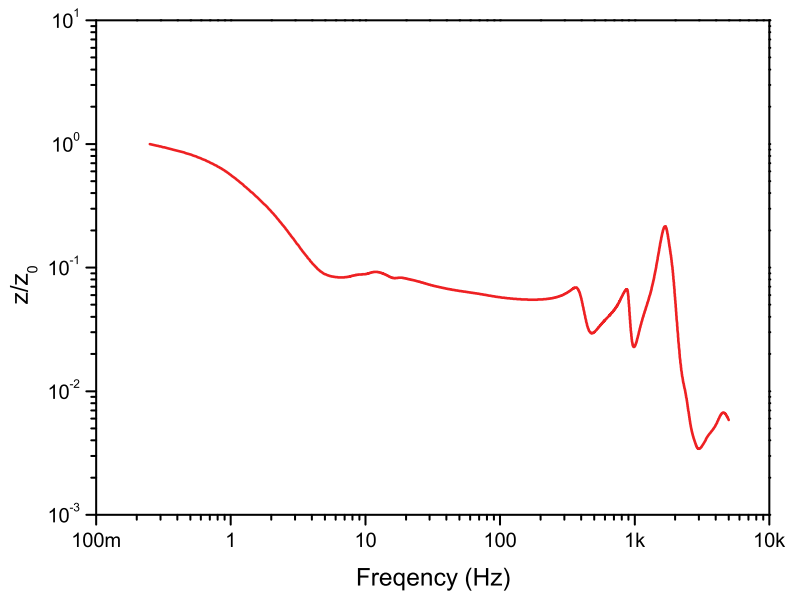
Figure 6.34: *Frequency response of the same actuator (on a Si chip) than the one used for the step response after 84k cycles. The amplitude of the deflection decreases quickly, and the resonance peak is barely visible at 2 kHz. One can see two time scale: an electrical RC time constant of the order of 1 second, and a mechanical time constant of 2 ms.*
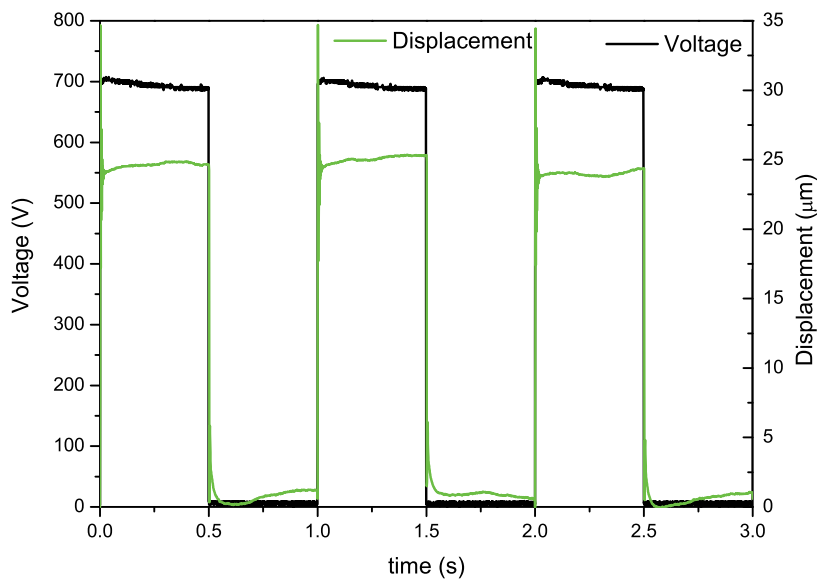

Figure 6.35: *Dynamic response to a 1 Hz 700 V step signal for a ∅2 mm actuator on a Pyrex chip with patterned backside electrode. Measurement of the displacement of the membrane's center.*
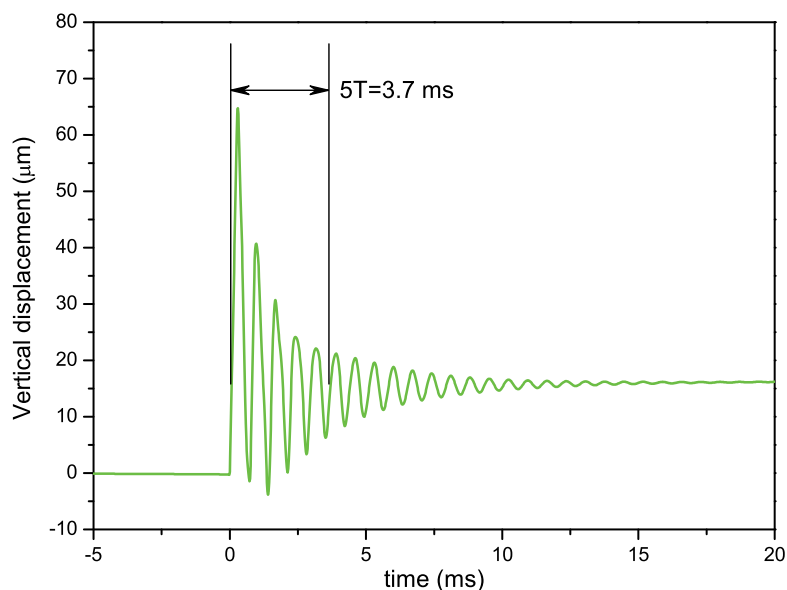
Figure 6.36: *Dynamic response to a* 700 V *electrical step signal for a* ⌀2 mm *actuator on a Pyrex chip with patterned backside electrode. A mechanically under-damped behavior is observed. The oscillations have a frequency of* 1350 Hz.

Figure 6.35 shows the mechanical response of a ⌀2 mm actuator on Pyrex with a patterned backside electrode to a 1 Hz 700 V step signal. Compared to what was observed for the actuators without patterned backside electrodes (cf. Fig. 6.32), this actuator presents a lower RC constant, leading to a much faster mechanical response to the 1 Hz square electrical signal. The sharper voltage rising edge is due to the use of a different HV source. A closer look in the step region shows that mechanical ringing takes place and the actuator behaves like a mechanically under-damped system (Fig. 6.36). The period was measured on 5 oscillations and leads to a mechanical resonance frequency of 1350 Hz. The response of the actuators with a patterned backside electrode is clearly mechanically dominated, and is limited by the mechanical ringing of the membrane. Stability of the deflection was investigated on a ⌀1.5 mm actuator submitted to a 1300 V square signal at 1 Hz. The initial actuator's peak deflection was 80 μm. This value remained unchanged after 55k cycles. After 110k cycles, the maximal deflection was reduced to 72.4 μm.

The frequency response of the same actuator clearly shows a mechanically-dominated second order behavior, with a flat response with a gain of one up to the resonance peak (Fig. 6.37). The resonance peak is clearly visible with its maximal gain of 10 and its quality factor of 7.5. The resonance peak is located at 1280 Hz, which is in good accordance with the frequency of the oscillations observed in the step response.
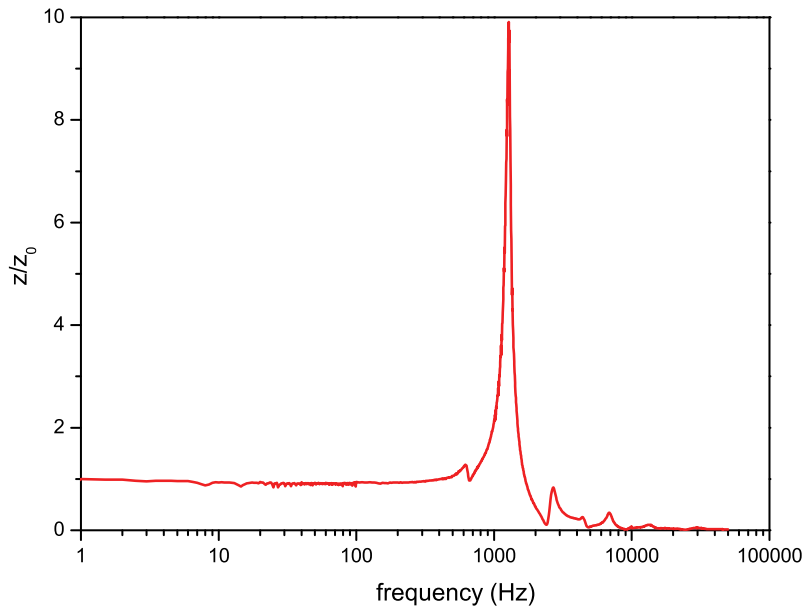
Figure 6.37: *Frequency response of the same ⌀2* mm *actuator on Pyrex with a patterned backside electrode. A perfectly flat response is observed up to the resonance peak (*1280 Hz*), which has a quality factor of 7.5*

6.6 Concluding remarks

The application of highly compliant metal ion-implanted electrodes to the fabrication of small-size circular dielectric elastomer actuators was exposed in this chapter. Three different process flows were introduced. The final process, which involves using a Pyrex chip as substrate and a patterned backside electrode, allowed to obtain static out-of-plane displacements up to 25% of the membrane's diameter, and a very fast, mechanically-limited, dynamic response time. However, this design dos not allow to reliably apply pressure on one side of the membrane, as membrane de-bonding can occur due to the absence of adhesion on the implanted zone of the PDMS. Further investigations are still needed to find the perfect design which will combine all the advantages together.

The characterization of actuators on Si chips with a distributed applied force (pressure) has been shown to be in excellent agreement with the theoretical model developed at the beginning of the present chapter. The model can be used to dimension actuators for practical applications, in order to fullfill desired requirements.

Taking a DEA with the parameters of membrane 1 (cf. table 6.2) , one can use the analytical model to calculate the performance one could expect from such an actuator if used as a micropump with hypothetical perfect inlet and outlet valves (Fig. 6.38), in a development similar to what Tews et al. did for larger actuators. [96].

Assuming an inlet pressure (P_{in}) of 600 Pa, and an actuation voltage of 800
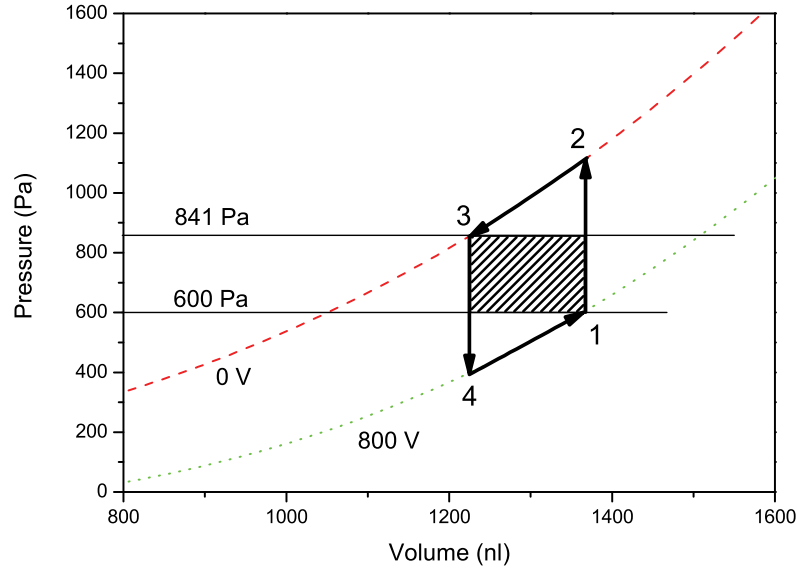
Figure 6.38: *Example of a theoretical work cycle of a DEA used as a microp-ump and actuated between* 0 *V and* 800 *V. The input pressure point is chosen at* 600 *Pa, and the output pressure is chosen to maximize the potential energy gain (hatched rectangle).*

V, the membrane's equilibrium position is represented by the point 1. If the voltage is removed, the membrane compresses the fluid and the pressure rises to point 2. The liquid can leave the chamber until the pressure decreases to the outlet pressure (P_{out}), at which time point 3 is reached. The membrane is then reactivated, which lowers the pressure in the chamber (point 4) and allows the liquid to enter the chamber to go back to the initial position. Total work done per cycle is represented by the surface enclosed by the loop and can be divided in one rectangle (hatched surface) and two triangle-like shapes. The rectangle represents the potential energy transmitted to the fluid by the pressure gain, and the triangles reflects the kinetic energy added to incoming and outgoing fluid, which is lost in most pumps designs (at least for the energy added to the fluid entering the pump). Total work is maximized if the two pressures are equal, but in that case, there is only kinetic energy created, half of which at least is lost and dissipated. Given a working point for P_{in} (378 μm, 600 Pa) on the activated curve, there is an optimal output point (z_{out}, P_{out}) which will maximize the potential energy transmitted to the fluid. This can easily be calculated by maximizing

$$E_{pot} = (vol(z_{in}) - vol(z_{out})) (p(z_{out}, 0 \text{ V}) - p(z_{in}, 800 \text{ V})), \qquad (6.31)$$

where Vol(z) is the volume of the chamber when the membrane is deformed to a height z, and p(z,V) is the equilibrium pressure for a displacement z and an applied voltage V (Eq. 6.22). By moving the input point to a lower pressure and selecting the output point to maximize the potential energy, the ratio E_{pot}/E_{kin} increases, but the value of the potential energy per cycle is

decreased. The opposite is observed if the pumping loop is moved toward higher pressure.

For this example, the optimal output height is 338.4 μm, which corresponds to an output pressure of 841 Pa, and a pumped volume of 148.3 nl per cycle. The mechanical work converted to potential energy is 35.7 nJ per cycle, the kinetic energy of the fluid leaving the pump is 19.7 nJ, and the kinetic energy dissipated by the fluid entering the pump is 15.8 nJ. The total mechanical work produced by the pump is 71.2 nJ per cycle. For an equivalent electrostatic force, the work divided by the volume of the membrane is approximately 15 times smaller than what Tews et al. obtained for the same polymer, but for a much larger diameter pump. Direct comparison is difficult, because our membranes have a thickness over surface ratio 40 times larger than those of Tews et al. However, it should be pointed out that the pressure difference has been conserved during miniaturization, and that it is the pumped volume per cycle which is greatly reduced. Furthermore, if air-tight or sealed actuators can be fabricated with the patterned backside electrode on Pyrex chip, higher voltages can be applied before breakdown, leading to larger energy output.

Another application which will be investigated at the LMTS, taking advantage of the high optical transmission of PDMS (cf. section 5.5), are tunable lenses, whose focal length can be voltage-modulated. The focal length of a lens depends on the radius of curvature of its two sides. However, because most lenses are made out of rigid materials (glass, hard polymers etc.), optical zooms are fabricated by combining optical elements that move relative to each other, leading to complex bulky systems. Dielectric elastomer actuators can be used to create lenses whose radius of curvature can be changed, hence providing a small and compact system whose focal length can be tuned on a large scale.

Figure 6.39 shows the concept of a DEA-based tunable lens. PDMS membranes are connected via a channel filled with a high-refractive-index liquid. The volume of liquid is chosen so as to inflate the membranes to an equilibrium position (Fig. 6.39 up). One of the membrane is implanted and acts as an actuator, or pump (it can also act as a lens, but the implantation decreases the transmission, as exposed in section 5.5), and the other membranes which are connected to the pump via the channel act as lenses. Several lens designs can be fabricated, such as the double lens with two PDMS membranes, and the single lens with one flat Pyrex interface, and a movable PDMS membrane. When a voltage is applied on the actuator, the equilibrium position is modified (Fig. 6.39 down). The two conditions that define the new stable position are: 1) a constant volume of the liquid, and 2) an identical pressure of the liquid under each membrane. The theoretical model can be used to calculate the different equilibrium positions and deduce the focal length of a lens as a function of voltage.

Theoretical calculations have been made to predict the focal length of a tunable lens as a function of voltage. Two different configurations were investigated: a single lens connected to a pump, and a double lens connected to a pump. The parameters for the all the PDMS membranes were taken to be identical: $r = 1$ mm, $t_0 = 20$ μm, $Y = 1$ MPa and $\sigma = 20$ kPa (Fig. 6.40). The initial pressure inside the chambers was set to 500 Pa, leading to an initial membrane height of 145.4 μm and a radius of curvature of 3.5 mm. The refraction index of the liquid was set to 1.5. The figure shows that the initial focal length of the double lens is two times smaller than that of the single lens due
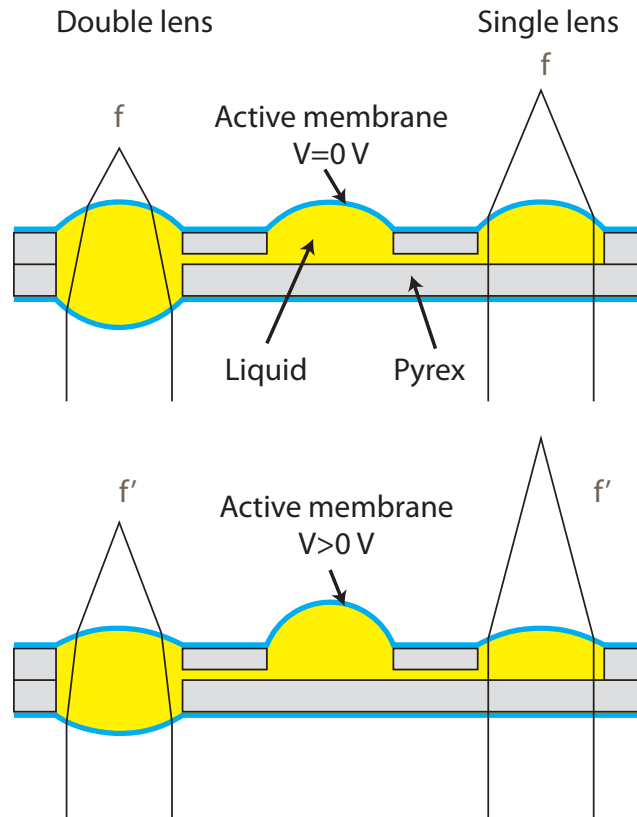
Figure 6.39: *Concept of a DEA-based tunable lens. A closed cavity filled with a liquid with a high refractive index is connected to several PDMS membranes. One of the membrane is implanted and acts as a pump. The non-implanted membranes act as lenses. An initial pressure deforms the membranes, and the application of a voltage on the active membrane changes the curvature of the lenses, and hence their focal length. Several lens types can be made, such as a double lens (left), and a single lens (right).*

to the two identically-curved interfaces. Applying a voltage on the pump leads to an increase of the lenses' radius of curvature, up to the the point at which the lens membranes are completely flat (0 pressure in the chamber), and the focal length diverges to infinity. Assuming sealed actuators on Pyrex (bonding problem solved), then voltages up to 2000 V can be applied on a 20 μm PDMS membrane. For membranes with the geometrical and mechanical parameters used for the present calculations, it can be seen on the graph that the chosen initial pressure of 500 Pa is optimal for the double lens, as the membranes reach a flat configuration around 2100 V, ensuring f-length tuning on the whole voltage range. For the single lens, however, the flat configuration is obtained for 1400 V only, thus reducing the tunable voltage range. A higher initial pressure should be used in the case of the single lens (about 1kPa for this geometry). The initial liquid pressure can therefore be used to take full advantage of the whole voltage range, but as the initial lenses' radius of curvature depends on
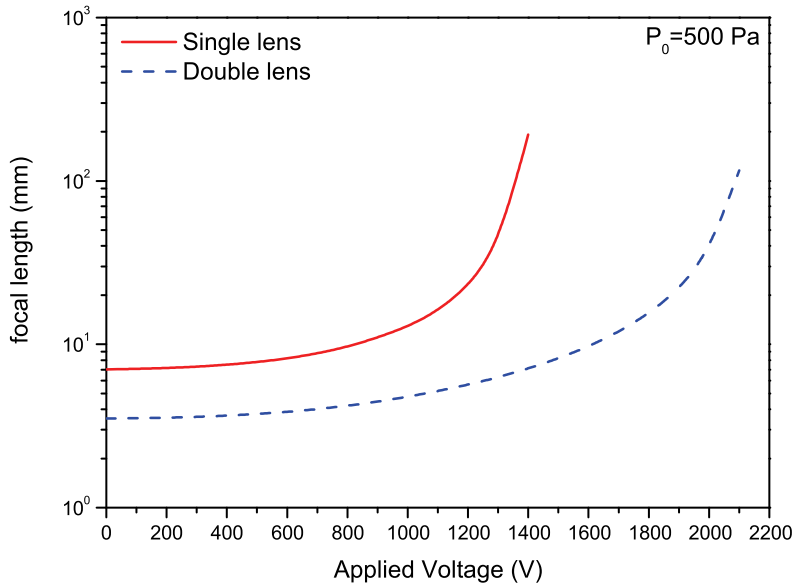
Figure 6.40: *Theoretical calculations of the focal length for a single and double lens with the following parameters: $r = 1$ mm, $t_0 = 20$ μm, $Y = 1$ MPa and $\sigma = 20$ kPa, both for the pump and the lens membrane(s).*

the initial pressure, the focal length at zero volt is also influenced by this initial pressure. Consequently, given a fixed lens diameter, the Young's modulus and thickness of the PDMS must be carefully chosen in order to achieve tuning on the whole voltage range, starting from a given initial focal length at zero volt, to reach a flat configuration before dielectric breakdown.

These two calculation examples – the pump and the lens – demonstrate how the theoretical model can be used to dimension non-prestretched circular diaphragm DEAs for precise applications. With their high response speed and large displacements, miniaturized DEAs open the door to a broad new range of applications, out of which the field of tunable optics looks particularly promising.

Part of the results and developments of this chapter were published in Sensors and Actuators A: Physical [85], in the Journal of Microelectromechanical Systems [94], and submitted to the Journal of Micromechanics and Microengineering (November 2008), as well as presented at the IEEE 21st International Conference on Micro Electro Mechanical Systems, Tucson, 2008 [97].

Chapter 7

Conclusions

This thesis has introduced the use of metal ion implantation for the fabrication of compliant electrodes for miniaturized dielectric elastomer actuators. Implantation of metal particles in an elastomer does not lead to the creation of a stiff continuous metallic layer. Instead, the implanted atoms form nanometer-size clusters that can move relative to each other while forming a conducting path, thus producing conductive layers that can be extensively stretched while remaining conductive.

Filtered cathodic vacuum arc was identified as an implantation technique which combines high ion fluxes with low energies, thus allowing to quickly implant a large number of metallic particles ($\sim 5 \cdot 10^{13}$ at/$(\mathrm{cm}^2 \cdot \mathrm{s})$) in the first 50 nm below the surface of PDMS layers. An experimental FCVA system was built in the frame of the project and was used to fabricated low-resistance PDMS layers capable of large deformations. It was shown that under certain conditions, gold implanted PDMS stripes could be obtained that combined low and time stable resistance (a few hundreds Ohm/square) with a very large uniaxial strains before loosing electrical conductivity ($> 170\%$), and a low degradation when cyclically stretched.

These compliant electrodes were successfully used to make millimeter-size dielectric elastomer actuators that exhibited out-of-plane vertical displacements up to 25% of their diameters, which is 4 times larger than reported displacements for similar actuators with patterned metallic thin-film. Far from being limited to the world of DEAs, the emergence of the use of polymers as functional materials, as well as the fabrication of electronic circuits on flexible and deformable substrates have created the need for electrodes that can be stretched, bent or deformed while remaining conductive. Metal ion implantation can be a solution for some of these applications, as it was shown to have larger strain capabilities compared to the other alternative techniques found in the literature.

Because ion implantation is a clean (as opposed to carbon-powders) technique that produces electrodes that are reliable, stable and that can be easily patterned by the use of a shadow mask or a combination of photolithography and lift-off, it opens the door to the miniaturization of DEAs, which has been lagging due to the lack of a technique to fabricate the compliant electrodes in a microfabrication-compatible manner. As DEAs' force-displacement characteristics are not easily matched by any other standard micro-actuator classes,

the field of potential applications is very wide. Tunable optical systems, which take advantage of PDMS' excellent optical properties, is a market on which small-size DEAs have a bright future.

This thesis represents only a small step in the rapidly-developing world of DEAs, but I hope that the results and ideas presented in this document will be useful for the artificial muscles community, and that metal ion implantation for DEAs will be used extensively outside the circle of our laboratory.

Acknowledgments

I want to thank my parents for their everyday support during these past 28 years. They have always encouraged me in my (mostly friendly) encounters with life's many challenges, from learning to read, up to this PhD thesis, without forgetting the tremendous task (as a child!) of dicovering and imitating their cunning strategy to win at the Cluedo, which – despite what I tell them again and again – hasn't left that much traumatized. I am also very thankfull of them for just bearing with me and my very detailed answers to their questions: "-What are you doing in the frame of your research project?" "-Things", or "Are you progressing with your project?" "-Maybe".

Although my name is the only one listed as author of this thesis, my research was conducted in the frame of a National Science Foundation project involving three other persons, whose precious help and kindness I want to acknowledge here. First, there is Prof. Herbert Shea, director of the *microsystems for space technologies laboratory*, and my thesis supervisor. Obviously, I want to thank him for taking me on board, but also for his unlimited trust and time. While some PhD students see their thesis director only once every three months, Herbert's unlimited availability greatly contributed to the results presented in this thesis. Because he had to go through my office to reach his, he could hardly escape my bottomless reserve of questions, be it on EAP-related subjects, or on the correct usage of the fax machine; and he always took time to answer, even to stupid ones. Then there is Philippe Dubois who, due to his unusual technical and academic background, is perfectly at ease at the commands of a milling machine in a workshop, as well as in the middle of the formulas of Timoshenko's demonic books on structural engineering. Our post-doc – who later became my thesis co-director to comply with EPFL's soviet-style bureaucracy – is therefore the kind of person every lab wants to have (and if possible, more than one), and his contribution to this project is beyond human imagination. To give credit where it is due, it is Philippe (together with Sander Koster of the IMT) who had the idea of ion implantation for DEAs. And finally, there is Muhamed Niklaus, my fellow PhD student on the project, who takes care of investigating the implantation's impact on the material properties of the PDMS. He has inherited of a tremendously difficult task, but has obtained very interesting results, most of them can be used to explain some of the behaviors observed in this document, such as the difference between the three tested metals. I am looking forward to reading Muhamed's upcoming publications, as I am sure that they will be of very high interest. Many of the issues I encountered during my research were solved by brainstorming sessions with these three persons, to whom I am deeply indebted.

I also want to thank my three thesis examiners, Dr. Gabor Kovacs from

Bibliography

[1] J. H. Burroughes, D. D. C. Bradley, A. R. Brown, R. N. Marks, K. Mackay, R. H. Friend, P. L. Burns, A. B. Holmes, Light-emitting diodes based on conjugated polymers, Nature 347 (6293) (1990) 539–541.

[2] R. Pelrine, R. Kornbluh, Q. Pei, J. Joseph, High-speed electrically actuated elastomers with strain greater than 100%, Science 287 (5454) (2000) 836–839.

[3] S. Ashley, Artificial muscles, Scientific American 289 (4) (2003) 52–59.

[4] Y. Bar-Cohen, Electro-active polymers: Current capabilities and challenges, in: Proceedings of SPIE - The International Society for Optical Engineering, Vol. 4695, 2002, pp. 1–7.

[5] R. E. Pelrine, R. D. Kornbluh, J. P. Joseph, Electrostriction of polymer dielectrics with compliant electrodes as a means of actuation, Sensors and Actuators, A: Physical 64 (1) (1998) 77–85.

[6] C. Loewe, X. Zhang, G. Kovacs, Dielectric elastomers in actuator technology, Adv Eng Mater 7 (5) (2005) 361–367.

[7] I. M. Ward, J. Sweeney, The Mechanical Properties of Solid Polymers, John Wiley, Chichester, 2004.

[8] G. Kovacs, P. Lochmatter, M. Wissler, An arm wrestling robot driven by dielectric elastomer actuators, Smart Materials and Structures 16 (2) (2007) s306–s317.

[9] Industry updates: Teenage girl arm wrestles robot and wins, Journal of Failure Analysis and Prevention 5 (3) (2005) 41.

[10] V. Sujan, S. Dubowsky, Design of a lightweight hyper-redundant deployable binary manipulator, Journal of Mechanical Design 126 (1) (2004) 29–39.

[11] A. Wingert, M. Lichter, S. Dubowsky, M. Hafez, Hyper-redundant robot manipulators actuated by optimized binary dielectric polymers, in: Proceedings of SPIE - The International Society for Optical Engineering, Vol. 4695, 2002, pp. 415–423.

[12] J. Vogan, A. Wingert, J. S. Plante, S. Dubowsky, M. Hafez, D. Kacher, F. Jolesz, Manipulation in mri devices using electrostrictive polymer actuators: with an application to reconfigurable imaging coils, in: Proc. IEEE

International Conference on Robotics and Automation ICRA '04, Vol. 3, 2004, pp. 2498–2504 Vol.3.

[13] F. Carpi, P. Chiarelli, A. Mazzoldi, D. De Rossi, Electromechanical characterisation of dielectric elastomer planar actuators: comparative evaluation of different electrode materials and different counterloads, Sensors and Actuators, A: Physical 107 (1) (2003) 85–95.

[14] B. O'Brien, J. Thode, I. Anderson, E. Calius, E. Haemmerle, S. Xie, Integrated extension sensor based on resistance and voltage measurement for a dielectric elastomer, in: Electroactive Polymer Actuators and Devices (EAPAD) 2007, Vol. 6524, SPIE, San Diego, California, USA, 2007, pp. 652415–11.

[15] R. Pelrine, R. Kornbluh, J. Joseph, R. Heydt, Q. Pei, S. Chiba, High-field deformation of elastomeric dielectrics for actuators, Materials Science and Engineering C 11 (2) (2000) 89–100.

[16] M. Aschwanden, A. Stemmer, Low voltage, highly tunable diffraction grating based on dielectric elastomer actuators, in: Electroactive Polymer Actuators and Devices (EAPAD) 2007, Vol. 6524, SPIE, San Diego, California, USA, 2007, pp. 65241N–10.

[17] J. J. Loverich, I. Kanno, H. Kotera, Concepts for a new class of all-polymer micropumps, Lab on a Chip - Miniaturisation for Chemistry and Biology 6 (9) (2006) 1147–1154.

[18] A. Pimpin, Y. Suzuki, N. Kasagi, Micro electrostrictive actuator with metal compliant electrodes for flow control applications, in: Proc. 17th IEEE International Conference on Micro Electro Mechanical Systems (MEMS), 2004, pp. 478–481.

[19] A. Pimpin, Y. Suzuki, N. Kasagi, Microelectrostrictive actuator with large out-of-plane deformation for flow-control application, Journal of Microelectromechanical Systems 16 (3) (2007) 753–764.

[20] P. Dubois, S. Rosset, S. Koster, J. M. Buforn, J. Stauffer, S. Mikhailov, M. Dadras, N. F. De Rooij, H. Shea, Microactuators based on ion-implanted dielectric electroactive polymer membranes (eap), in: Digest of Technical Papers - International Conference on Solid State Sensors and Actuators and Microsystems, TRANSDUCERS '05, Vol. 2, 2005, pp. 2048–2051.

[21] X. Q. Zhang, M. Wissler, B. Jaehne, R. Broennimann, G. Kovacs, Effects of crosslinking, prestrain and dielectric filler on the electromechanical response of a new silicone and comparison with acrylic elastomer, in: Proceedings of SPIE - The International Society for Optical Engineering, Vol. 5385, 2004, pp. 78–86.

[22] H. C. Nathanson, W. E. Newell, R. A. Wickstrom, J. Davis, J. R. Jr A. Davis J. R., The resonant gate transistor, Electron Devices, IEEE Transactions on 14 (3) (1967) 117–133, 0018-9383.

[23] G. A. Holzapfel, Nonlinear Solid Mechanics, John Wiley, Chichester, 2000.

[24] M. Wissler, E. Mazza, Modeling of a pre-strained circular actuator made of dielectric elastomers, Sensors and Actuators, A: Physical 120 (1) (2005) 184–192.

[25] P. Lochmatter, G. Kovacs, Design and characterization of an active hinge segment based on soft dielectric eaps, Sensors and Actuators, A: Physical 141 (2) (2008) 577–587.

[26] H. R. Choi, K. Jung, N. H. Chuc, M. Jung, I. Koo, J. Koo, J. Lee, J. Lee, J. Nam, M. Cho, Y. Lee, Effects of prestrain on behavior of dielectric elastomer actuator, in: Smart Structures and Materials 2005: Electroactive Polymer Actuators and Devices (EAPAD), Vol. 5759, SPIE, San Diego, CA, USA, 2005, pp. 283–291.

[27] S. P. Lacour, S. Wagner, H. Prahlad, R. Pelrine, High voltage photoconductive switches of amorphous silicon for electroactive polymer actuators, Journal of Non-Crystalline Solids 338-340 (2004) 736–739.

[28] P. Dubois, S. Rosset, S. Koster, J. Stauffer, S. Mikhailov, M. Dadras, N.-F. de Rooij, H. Shea, Microactuators based on ion implanted dielectric electroactive polymer (eap) membranes, Sensors and Actuators, A: Physical 130-131 (2006) 147–154.

[29] J. F. Ziegler, The stopping and range of ions in matter (srim) (2008). URL www.srim.org

[30] X. Wang, M. Chen, J. Chen, W. Zheng, Novel approaches for low cost fabrication of soi, Current Applied Physics 1 (2-3) (2001) 225–231.

[31] L. Rubin, J. Poate, Ion implantation in silicon technology, The Industrial Physicist 9 (3) (2003) 12–15.

[32] P. K. Chu, J. Y. Chen, L. P. Wang, N. Huang, Plasma-surface modification of biomaterials, Materials Science and Engineering: R: Reports 36 (5-6) (2002) 143–206.

[33] I. Azarko, I. Karpovich, I. Kozlov, E. Kozlova, V. Odzhaev, V. Popok, V. Hnatowicz, Influence of ion implantation on the properties of polymer films, Solid State Communications 95 (1) (1995) 49–51.

[34] A. De Bonis, G. Marletta, A. Bearzotti, Structural modifications and electrical properties in ion-irradiated polyimide, Nuclear Instruments and Methods in Physics Research, Section B: Beam Interactions with Materials and Atoms 151 (1-4) (1999) 101–108.

[35] H. Dong, T. Bell, State-of-the-art overview: Ion beam surface modification of polymers towards improving tribological properties, Surface and Coatings Technology 111 (1) (1999) 29–40.

[36] J.-P. Salvetat, J.-M. Costantini, F. Brisard, L. Zuppiroli, Onset and growth of conduction in polyimide kapton induced by swift heavy-ion irradiation, Physical Review B - Condensed Matter and Materials Physics 55 (10) (1997) 6238–6248.

[37] J. Y. Sze, B. K. Tay, C. I. Pakes, D. N. Jamieson, S. Prawer, Conducting ni nanoparticles in an ion-modified polymer, Journal of Applied Physics 98 (6) (2005) 066101–3.

[38] Y. Wu, T. Zhang, H. Zhang, X. Zhang, Z. Deng, G. Zhou, Electrical properties of polymer modified by metal ion implantation, Nuclear Instruments and Methods in Physics Research Section B: Beam Interactions with Materials and Atoms 169 (1-4) (2000) 89–93.

[39] Y. Wu, T. Zhang, Y. Zhang, H. Zhang, X. Zhang, G. Zhou, Behavior of pet implanted by ti, ag, si and c ion using mevva implantation, Nuclear Instruments and Methods in Physics Research Section B: Beam Interactions with Materials and Atoms 173 (3) (2001) 292–298.

[40] W. Yuguang, Z. Tonghe, L. Andong, Z. Gu, The nano-structure and properties of ag-implanted pet, Surface and Coatings Technology 157 (2-3) (2002) 262–266.

[41] W. Yuguang, Z. Tonghe, L. Andong, Z. Xu, Z. Gu, Properties of implanted pet by w ion using mevva implantation, Vacuum 69 (4) (2003) 461–466.

[42] W. Yuguang, Z. Tonghe, Z. Yawen, Z. Gu, Z. Huixing, Z. Xiaoji, Influence of nanostructure on electrical and mechanical properties for cu implanted pet, Surface and Coatings Technology 148 (2-3) (2001) 221–225.

[43] A. Anders, S. Anders, I. G. Brown, Effect of duct bias on transport of vacuum arc plasmas through curved magnetic filters, Journal of Applied Physics 75 (10) (1994) 4900–4905.

[44] A. Anders, S. Anders, I. G. Brown, Transport of vacuum arc plasmas through magnetic macroparticle filters, Plasma Sources Science and Technology 4 (1) (1995) 1–12.

[45] E. Byon, T. W. H. Oates, A. Anders, Coalescence of nanometer silver islands on oxides grown by filtered cathodic arc deposition, Applied Physics Letters 82 (10) (2003) 1634–1636.

[46] S. Anders, A. Anders, I. Brown, Macroparticle-free thin films produced by an efficient vacuum arc deposition technique, Journal of Applied Physics 74 (6) (1993) 4239–4241.

[47] S. Anders, A. Anders, I. Brown, Focused injection of vacuum arc plasmas into curved magnetic filters, Journal of Applied Physics 75 (10) (1994) 4895–4899.

[48] S. Anders, A. Anders, M. R. Dickinson, R. A. MacGill, I. G. Brown, S-shaped magnetic macroparticle filter for cathodic arc deposition, IEEE Transactions on Plasma Science 25 (4) (1997) 670–674.

[49] M. M. M. Bilek, P. Evans, D. R. Mckenzie, D. G. McCulloch, H. Zreiqat, C. R. Howlett, Metal ion implantation using a filtered cathodic vacuum arc, Journal of Applied Physics 87 (9) (2000) 4198–4204.

[50] J. Koskinen, A. Anttila, J. P. Hirvonen, Diamond-like carbon coatings by arc-discharge methods, Surface and Coatings Technology 47 (1-3) (1991) 180–187.

[51] I. Aksenov, V. A. Belous, V. G. Padalka, V. M. Khoroshikh, Soviet Journal of Plasma Physics 4 (1978) 425.

[52] S. Anders, A. Anders, I. G. Brown, R. A. MacGill, M. R. Dickinson, Vacuum arc ion source with filtered plasma for macroparticle-free implantation, Review of Scientific Instruments 65 (4) (1994) 1319–1321.

[53] I. G. Brown, Vacuum arc metal plasma production and the transition of processing mode from metal ion beam to dc metal plasma immersion, Surface and Coatings Technology 136 (1-3) (2001) 16–22.

[54] I. G. Brown, X. Godechot, Vacuum arc ion charge-state distributions 19 (5) (1991) 713–717.

[55] I. G. Brown, O. R. Monteiro, M. M. M. Bilek, High voltage sheath behavior in a drifting plasma, Applied Physics Letters 74 (17) (1999) 2426–2428.

[56] A. Anders, G. Y. Yushkov, Ion flux from vacuum arc cathode spots in the absence and presence of a magnetic field, Journal of Applied Physics 91 (8) (2002) 4824–4832.

[57] I. G. Brown, Vacuum arc ion sources for particle accelerators and ion implantation, IEEE T Plasma Sci 21 (5) (1993) 537–546.

[58] I. G. Brown, Applications of the mevva high current metal ion source, Nuclear Instruments and Methods in Physics Research, Section B: Beam Interactions with Materials and Atoms B24-25 (pt 2 Apr III) (1986) 841–844.

[59] T. S. Green, Beam formation and space charge neutralisation 23 (2) (1976) 918–928.

[60] A. Anders (editor), Handbook of Plasma Immersion Ion Implantation and Deposition, John Wiley, New-York, 2000.

[61] A. Anders, S. Anders, I. G. Brown, M. R. Dickinson, R. A. MacGill, Metal plasma immersion ion implantation and deposition using vacuum arc plasma sources, Journal of Vacuum Science and Technology B 12 (2) (1994) 815–820.

[62] M. Niklaus, S. Rosset, M. Dadras, P. Dubois, H. Shea, Microstructure of 5kev gold-implanted polydimethylsiloxane, Scripta Materialia 59 (8) (2008) 893–896.

[63] M. Niklaus, S. Rosset, M. Dadras, P. Dubois, H. R. Shea, Modification of conductivity and of mechanical properties of electroactive polymer (eap) thin films by titanium ion implantation, in: Mater. Res. Soc. Symp. Proc., Vol. 1052, Materials Research Society, Boston, MA, 2008.

[64] S. Takamatsu, K. Matsumoto, I. Shimoyama, Mechanically flexible and expandable display with conductive-polymer-coated nylon fabric, in: Proc. IEEE 21st International Conference on Micro Electro Mechanical Systems MEMS 2008, 2008, pp. 140–143.

[65] P.-J. Chen, D. C. Rodger, S. Saati, M. S. Humayun, Y.-C. Tai, Implantable parylene-based wireless intraocular pressure sensor, in: Proc. IEEE 21st International Conference on Micro Electro Mechanical Systems MEMS 2008, 2008, pp. 58–61.

[66] V. J. Lumelsky, M. S. Shur, S. Wagner, Sensitive skin, IEEE Sensors Journal 1 (1) (2001) 41–51.

[67] N. Bowden, S. Brittain, A. G. Evans, J. W. Hutchinson, G. M. Whitesides, Spontaneous formation of ordered structures in thin films of metals supported on an elastomeric polymer, Nature 393 (6681) (1998) 146–149.

[68] S. P. Lacour, S. Wagner, Z. Huang, Z. Suo, Stretchable gold conductors on elastomeric substrates, Applied Physics Letters 82 (15) (2003) 2404–2406.

[69] S. P. Lacour, J. Jones, Z. Suo, S. A. W. S. Wagner, Design and performance of thin metal film interconnects for skin-like electronic circuits, IEEE Electron Device Letters 25 (4) (2004) 179–181.

[70] E. Seker, M. Reed, M. Utz, M. R. Begley, Flexible and conductive bilayer membranes of nanoporous gold and silicone: Synthesis and characterization, Applied Physics Letters 92 (15) (2008) 154101–3.

[71] M. G. Urdaneta, R. Delille, E. Smela, Stretchable electrodes with high conductivity and photo-patternability, Advanced Materials 19 (18) (2007) 2629–2633.

[72] W. Yuan, T. Lam, J. Biggs, L. Hu, Z. Yu, S. Ha, D. Xi, M. K. Senesky, G. Gruner, Q. Pei, New electrode materials for dielectric elastomer actuators, in: Electroactive Polymer Actuators and Devices (EAPAD) 2007, Vol. 6524, SPIE, San Diego, California, USA, 2007, pp. 65240N–12.

[73] S. Sawano, K. Naka, A. Werber, H. Zappe, S. Konishi, Sealing method of pdms as elastic material for mems, in: Proc. IEEE 21st International Conference on Micro Electro Mechanical Systems MEMS 2008, 2008, pp. 419–422.

[74] P. Carazzetti, P. Renaud, H. Shea, Low-power hermetically sealed on-chip plasma light source micromachined in glass, in: Micro Electro Mechanical Systems, 2008. MEMS 2008. IEEE 21st International Conference on, 2008, pp. 818–821.

[75] E. Bonnotte, P. Delobelle, L. Bornier, B. Trolard, G. Tribillon, Two interferometric methods for the mechanical characterization of thin films by bulging tests. application to single crystal of silicon, Journal of Materials Research 12 (9) (1997) 2234–2248.

[76] J. J. Vlassak, W. D. Nix, A new bulge test technique for the determination of young's modulus and poisson's ratio of thin films, Journal of Materials Research 7 (12) (1992) 3242–3249.

[77] A. J. Kalkman, A. H. Verbruggen, G. C. A. M. Janssen, High-temperature bulge-test setup for mechanical testing of free-standing thin films, Review of Scientific Instruments 74 (3) (2003) 1383–1385.

[78] V. Paviot, J. Vlassak, W. Nix, Measuring the mechanical properties of thin metal films by means of bulge testing of micromachined windows, in: Mater. Res. Soc. Symp. Proc., Vol. 356, 1995, pp. 579–584.

[79] B. E. Alaca, J. C. Selby, M. T. A. Saif, H. Sehitoglu, Biaxial testing of nanoscale films on compliant substrates: Fatigue and fracture, Review of Scientific Instruments 73 (8) (2002) 2963–2970.

[80] C. Poilane, P. Delobelle, L. Bornier, P. Mounaix, X. Melique, D. Lippens, Determination of the mechanical properties of thin polyimide films deposited on a gaas substrate by bulging and nanoindentation tests, Materials Science and Engineering A 262 (1-2) (1999) 101–106.

[81] J. D. Hall, N. E. Apperson, B. T. Crozier, C. Xu, R. F. Richards, D. F. Bahr, C. D. Richards, A facility for characterizing the dynamic mechanical behavior of thin membranes for microelectromechanical systems, Review of Scientific Instruments 73 (5) (2002) 2067–2072.

[82] M. Small, W. D. Nix, Analysis of the accuracy of the bulge test in determining the mechanical properties of thin films, Journal of Materials Research 7 (6) (1992) 1553–1563.

[83] D. Briand, P. Dubois, L.-E. Bonjour, L. Guillot, U. Bley, S. Danninger, S. Rosset, H. Shea, N. F. de Rooij, Large deformation balloon micro-actuator based on pyrotechnics on chip, in: 21st IEEE International Conference on Micro Electro Mechanical Systems, Tucson, AZ, 2008, pp. 535–538.

[84] C.R.M., C.R.P., C.R.C., Formulaires et Tables, mathematique, physique, chimie, 4th Edition, Editions du Tricorne, Geneve, 1992.

[85] S. Rosset, M. Niklaus, P. Dubois, H. R. Shea, Mechanical characterization of a dielectric elastomer microactuator with ion-implanted electrodes, Sensors and Actuators, A: Physical 144 (1) (2008) 185–193.

[86] K. McGoldrick, Mobile friendly rollable displays, in: Solid-State Device Research Conference, 2006. ESSDERC 2006. Proceeding of the 36th European, 2006, pp. 1–2.

[87] D. H. Kim, J. H. Ahn, M. C. Won, H. S. Kim, T. H. Kim, J. Song, Y. Y. Huang, Z. Liu, C. Lu, J. A. Rogers, Stretchable and foldable silicon integrated circuits, Science 320 (5875) (2008) 507–511.

[88] S. Rosset, M. Niklaus, P. Dubois, M. Dadras, H. R. Shea, Mechanical properties of electroactive polymer microactuators with ion-implanted electrodes, in: Electroactive Polymer Actuators and Devices (EAPAD) 2007, Vol. 6524, SPIE, San Diego, California, USA, 2007, pp. 652410–11.

[89] S. Rosset, M. Niklaus, V. Stojanov, A. Felber, P. Dubois, H. R. Shea, Ion-implanted compliant and patternable electrodes for miniaturized dielectric elastomer actuators, in: Electroactive Polymer Actuators and Devices (EAPAD) 2008, Vol. 6927, SPIE, San Diego, California, USA, 2008, pp. 69270W–10.

[90] S. P. Lacour, H. Prahlad, R. Pelrine, S. Wagner, Mechatronic system of dielectric elastomer actuators addressed by thin film photoconductors on plastic, Sensors and Actuators, A: Physical 111 (2-3) (2004) 288–292.

[91] W. C. Young, Roark's Formulas for Stress and Strain, 6th Edition, McGraw-Hill, New York, 1989.

[92] S. Timoshenko, D. H. Young, W. Weaver, Vibration Problems in Engineering, 4th Edition, John Wiley, New-York, 1974.

[93] S. D. Senturia, Microsystem Design, Kluwer Academic Publishers, Boston, 2001.

[94] P. Dubois, S. Rosset, M. Niklaus, M. Dadras, H. Shea, Voltage control of the resonance frequency of dielectric electroactive polymer (deap) membranes, Journal of Microelectromechanical Systems 17 (5) (2008) 1072–1081.

[95] M. Rosenthal, C. Weaber, I. Polyakov, A. Zarrabi, P. Gise, Designing components using smartmove electroactive polymer technology, in: Electroactive Polymer Actuators and Devices (EAPAD) 2008, Vol. 6927, SPIE, San Diego, California, USA, 2008, pp. 692704–12.

[96] A. M. Tews, K. L. Pope, A. J. Snyder, Pressure-volume characteristics of dielectric elastomers diaphragms, in: Proceedings of SPIE - The International Society for Optical Engineering, Vol. 5051, 2003, pp. 159–169.

[97] S. Rosset, M. Niklaus, P. Dubois, H. R. Shea, Performance characterization of miniaturized dielectric elastomer actuators fabricated using metal ion implantation, in: Proc. IEEE 21st International Conference on Micro Electro Mechanical Systems MEMS 2008, 2008, pp. 503–506.

Curriculum Vitae

Samuel Rosset
Born April 15 1980 in le Locle, Switzerland
Swiss citizen
`samuel.rosset@a3.epfl.ch`

Education

2005 – 2008	Doctoral School of the Ecole Polytechnique Fédérale de Lausanne, Microsystems and Microelectronics program
1999 – 2004	Ecole Polytechnique Fédérale de Lausanne (EPFL), micro-engineering section with an "integrated product" orientation, MSc degree in micro-engineering (March 2004)
1998 – 1999	Exchange student in the USA, Emporia High School, Emporia, Kansas
1995 – 1998	Federal Maturity (Matura), "mention bien", Gymnase cantonal de Neuchâtel

Professional Experience

Jan 2005 – 2008	Research assistant and Ph.D. student in the *microsystems for space technologies laboratory* at EPFL (Prof. H. R. Shea). Research on metal ion implantation applied to the fabrication of compliant electrodes for electroactive polymers
2003 – 2008	Teaching activities at EPFL: Assistant for electronics labs, coaching of students for their semester and master projects, assistant of the class "Reliability of Microsystems" given by Prof. Shea, writing and grading of exams, as well as expert for oral exams
Apr 2004 – Dec 2004	Research assistant at the institute of microtechnology (University of Neuchtel), in the photovoltaics and thin-film electronics group (Prof. A. Shah). Construction of a new measurement setup for the characterization of defects in solar cells, allowing fast acquisition time.

Technical Skills

- Programming: C/C++, LabVIEW, Matlab, Assembly, PHP, HTML.
- Windows, Linux, MS Office, Latex, Adobe Illustrator, etc.
- Specialized softwares: finite elements method simulation (ANSYS), masks design (Silvaco-Expert), CAD (Solidworks).
- Clean room processing: standard processes, as well as development of new processes for elastomers (production of thin suspended PDMS membranes).

Language Skills

- French: fluent (first language)
- English: fluent, oral and written
- German: Unfortunately not that good. Needs a refresh.

Recent Publications

- **Rosset, S., et al.**, *Ion-implanted compliant and patternable electrodes for miniaturized dielectric elastomer actuators.* in Proceedings of SPIE 6927, 2008.
- **Rosset, S., et al.**, *Mechanical characterization of a dielectric elastomer microactuator with ion-implanted electrodes.* Sensors and Actuators A: Physical, 2008. 144(1): p. 185-193.
- **Rosset, S., et al.**, *Performance characterization of miniaturized dielectric elastomer actuators fabricated using metal ion implantation.* in IEEE 21st International Conference on MEMS, 2008.